Depth Mapping in Turbid and Deep Waters Using AVIRIS-NG Imagery: A Study in Wax Lake Delta, Louisiana, USA

Siyoon Kwon[1], Paola Passalacqua[1], Antoine Soloy[2], Daniel J Jensen[2], and Marc Simard[3]

[1]The University of Texas at Austin
[2]NASA Jet Propulsion Laboratory, California Institute of Technology
[3]Caltech/Jet Propulsion Laboratory

March 19, 2024

Abstract

Remote sensing has been widely applied to investigate fluvial processes, but depth retrievals face significant constraints in deep and turbid conditions. This study evaluates the potential for depth retrievals under such challenging conditions using NASA's Airborne Visible/Infrared Imaging Spectrometer-Next Generation (AVIRIS-NG) imagery. We employ interpretable machine learning to construct a hyperspectral regressor for water depth and explore the spectral characteristics of deep and turbid waters in Wax Lake Delta (WLD), LA. The reflectance spectra of WLD show minor effects from depth differences due to turbidity. Nevertheless, a Random Forest with Recursive Feature Elimination (RF-RFE) effectively generalizes high and low turbid cases in a single model, achieving a R^2 of 0.94 ± 0.005. Moreover, this model shows a maximum detectable depth of approximately 30 m, outperforming other methods. A spectral analysis using Shapley additive explanations (SHAP) points out the importance of learning various spectral bands and non-linear relationships between depth and reflectance. Specifically, the short blue and Near-InfraRed (NIR) bands, with high attenuation coefficients, play a crucial role. This finding highlights the attenuation as the key process for deep-depth retrievals. The depth maps of WLD captured by this model distinctly represent the spatial distribution of deep river and shallow delta regions. However, the high dependency on short blue and NIR bands leads to discontinuous areas due to the noise sensitivity of these bands. This result highlights a drawback of remote sensing using empirical models. Future research will focus on correcting such discontinuities by integrating data from multiple remote sensing sources.

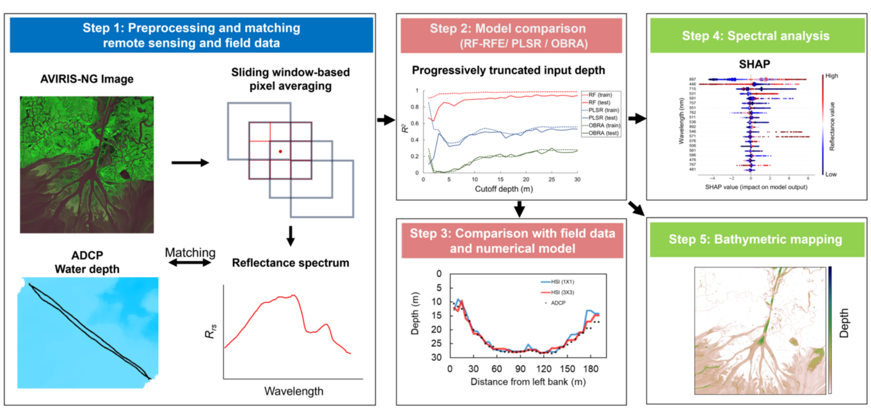

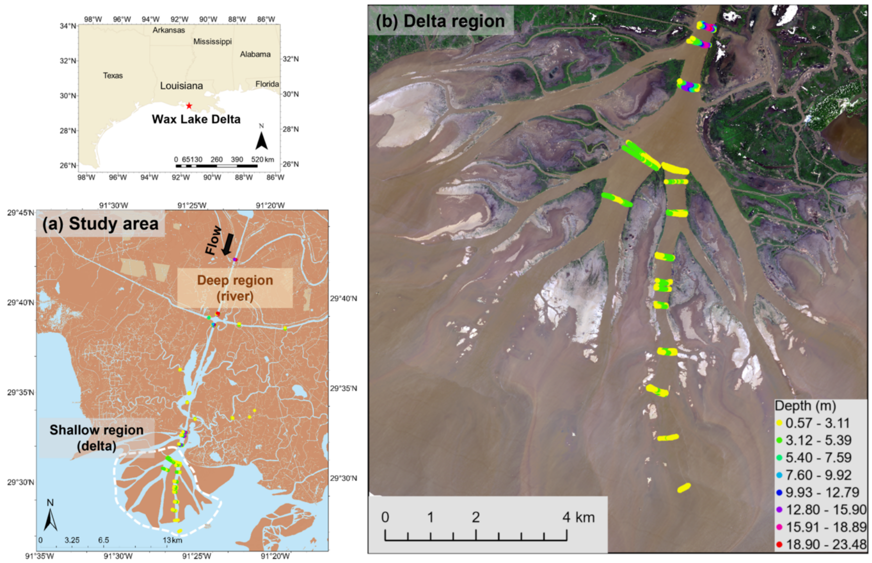

Arkansas
Mississippi
Alabama
Texas
Louisiana
Florida
Wax Lake Delta
(a) Study area
Flow
Deep region (river)
Shallow region (delta)
(b) Delta region
Depth (m)
0.57 - 3.11
3.12 - 5.39
5.40 - 7.59
7.60 - 9.92
9.93 - 12.79
12.80 - 15.90
15.91 - 18.89
18.90 - 23.48
0 1 2 4 km

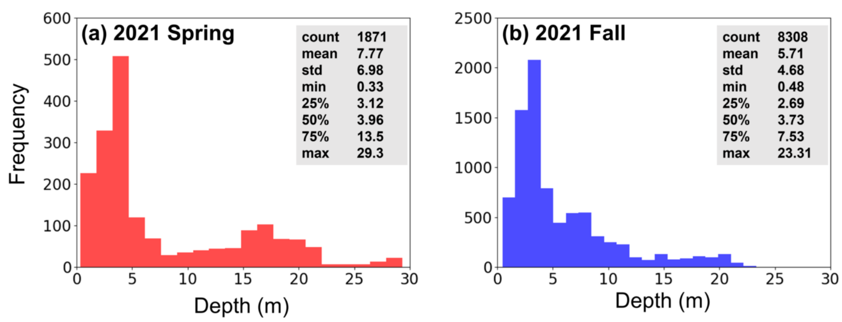

(a) 2021 Spring
count 1871
mean 7.77
std 6.98
min 0.33
25% 3.12
50% 3.96
75% 13.5
max 29.3
Frequency
Depth (m)
(b) 2021 Fall
count 8308
mean 5.71
std 4.68
min 0.48
25% 2.69
50% 3.73
75% 7.53
max 23.31
Depth (m)

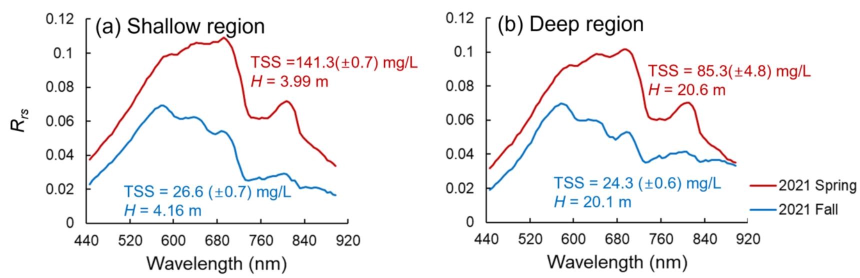

(a) Shallow region
TSS =141.3(±0.7) mg/L
H = 3.99 m
TSS = 26.6 (±0.7) mg/L
H = 4.16 m
Rrs
Wavelength (nm)
(b) Deep region
TSS = 85.3(±4.8) mg/L
H = 20.6 m
TSS = 24.3 (±0.6) mg/L
H = 20.1 m
2021 Spring
2021 Fall
Wavelength (nm)

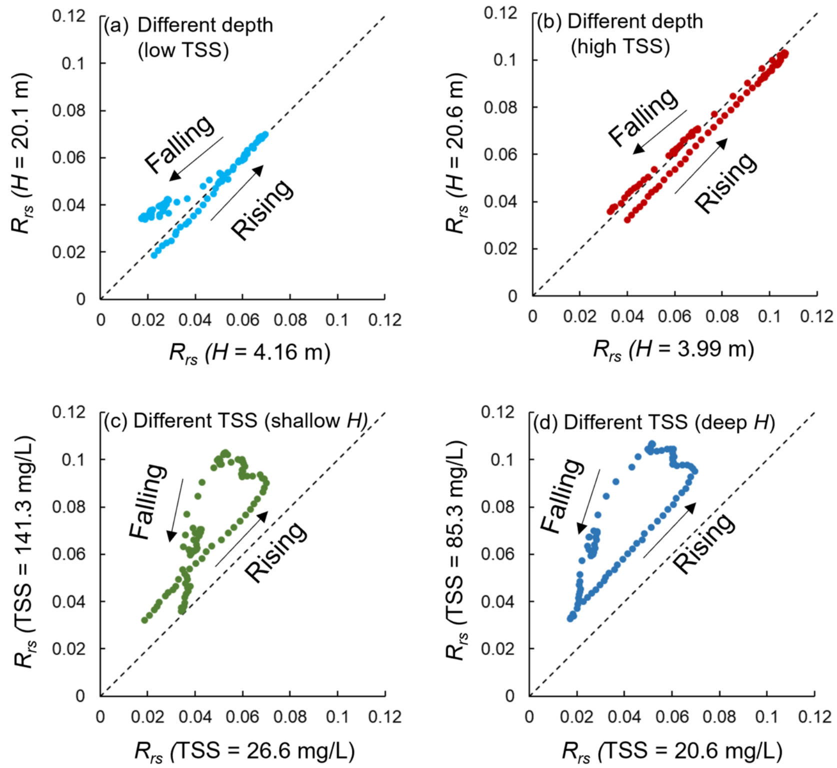
(a) Different depth (low TSS)
Falling
Rising
R_{rs} (H = 20.1 m)
R_{rs} (H = 4.16 m)
(b) Different depth (high TSS)
R_{rs} (H = 20.6 m)
R_{rs} (H = 3.99 m)
(c) Different TSS (shallow H)
R_{rs} (TSS = 141.3 mg/L)
R_{rs} (TSS = 26.6 mg/L)
(d) Different TSS (deep H)
R_{rs} (TSS = 85.3 mg/L)
R_{rs} (TSS = 20.6 mg/L)

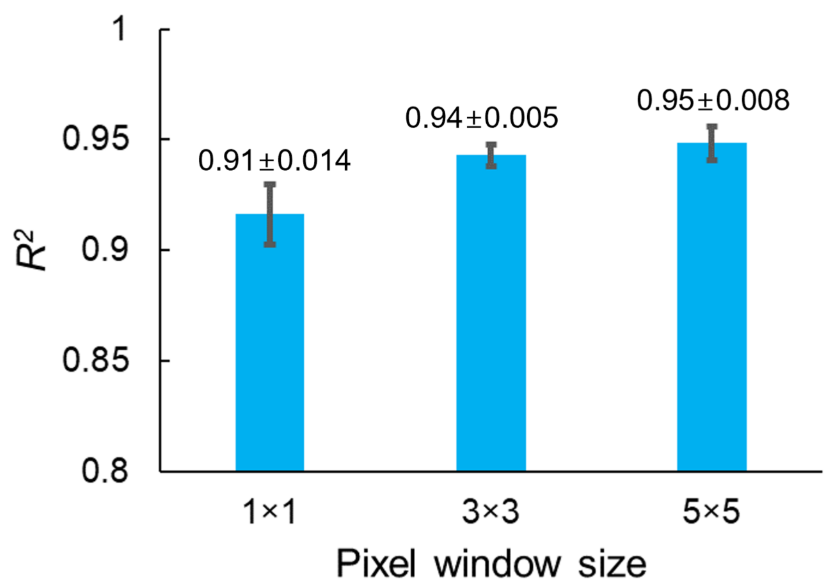
0.91±0.014
0.94±0.005
0.95±0.008
R^2
1×1
3×3
5×5
Pixel window size

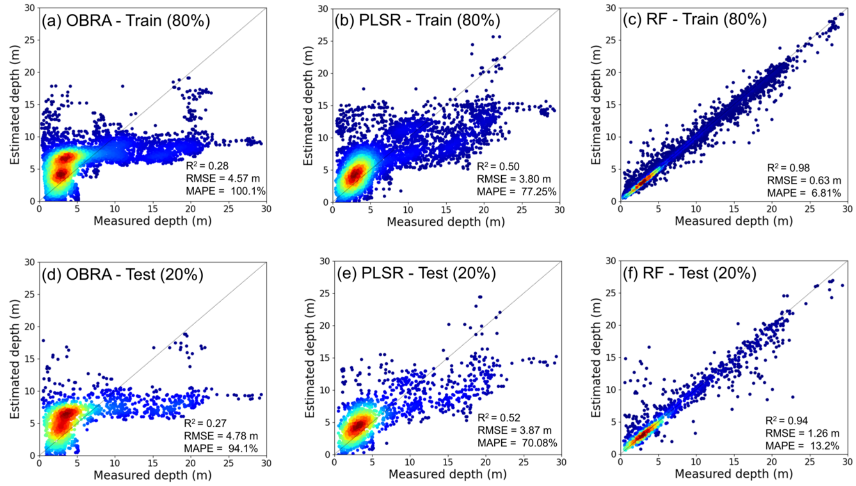
(a) OBRA - Train (80%)
R² = 0.28
RMSE = 4.57 m
MAPE = 100.1%
(b) PLSR - Train (80%)
R² = 0.50
RMSE = 3.80 m
MAPE = 77.25%
(c) RF - Train (80%)
R² = 0.98
RMSE = 0.63 m
MAPE = 6.81%
(d) OBRA - Test (20%)
R² = 0.27
RMSE = 4.78 m
MAPE = 94.1%
(e) PLSR - Test (20%)
R² = 0.52
RMSE = 3.87 m
MAPE = 70.08%
(f) RF - Test (20%)
R² = 0.94
RMSE = 1.26 m
MAPE = 13.2%
Estimated depth (m)
Measured depth (m)

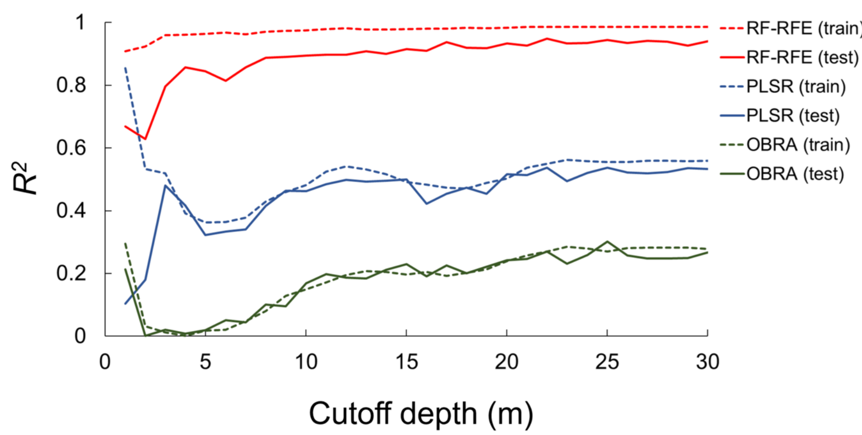
RF-RFE (train)
RF-RFE (test)
PLSR (train)
PLSR (test)
OBRA (train)
OBRA (test)
R²
Cutoff depth (m)

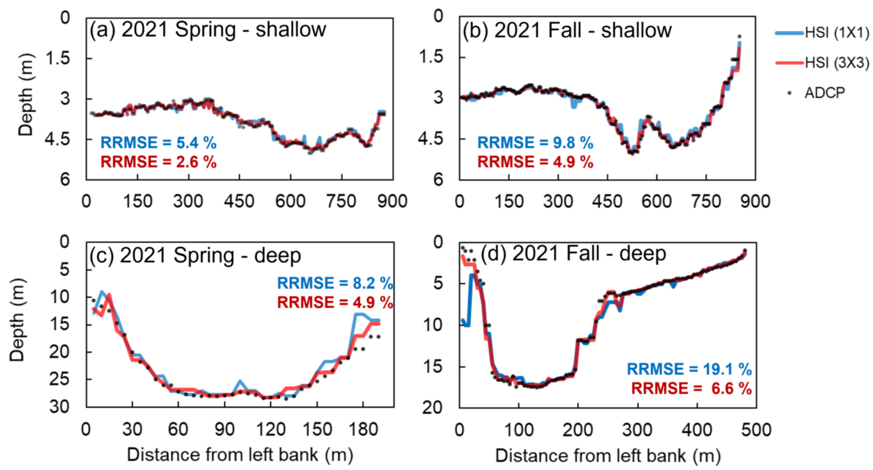
(a) 2021 Spring - shallow
RRMSE = 5.4 %
RRMSE = 2.6 %
(b) 2021 Fall - shallow
RRMSE = 9.8 %
RRMSE = 4.9 %
HSI (1X1)
HSI (3X3)
ADCP
(c) 2021 Spring - deep
RRMSE = 8.2 %
RRMSE = 4.9 %
(d) 2021 Fall - deep
RRMSE = 19.1 %
RRMSE = 6.6 %
Depth (m)
Distance from left bank (m)

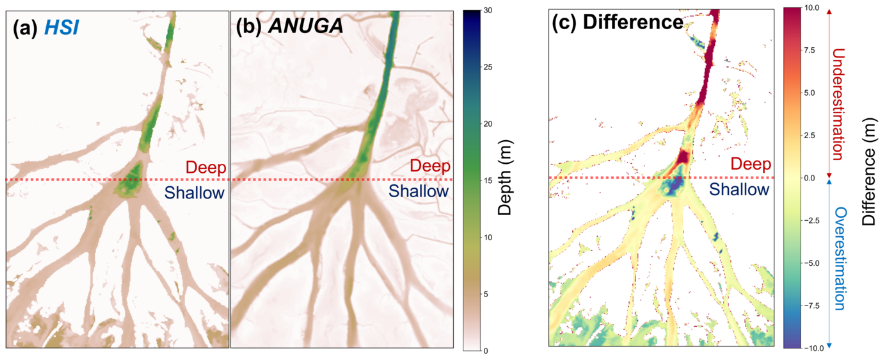

(a) HSI
(b) ANUGA
(c) Difference
Deep
Shallow
Depth (m)
Difference (m)
Underestimation
Overestimation

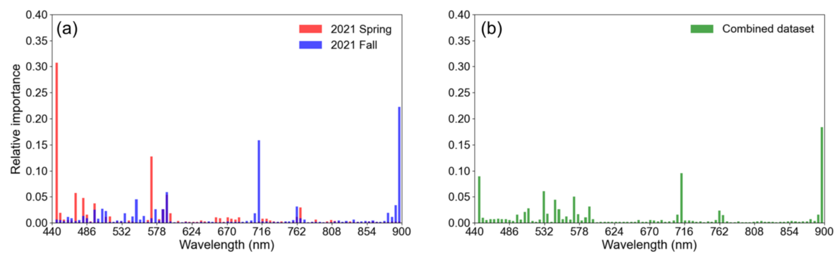

(a)
(b)
2021 Spring
2021 Fall
Combined dataset
Relative importance
Wavelength (nm)

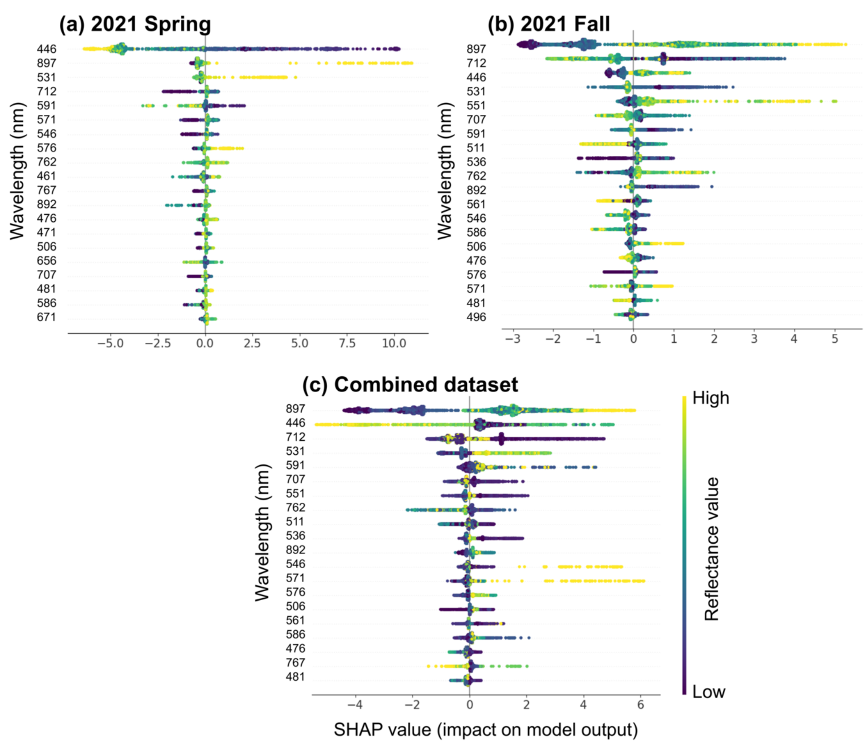

(a) 2021 Spring
(b) 2021 Fall
(c) Combined dataset
Wavelength (nm)
SHAP value (impact on model output)
Reflectance value
High
Low

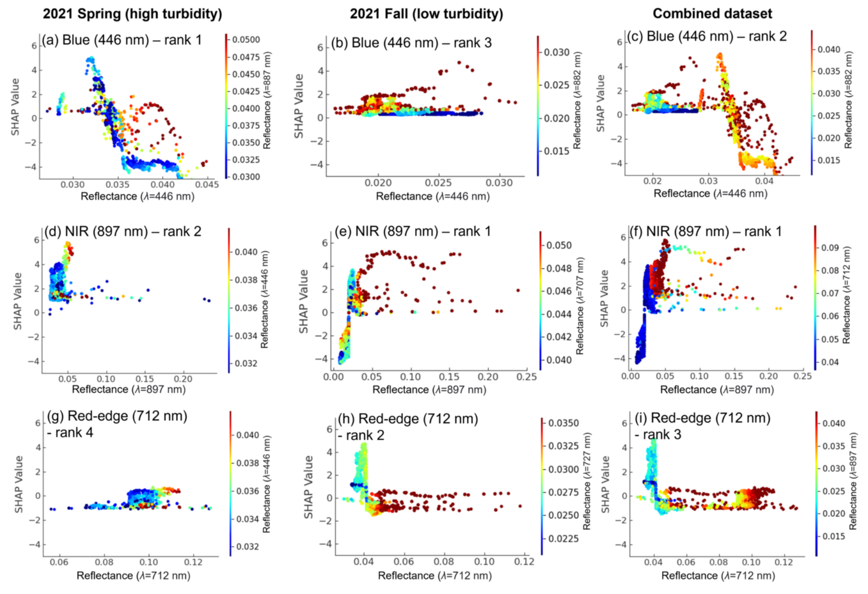
2021 Spring (high turbidity)
2021 Fall (low turbidity)
Combined dataset
(a) Blue (446 nm) – rank 1
(b) Blue (446 nm) – rank 3
(c) Blue (446 nm) – rank 2
(d) NIR (897 nm) – rank 2
(e) NIR (897 nm) – rank 1
(f) NIR (897 nm) – rank 1
(g) Red-edge (712 nm) - rank 4
(h) Red-edge (712 nm) - rank 2
(i) Red-edge (712 nm) - rank 3
SHAP Value
Reflectance (λ=446 nm)
Reflectance (λ=897 nm)
Reflectance (λ=712 nm)
Reflectance (λ=887 nm)
Reflectance (λ=882 nm)
Reflectance (λ=707 nm)
Reflectance (λ=727 nm)

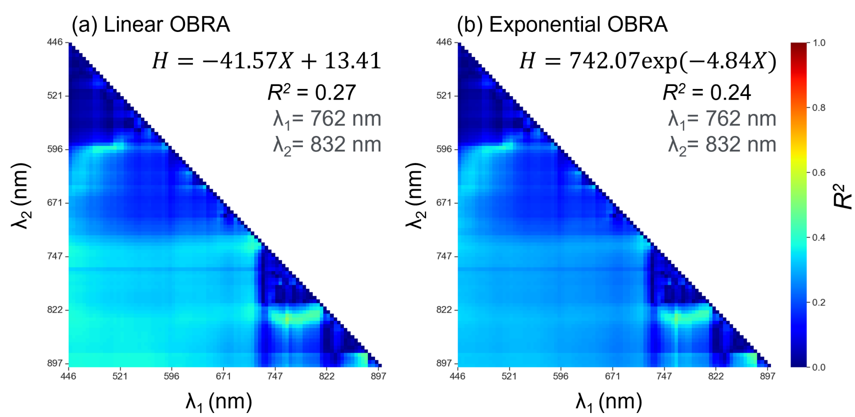
(a) Linear OBRA
$H = -41.57X + 13.41$
R^2 = 0.27
λ_1= 762 nm
λ_2= 832 nm
(b) Exponential OBRA
$H = 742.07\exp(-4.84X)$
R^2 = 0.24
λ_1= 762 nm
λ_2= 832 nm
λ_2 (nm)
λ_1 (nm)
R^2

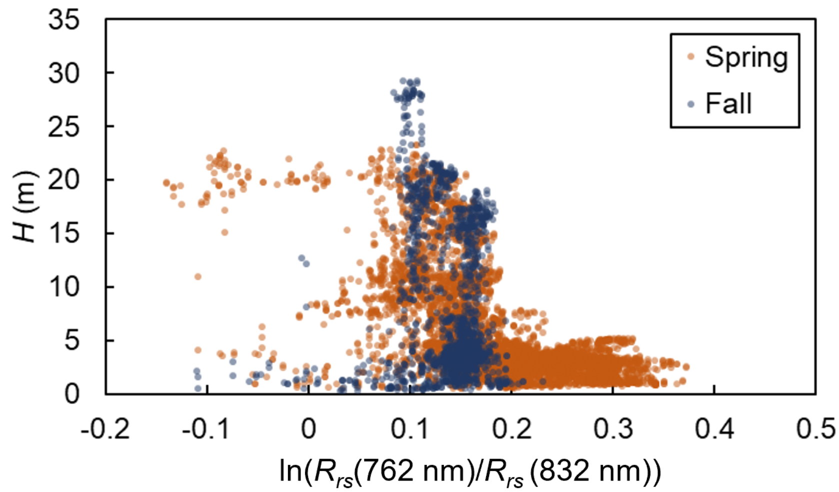

35
30
25
20
15
10
5
0
H (m)
-0.2
-0.1
0
0.1
0.2
0.3
0.4
0.5
ln(Rrs(762 nm)/Rrs (832 nm))
Spring
Fall

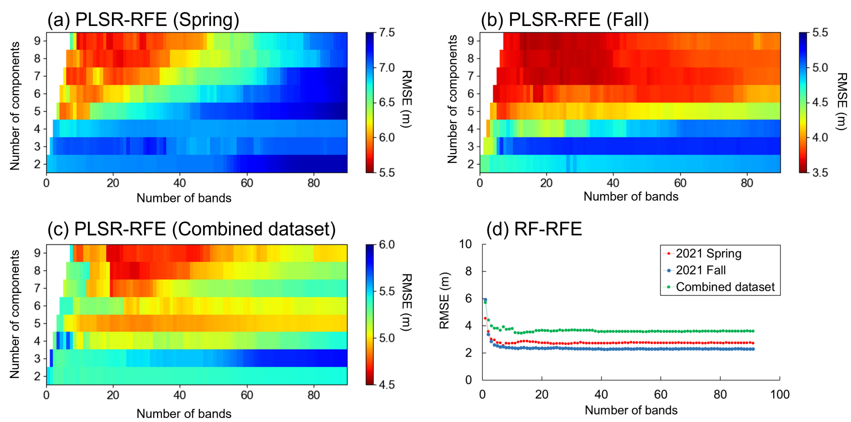

(a) PLSR-RFE (Spring)
(b) PLSR-RFE (Fall)
(c) PLSR-RFE (Combined dataset)
(d) RF-RFE
Number of components
Number of bands
RMSE (m)
2021 Spring
2021 Fall
Combined dataset

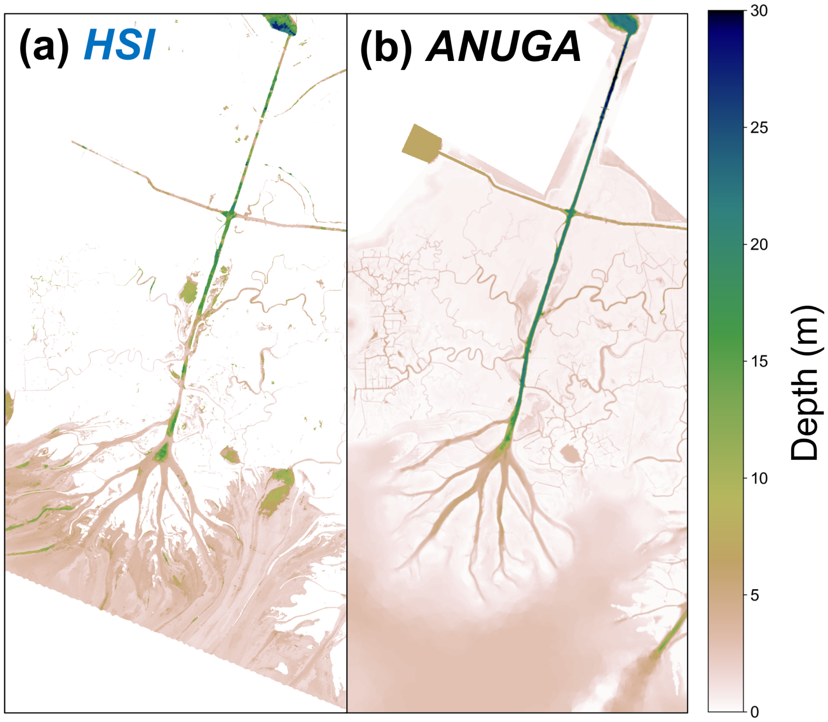
(a) HSI
(b) ANUGA
30
25
20
15
10
5
0
Depth (m)

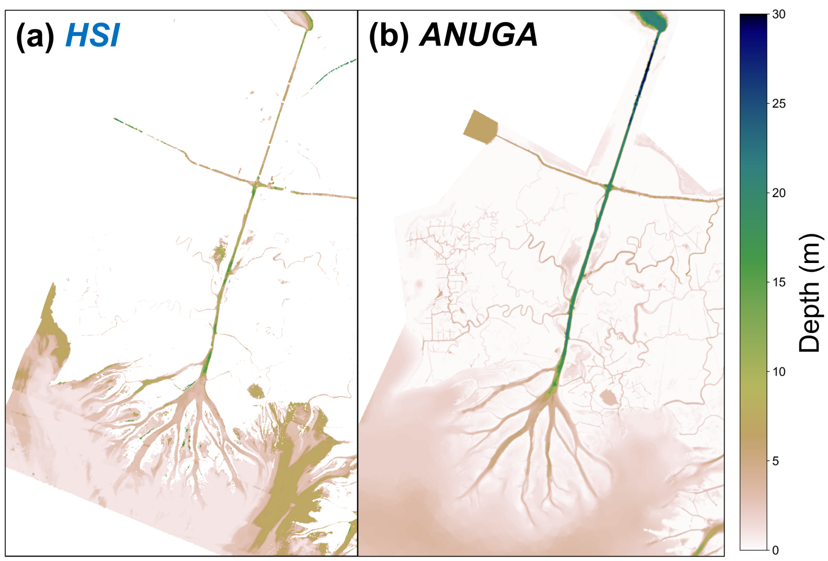
(a) HSI
(b) ANUGA
30
25
20
15
10
5
0
Depth (m)

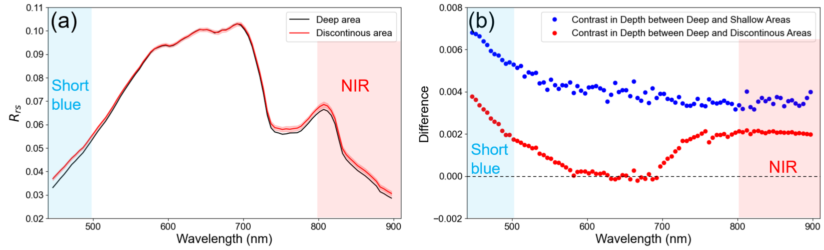
(a)
Deep area
Discontinous area
Short blue
NIR
R_{rs}
Wavelength (nm)
(b)
Contrast in Depth between Deep and Shallow Areas
Contrast in Depth between Deep and Discontinous Areas
Short blue
NIR
Difference
Wavelength (nm)

Depth Mapping in Turbid and Deep Waters Using AVIRIS-NG Imagery: A Study in Wax Lake Delta, Louisiana, USA

Siyoon Kwon[1], Paola Passalacqua[1,2], Antoine Soloy[3], Daniel Jensen[3], Marc Simard[3]

[1]Maseeh Department of Civil, Architectural and Environmental Engineering, The University of Texas at Austin, Austin, TX, USA
[2]Department of Earth and Planetary Sciences, The University of Texas at Austin, Austin, TX, USA
[3]Jet Propulsion Laboratory, California Institute of Technology, Pasadena, CA, USA

Key Points:

- Hyperspectral imaging spectroscopy detects a depth of approximately 30 m in Wax Lake Delta.
- Machine learning successfully generalizes spectral variability of the deep and turbid delta.
- We identify the importance of spectral bands with high attenuation for estimating deep and turbid waters.

Corresponding author: Siyoon Kwon, siyoon@utexas.edu

Abstract

Remote sensing has been widely applied to investigate fluvial processes, but depth retrievals face significant constraints in deep and turbid conditions. This study evaluates the potential for depth retrievals under such challenging conditions using NASA's Airborne Visible/Infrared Imaging Spectrometer-Next Generation (AVIRIS-NG) imagery. We employ interpretable machine learning to construct a hyperspectral regressor for water depth and explore the spectral characteristics of deep and turbid waters in Wax Lake Delta (WLD), LA. The reflectance spectra of WLD show minor effects from depth differences due to turbidity. Nevertheless, a Random Forest with Recursive Feature Elimination (RF-RFE) effectively generalizes high and low turbid cases in a single model, achieving a R^2 of 0.94 ± 0.005. Moreover, this model shows a maximum detectable depth of approximately 30 m, outperforming other methods. A spectral analysis using Shapley additive explanations (SHAP) points out the importance of learning various spectral bands and non-linear relationships between depth and reflectance. Specifically, the short blue and Near-InfraRed (NIR) bands, with high attenuation coefficients, play a crucial role. This finding highlights the attenuation as the key process for deep-depth retrievals. The depth maps of WLD captured by this model distinctly represent the spatial distribution of deep river and shallow delta regions. However, the high dependency on short blue and NIR bands leads to discontinuous areas due to the noise sensitivity of these bands. This result highlights a drawback of remote sensing using empirical models. Future research will focus on correcting such discontinuities by integrating data from multiple remote sensing sources.

1 Introduction

Remote sensing of water depth has been gaining attention across various fields, including fluvial geomorphology, stream ecology, and hydrodynamics owing to its capability of mapping spatially distributed information (Harrison et al., 2022; Niroumand-Jadidi et al., 2022; Moramarco et al., 2019; Hossain et al., 2022). The conventional approach to water depth measurement using acoustic Doppler current profilers (ADCPs) or real-time kinematic global positioning systems (RTK-GPS) depends on point measurements, requiring a substantial investment of time and labor for frequent and spatial measurements (Zinger et al., 2013). This challenge is particularly pronounced in water regions with rapidly changing bed morphology due to sediment transport, such as river deltas.

Remote sensing-based depth measurements have emerged as promising alternatives. Recent development of various sensors and platforms has led to a variety of remote sensing approaches (Legleiter & Harrison, 2019). In particular, active remote sensing, utilizing Light Detection And Ranging (lidar), and passive remote sensing techniques based on imaging spectroscopy, have been widely used (de Almeida et al., 2019). Lidar, which has a low dependence on weather conditions, has become a widely used method for terrain measurements (Passalacqua et al., 2012). For water depth estimates, lidar equipped with a green-wavelength laser is able to penetrate through the water column and thus is typically used to measure shallow water depths (McKean et al., 2014). Recent studies have significantly improved the ability to estimate depths up to 20 m using the advanced topographic laser altimeter system (ATLAS) onboard the Ice, Cloud, and Land Elevation Satellite-2 (ICESat-2) (Xie et al., 2023; Chen et al., 2021). However, applying lidar in turbid waters remains challenging (Legleiter & Harrison, 2019; Chen et al., 2021).Compared to lidar, imaging spectroscopy highly depends on weather conditions, but this method is more versatile thanks to abundant spectral bands that allow it to measure various parameters in water environments at the same time, such as algal bloom, suspended sediment, organic matter, and water depth from one image (Kwon et al., 2022a, 2022b, 2023b; Legleiter et al., 2022; Hestir et al., 2015). Recently, there has been an increase in satellites equipped with hyperspectral sensors, enabling their application over wide spatial areas. Additionally, high-resolution information for specific regions can be obtained through images captured by aircrafts or drones.

In terms of water depth (H) estimates, imaging spectroscopy also has limitations in measuring deep water depth since this method relies on the reflected light from the bottom under the water column. The bottom-reflected radiance exponentially attenuates with the distance of transmittance through the water column (Legleiter et al., 2004) Consequently, accurately measuring deep water depth becomes challenging due to the diminishing strength of bottom-reflected radiance. Legleiter et al. (2018) and Legleiter and Harrison (2019) evaluated the maximum detectable depth of passive optical images for various sensors, platforms, and algorithms under clean and shallow water conditions ($H < 10\,\mathrm{m}$). They introduced Optimal Band Ratio Analysis (OBRA) of progressively truncated input depths (OPTID) and evaluated the performance according to water depth ranges. Their results indicated that hyperspectral imagery from unmanned aerial systems (UAS) or airborne platforms could measure water depths up to 4 m and exhibited superior accuracy compared to multispectral satellite imagery. This result underscores the importance of both spectral and spatial resolutions in hyperspectral retrievals. Gwon et al. (2023) conducted further assessments of hyperspectral retrievals for shallow depths ($H < 1\,\mathrm{m}$) under varying suspended sediment concentrations and compositions in experimental channels. Despite the weak contribution of bottom radiance under turbid conditions, this study revealed that machine-learning (ML) regression improved the performance of hyperspectral retrievals for water depth compared to the conventional regression approach using a few spectral bands (e.g., OBRA). Specifically, among various ML regression algorithms, Random forest (RF) showed accurate and robust performance for hyperspectral retrievals. This result can be attributed to the insensitivity of RF to noise and hyperparameters, a characteristic derived from its ensemble learning approach. The key point arising from the superior performance of ML is that handling non-linearity and numerous variables is critical due to increased spectral variability under optically complex conditions. Nevertheless, the inherent black-box structure of ML represents a weakness, as it prevents the interpretation of causal relationships between inputs and outputs. This characteristic not only limits understanding spectral characteristics but also confines ML-based hyperspectral remote sensing to local applicability.

To enhance the transferability and robustness of the hyperspectral retrievals, many recent studies have attempted to account for spectral variability in water environments (Jensen et al., 2019a; Kwon et al., 2023a, 2022b; Dethier et al., 2020; Niroumand-Jadidi et al., 2019). Niroumand-Jadidi et al. (2020) improved OBRA through the compilation of sample-specific multiple band ratio techniques for satellite-derived bathymetry (SMART-SDB), a fusion of the sample-specific k-nearest neighbor (KNN) method with OBRA. SMART-SDB was much more robust for inland and coastal waters, but the depth ranges of study sites were under 2.5 m. Kwon et al. (2023a) demonstrated the applicability of the Gaussian Mixture Model (GMM) for classifying bottom types in shallow rivers. That study also emphasized the significance of considering spectral variability from various types of river substrates in hyperspectral retrievals of shallow water depth. However, there remain a number of challenges for hyperspectral retrievals of water depth related to their applicability in various conditions. First, the maximum detectable depth was evaluated only with clean and shallow water (Legleiter et al., 2018; Legleiter & Harrison, 2019). The applicability to hyperspectral retrievals of water depth in turbid and deeper conditions is still unknown. ML has the potential to enhance the use of hyperspectral retrievals by capturing the non-linear relationship between water depth and reflectance across various spectral bands. Second, bathymetric studies using imaging spectroscopy are conducted less frequently compared to surveys that focus on the shape or surface dynamics of delta networks (Teresa Jarriel, 2021; Kuenzer et al., 2019). In delta regions with active sediment transport and complex morphodynamics, depth mapping is substantially beneficial for understanding the complex dynamics of channel networks. However, these areas are often highly turbid, leading to limited applicability of remote sensing-based water depth estimation.

It is known that bottom-reflected radiance tends to be weak in turbid and deep waters. Nevertheless, we focus on the radiance emanating from the water column, which is also correlated with water depth through exponential attenuation (Wong et al., 2019; Lee et al., 1999, 2002). The theoretically derived relationship from exponential attenuation (Lee et al., 1999) provides a key insight for hyperspectral retrievals of water depth under deep and turbid conditions. We posit that this relationship can be effectively learned by accounting for non-linearity and spectral variability through a ML approach. Based on this hypothesis, this study aims to evaluate ML-based hyperspectral retrievals of water depth in the turbid and deep region of Wax Lake Delta (WLD) using spatially and spectrally abundant HSI, AVIRIS-NG collected by NASA's Delta-X mission. Subsequently, we analyze spectral variability using the Shapley additive explanation (SHAP), an interpretable ML approach. In particular, we focus on the following specific objectives:

1. Evaluate the potential of remote sensing to retrieve deep water depth under turbid conditions.
2. Compare the maximum detectable depth of hyperspectral retrievals using three regression algorithms.
3. Interpret spectral variability under deep and turbid waters through the SHAP-explained RF framework.
4. Suggest a strategy for accurate and robust depth mapping under diverse conditions as those encountered in coastal environments.

2 Materials and Methods

2.1 Overview

Passive remote sensing of water depth relies on measuring visible and near-infrared (NIR) reflected solar energy (Mobley, 1999). This process takes into account the attenuation within the water column and its interaction with other physical components, which influence the detected signals. Therefore, the total below-surface remote sensing reflectance (R_{rs}) in rivers mainly consists of the signal emanating from the water column and the bottom-reflected signal (Kwon et al., 2023b; Legleiter et al., 2004; Baek et al., 2019). This combination can be expressed by a simple radiative transfer model introduced by Lee et al. (1999):

$$R_{rs}(\lambda) = \frac{L_u(\lambda)}{E_d(\lambda)} = R_\infty(\lambda)\left(1 - e^{-K(\lambda)H}\right) + \frac{\rho_b}{\pi}e^{-K(\lambda)H}, \tag{1}$$

where R_{rs} is the remote sensing reflectance, λ is the wavelength, L_u is total upwelling radiance reaching the sensor, E_d is the irradiance, R_∞ is the reflectance of an infinitely deep water column. H is the water depth, $K(\lambda)$ is the attenuation coefficient, and ρ_b is the bottom albedo, which is a distinctive property according to the bed substrate. Equation (1) shows that the water column reflectance, the first term on the right-hand side, exponentially increases with H and has a maximum value under infinitely deep depth. The second term on the right-hand side is the bottom reflectance, exponentially decreasing with H. Under deep and turbid conditions, the bottom reflectance is negligible, which is the reason why detecting the water depth in this condition is challenging. Recent studies dealt with these optically deep-water areas by masking unmeasurable pixels (Caballero & Stumpf, 2023). Here, instead, we focus on the exponential relationship between water column reflectance and water depth. We hypothesize that only reflectance from the water column has the potential for measuring water depth in optically deep-water areas if we can account for non-linearity and abundant spectral information using ML.

Based on this hypothesis, this study consists of five key steps to evaluate a ML model and interpret spectral characteristics under deep and turbid conditions (Figure 1). First, we matched hyperspectral imagery acquired by the NASA airborne spectrometer, AVIRIS-NG, and ADCP water depth measurements from the NASA Delta-X mission (Step 1). To achieve this alignment, we averaged the ADCP data on a per-pixel basis corresponding to AVIRIS-NG. We then filtered reflectance values within each pixel through a sliding window-based pixel-averaging process. We also investigated the impact of window size on depth retrievals. Based on the matched dataset, we compared three regression algorithms: Random forest with recursive feature elimination (RF-RFE), partial least squared regression (PLSR), and OBRA (Step 2). To evaluate the sensitivity of each algorithm to depth range, we employed progressively truncated input depth (PTID) as proposed by Legleiter et al. (2018). Subsequently, the best algorithm was compared with cross-sectional depth profiles from ADCP and spatial distributions from the calibrated hydrodynamic model, ANUGA (Step 3) (Wright et al., 2022). This step allowed for the assessment of the accuracy of the retrieved depth maps in both shallow and deep sections, as well as in uncalibrated areas. Following that, the trained RF model was employed to understand how reflectance spectra relate to water depth through the utilization of SHAP (Step 4). We also identified significant wavelengths for water depth retrievals in turbid and deep conditions, considering the RF-RFE model performance in separate and combined learning from two distinct campaign datasets. Ultimately, we visualized the depth maps for the two campaigns from the best model and discussed the qualities of the maps (Step 5). Each step is described in this section, following a description of the study area.

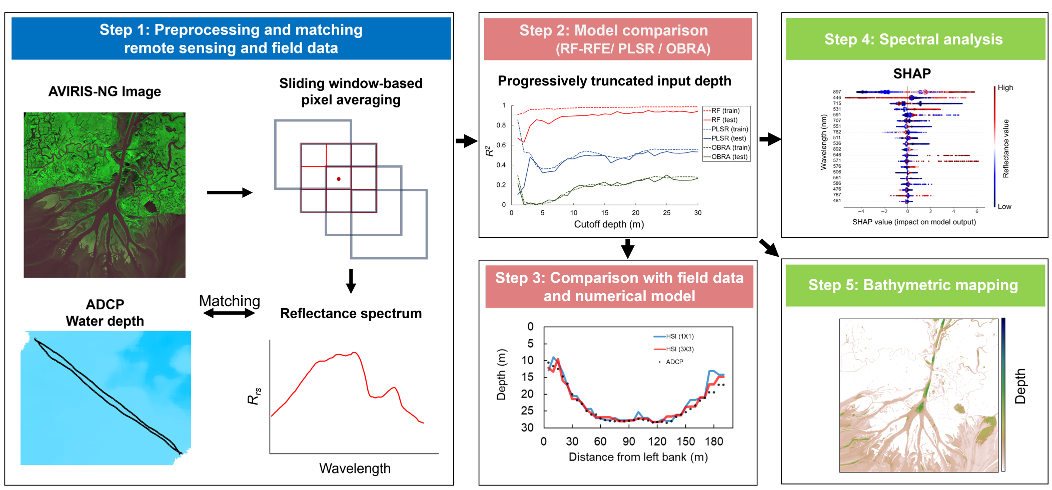

Figure 1. Flowchart of the proposed framework. AVIRIS-NG = airborne visible infrared imaging spectrometer - next generation; RF = random forest; PLSR = partial least squares regression; OBRA = optimal band ratio analysis; SHAP = Shapley additive explanation.

2.2 Study site and field data of Delta-X mission

Wax Lake Delta (WLD) is a delta with an approximate area of $100km^2$, located in coastal Louisiana, at the mouth of the Wax Lake Outlet (WLO) (Figure 2). This region has been steadily building land due to a diversion of the Atchafalaya River with a strong sediment supply, resulting in sediment deposition (Hiatt & Passalacqua, 2015).

Sediment input to WLD is approximately 38.4 Mt per year, with an 18% of sand fraction (Kim et al., 2009). Owing to the morphological features of WLD, the deltaic area is relatively shallow, while the riverine area is relatively deep (Figure 2a, b).

The NASA Delta-X mission provides comprehensive datasets for hydrodynamic, sediment transport, and eco-geomorphic studies, incorporating both in-situ measurements and remote sensing data (Simard et al., 2020). For the depth retrieval model in Step 2 (Figure 1), we utilized the ADCP depth data from the 2021 Spring (from 2021-03-25 to 2021-04-11) and Fall (from 2021-08-16 to 2021-09-25) campaigns of Delta-X as the training and test datasets. At the measurement transects (Figure 2b), the bathymetry was repeatedly measured over two times using a Teledyne RiverPro ADCP or a Sontek M9 RiverSurveyor ADCP. The resolution of the depth profiles ranged from $0.1m$ to $1m$. The overall dataset covered a broader expanse of the Atchafalaya and Terrebonne Basins within the Mississippi River Delta floodplain. However, here, we focus specifically on the data within a 35 km reach of WLD (Figure 2a). The data in this region were collected for three days, specifically from 2021-03-30 to 2021-04-02 (Spring) and 2021-08-20 to 2021-08-22 (Fall), respectively. This narrowing of the study area allows a distinct separation between deep and shallow regions, leading to the isolation of depth difference effects. Additionally, the substantial turbidity and total suspended solid (TSS) difference between the Spring and Fall campaigns in this area makes it particularly suitable for analyzing the effects of turbidity (Table 1). More details of depth and water quality data can be found in Christensen et al. (2022) and Fichot et al. (2022).

To match in-situ depth data with AVIRIS-NG, we averaged the data based on the pixel size of AVIRIS-NG images, which ranged from 3.8 to 5.4 m (Thompson et al., 2022). The number (n) of averaged depth data was 1,871 and 8,308 in the Spring and Fall campaigns, respectively (Table 1). The mean values of water depth were $7.77m$ and $5.71m$ in each campaign, while the discharge at the apex of WLO was five times larger in Spring than in Fall (Table 1). The depth ranges varied, with the maximum depth approaching approximately $30m$ (Figure 3). This information suggests that the dataset allows the assessment of the maximum detectable depth from hyperspectral retrievals, extending up to a $30m$ depth.

Table 1. Field-measured values of hydraulic and water quality parameters in each campaign. n denotes the number of measurements

Parameter	2021 Spring (n)	2021 Fall (n)
Discharge (m^3/s)	5148.3 (Apex)	1646.3 (Apex)
Water depth (m)	7.77±6.98 (1,871)	5.71±4.68 (8,308)
TSS (mg/L)	80.86±40.4 (44)	23.2±8.14 (39)
Turbidity (NTU)	46.2±15.8 (56)	13.59±4.67 (42)
Chl-a (RFU)	0.80±0.11 (56)	1.63±0.75 (42)
Temperature (°C)	16.30±1.31 (56)	30.55±1.27 (42)

2.3 AVIRIS-NG

The Airborne Visible–Infrared Imaging Spectrometer-Next Generation (AVIRIS-NG) is a pushbroom spectral mapping system that captures 14-bit radiance as 425 spectral bands at $5-nm$ resolution with a range from 380 to $2510nm$ wavelengths (Thompson et al., 2015; Chapman et al., 2019). In the Delta-X mission, AVIRIS-NG acquired a wide

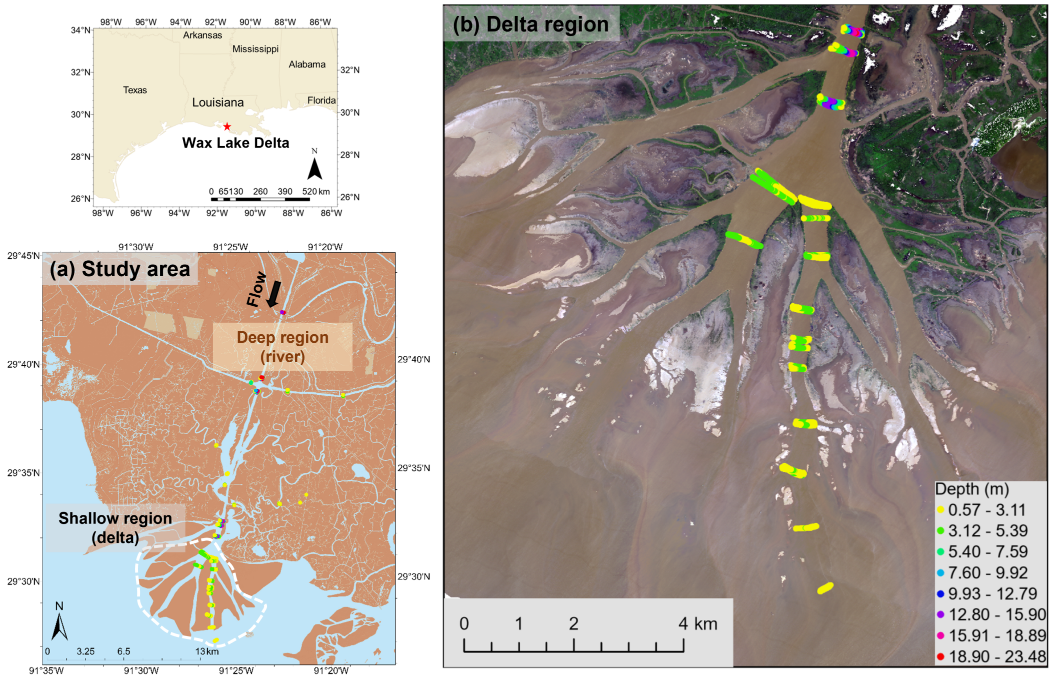

Figure 2. (a) Location of the study site, Wax Lake Delta (WLD), and water depth measurement points by ADCP. (b) Detailed image of the shallow region from AVIRIS-NG and ADCP depth.

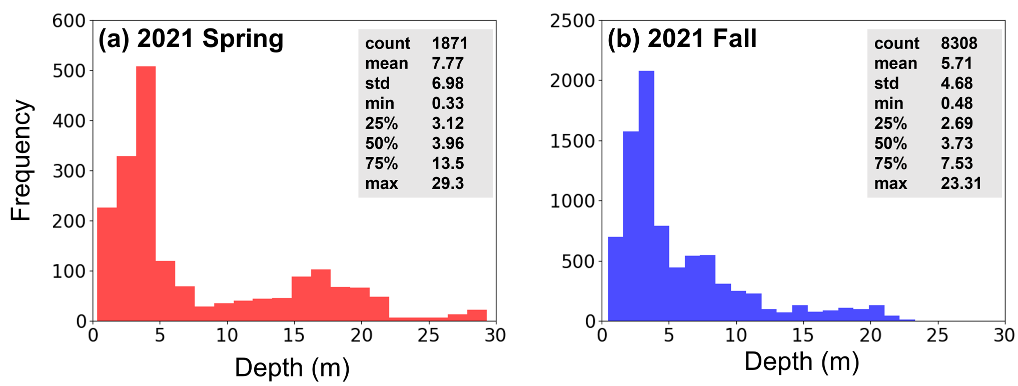

Figure 3. Histograms of measured depths and their corresponding statistics in WLD during 2021 (a) Spring and (b) Fall campaigns.

range of hyperspectral images (HSIs) covering the Atchafalaya and Terrebonne basins in the 2021 Spring and Fall campaigns. We used Level 2B (L2B) bidirectional reflectance distribution function (BRDF) and sunglint-corrected surface spectral reflectance images from AVIRIS-NG for hyperspectral retrievals (Thompson et al., 2023). The atmospheric correction of this dataset was conducted using the optimal estimation algorithm (Thompson et al., 2018a, 2018b, 2019). This process incorporates a radiometric correction for vicarious adjustment to mitigate minor differences between laboratory calibration and actual flight conditions. Details regarding the radiometric correction, which utilizes in-situ references from the Delta-X flight campaign, as well as the sunglint correction, are documented in Bruegge et al. (2021), Gao and Li (2021), and Greenberg et al. (2022). These corrections yield water pixel values that closely approximate the accurate normalized water-leaving reflectance (ρ_w). Consequently, by applying the Lambertian reflection model, the remote-sensing reflectance (R_{rs}) can be directly calculated by dividing ρ_w by π, reflecting isotropic reflectance (Mobley et al., 2010).

In this study, we cropped the mosaic images of the Spring and Fall campaigns within the WLD region, aligning them with the ADCP dataset (Figures 2b). The image acquisition dates were 2021-04-01 (Spring) and 2021-08-20 to 2021-08-22 (Fall). Additionally, we selectively utilized the wavelength range between $446nm$ and $897nm$, a range consistently identified as effective for retrieving both water depth and suspended sediment in various studies (Kwon et al., 2023a; Gwon et al., 2023; Legleiter & Harrison, 2019). We used the ultimately extracted images for model development and spectral analysis by aligning each pixel with preprocessed ADCP depth data, as described in Section 2.2. Here, we subjected the pixel values to a 1:1 matching process with the preprocessed images generated using sliding-window averaging with window sizes of 3x3 and 5x5, as described in Section 2.1. We conducted a comparative study between the images processed with this sliding window and those without preprocessing to examine whether there was an improvement in model performance through noise reduction.

2.4 Regression methods

2.4.1 Optimal Band Ratio Analysis (OBRA)

Optimal Band Ratio Analysis (OBRA) is a representative spectrally based depth retrieval algorithm proposed by Legleiter et al. (2009b). This algorithm is based on an empirical equation for the depth (H) using the log-transformed band ratio (X) as an independent variable:

$$X = \ln\left[\frac{R(\lambda_1)}{R(\lambda_2)}\right] \tag{2}$$

where $R(\lambda_1)$ and $R(\lambda_2)$ are reflectance values at the two most relevant wavelengths, λ_1 and λ_2. These two bands can be identified by evaluating the regression of X versus H for all possible band combinations. Following this iterative regression training, the optimal band combination is determined as the one where X versus H achieves the highest coefficient of determination (R^2). The regression equation is typically selected as a linear form in clear and shallow waters. However, in challenging conditions, non-linear forms, such as exponential, power law, and quadratic forms, are considered. For a more detailed description of OBRA and its applications, refer to Legleiter and Harrison (2019).

2.4.2 Partial Least Squares Regression (PLSR)

While OBRA can only account for two spectral bands, limiting its ability to consider diverse spectral information, Partial Least Squares Regression (PLSR) can leverage multiple spectral bands (Carrascal et al., 2009). Notably, PLSR demonstrates strength in handling multicollinearity and varying sample sizes, a feature that Ordinary Least Squares Regression (OLSR) lacks, making PLSR widely adopted for regression using imaging spectrometer data (Jensen et al., 2019a; Meacham-Hensold et al., 2019).

Specifically, PLSR generates new orthogonal variables called latent variables. These latent variables are derived through covariance optimization based on Principal Component Analysis (PCA) with a weighting for the dependent variable (Jensen et al., 2019b; Singer et al., 2016). The estimation of regression coefficients entails subjecting the latent variables to multiple linear regression (MLR) analysis. This transformation of reflectance spectra into latent variables enables PLSR to effectively address non-linear problems in the relationship between reflectance spectra and water depth data. Following this transformation, the estimation involves a linear regression process with multiple predictors using MLR. In this study, we performed Recursive Feature Elimination (RFE) with cross-validation (CV) and the calibration of the number of latent variables to identify the optimal band set and the number of latent variables with the lowest error for PLSR (Guyon et al., 2002). A higher number of latent variables can lead to overfitting due to noise, so we calibrated the range of components to be between 2 and 9 (Jensen et al., 2019a). We conducted PLSR training and validation using the 'PLSRegression' function from scikit-learn (version 1.3.1). Additionally, we adapted the 'RFE' function from scikit-learn (version 1.3.1) to apply PLSR with RFE-CV and calibration of the number of latent variables ('`n_components`' in 'PLSRegression').

2.4.3 Random forest (RF)

Random forest (RF) has gained widespread usage in spectral imaging applications, demonstrating notable predictive accuracy (Cao et al., 2020; Demarchi et al., 2020; Kwon et al., 2023b, 2022b; Gwon et al., 2023). In particular, RF has shown high interpretability through the estimation of relative variable importance, which can be used for spectral band selection. When compared to alternative ML algorithms such as the support vector regressor (SVR), neural networks, and boosting-based decision tree models (e.g., Gradient Boosting, XGBoost, AdaBoost), RF stands out due to its ensemble learning approach (Kwon et al., 2022b). This method offers several distinct advantages, as follows: (a) insensitivity to hyperparameters, (b) efficient model development during iterative training, reducing the required time, (c) robustness in handling noisy data, and (d) efficiency in managing input variables.

Reducing prediction variance through ensemble learning, a concept introduced by Breiman (2001), can be advantageous for spectral data with inherent noise. RF seamlessly integrates multiple decision trees, arriving at predictions by averaging the individual tree outputs. In this process, each decision tree randomly selects samples and variables, partitioning the input variable into nodes based on the output variable values. Throughout the model training phase, the split for each node is strategically determined, aiming to maximize the reduction in overall impurity within the nodes. In this study, we estimated impurity through the mean square error (MSE), as follows:

$$\mathrm{MSE} = \frac{1}{n}\sum_{i}\left(y_i - \widehat{y_i}\right)^2, \tag{3}$$

where n represents the number of observations, y_i is the true value (ADCP water depth data), and $\widehat{y_i}$ denotes the estimated value (the retrieved water depth from hyperspectral data). From the impurity of the trained model, we can estimate the relative band importance since impurity reduction in each spectral band indicates a positive effect on prediction. Therefore, we can estimate the relative band importance (I_λ) by:

$$I_\lambda = \sum_{nt} \Delta MSE_\lambda(nt), \tag{4}$$

where λ is the wavelength of each spectral band and nt is the number of trees in the ensemble structure of RF. Furthermore, I_λ can be used for optimal band selection using RFE with CV. Kwon et al. (2022a) employed RFE for hyperspectral retrievals of suspended sediment concentration under optically complex conditions. That study highlighted that utilizing the optimal combination of bands through RFE is more efficient than using the entire set of bands in hyperspectral imagery. Therefore, we employed RF-RFE to select important bands for the spring and fall campaigns. Subsequently, we derived optimal band combinations from the combined dataset of both campaigns and then utilized them for spectral characteristic analysis in the WLD. We trained and validated RF using the 'RandomForestRegressor' function from scikit-learn. We used the default values of hyperparameters and tuned only the most sensitive parameter ('`max_features`' in 'RandomForestRegressor') in RF, due to its insensitivity to other hyperparameters (Probst et al., 2019; Kwon et al., 2022b).

2.4.4 Model validation and error metrics

We compared the three models introduced above using the combined dataset of both the Spring and Fall campaigns. We conducted the training and test for all models by randomly splitting the entire dataset into 80% for training and 20% for testing. To ensure unbiased validation, we performed a 5-fold CV using four error metrics: coefficient of determination (R^2), root mean squared error ($RMSE$), mean absolute percentage error ($MAPE$), and relative root mean squared error ($RRMSE$). The equations for each metric are as follows:

$$R^2 = 1 - \frac{\sum_i (y_i - \widehat{y}_i)^2}{\sum_i (y_i - \bar{y})^2} \tag{5}$$

$$RMSE = \sqrt{\frac{1}{n}\sum_i (y_i - \hat{y}_i)^2} \tag{6}$$

$$MAPE = \frac{1}{n}\sum_i \left| \frac{y_i - \widehat{y}_i}{\widehat{y}_i} \right| \times 100\% \tag{7}$$

$$RRMSE = \frac{RMSE}{\bar{y}} \times 100\% \tag{8}$$

To evaluate the maximum detectable depth (d_{max}), we followed the OBRA progressively truncated input depths (OPTID) framework proposed by Legleiter et al. (2018). This framework iteratively trains and validates the OBRA approach using a dataset that excludes water depth over a series of specified cutoff depths. By examining the regression results of R^2 for the excluded dataset, the inflection point can be interpreted as d_{max}. We replaced OBRA with PLSR and RFE-RF in OPTID, which can be referred to as PTID.

Using the optimal model, we further assessed the accuracy of the retrieved depth by comparing it with cross-sectional profiles of water depth obtained from ADCP, allowing the identification of d_{max}. Additionally, we used the spatial distribution of depth from a calibrated ANUGA hydrodynamic model of WLD (Wright et al., 2022) to compare the spatial distribution of modeled depth with retrieved depth map and evaluate the error in untrained regions.

2.5 Spectral analysis using SHAP

The primary disadvantage of ML is that understanding the causal relationship between input and output data is challenging owing to its black-box structure (Li, 2022). Interpretable ML has emerged as a powerful tool in data science to address the demand for understanding complex structures in ML. SHAP is one of the recent advanced explainable AI for tree-based models (Lundberg & Lee, 2017; Lundberg et al., 2020). This algorithm can describe the performance of ML with variable contributions based on game theory (Shapley, 1953) and a local explanation technique (Ribeiro et al., 2016). To estimate the contributions of variables to the model output, the SHAP value is computed as:

$$\mathrm{SHAP}_i(f) = \sum_{S \subseteq N \setminus \{i\}} \frac{|S|!(|N| - |S| - 1)!}{|N|!}[f(S \cup \{i\}) - f(S)] \tag{9}$$

where $SHAP_i(f)$ represents the SHAP value of model f for the i_{th} variable, N denotes the set of all variables, and S is a subset of variables excluding the i_{th} variable. $|S|$ represents the cardinality (the total number of elements) of the subset S, and $|N|$ is the total number of variables. $f(S \cup \{i\})$ represents the model output, including the i_{th} variable in addition to the subset S, while $f(S)$ is the model output accounting for only the variables in the subset S. The term $\frac{|S|!(|N|-|S|-1)!}{|N|!}$ serves as the probability weight of $|S|$. Lastly, $f(S \cup \{i\}) - f(S)$ is the difference between model output with and without the i_{th} variable. Therefore, the SHAP value for each variable can be interpreted as the average marginal contribution to the model prediction across all possible models with varying combinations of variables. This metric enables us to interpret how the predictions change when the values of each input variable vary.

In this study, we employed SHAP with RF to interpret spectral variability under the turbid and deep conditions of WLD. Our analysis includes the assessment of spectral band contributions and their relationship with water depth for both the Spring and Fall datasets, as well as for the combined dataset. Specifically, our analysis involves two key goals: 1) assessing the contributions of each spectral band for deep depth estimation under turbid conditions, focusing on maximum detectable depth, and 2) investigating how the RF learns from the combined dataset of the two campaigns with distinct spectral characteristics when trained collectively.

3 Results

3.1 Spectral characteristics of WLD

The reflectance spectra obtained from AVIRIS-NG during the Spring and Fall campaigns consistently exhibit high values in the visible range, from 500 to 700 nm, where absorption and attenuation within the water column are typically low (Figure 4). However, the wavelength corresponding to the maximum reflectance varies. In turbid conditions (Spring), we observed a peak near the red-edge (700 nm), associated with suspended sediment. Conversely, during fall, under clear waters with low turbidity but higher organic content (as indicated by elevated Chl-a in Table 1) due to seasonal bioproductivity (Harringmeyer et al., 2024), the maximum values are around the green (550 nm). As detailed in Table 1, we attribute this variation to the backscattering of light by suspended matters within the water column, resulting in increased reflectance under high-turbidity conditions. The notably higher reflectance around 700 nm suggests a more pronounced increase in reflectance due to the strong correlation with suspended sediments in that wavelength range (Kwon et al., 2022b).

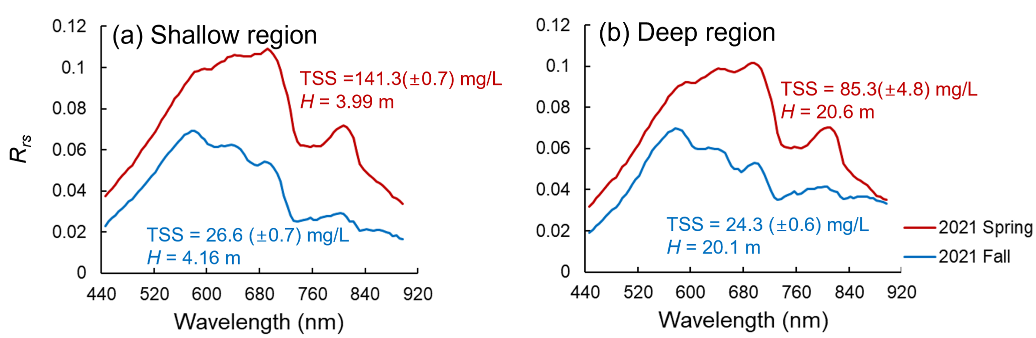

Figure 4. Reflectance spectra with varying total suspended solids (TSS) from AVRIS-NG captured in (a) shallow and (b) deep regions.

The relationships between reflectance spectra at different depths and TSS (Figure 5) show that in conditions of low turbidity, variations in reflectance due to changes in water depth are mainly observed in the falling limb of the reflectance spectrum, particularly in the near-infrared (NIR) region beyond 800 nm (Figure 5a). However, under high-turbidity conditions, reflectance differences are minor despite variations in water depth (Figure 5b). This phenomenon suggests that, in the presence of suspended matter within the water column, solar energy is unable to penetrate and is mostly reflected, highlighting the dominance of the water reflectance term in Equation (1). Nevertheless, the short blue band under 500 nm, consistent with the rising limb in Figure 5b, shows a deviation from the 1:1 line because of the depth difference. These reflectance alterations suggest that NIR and short blue bands could be effective for depth retrievals in both cases.

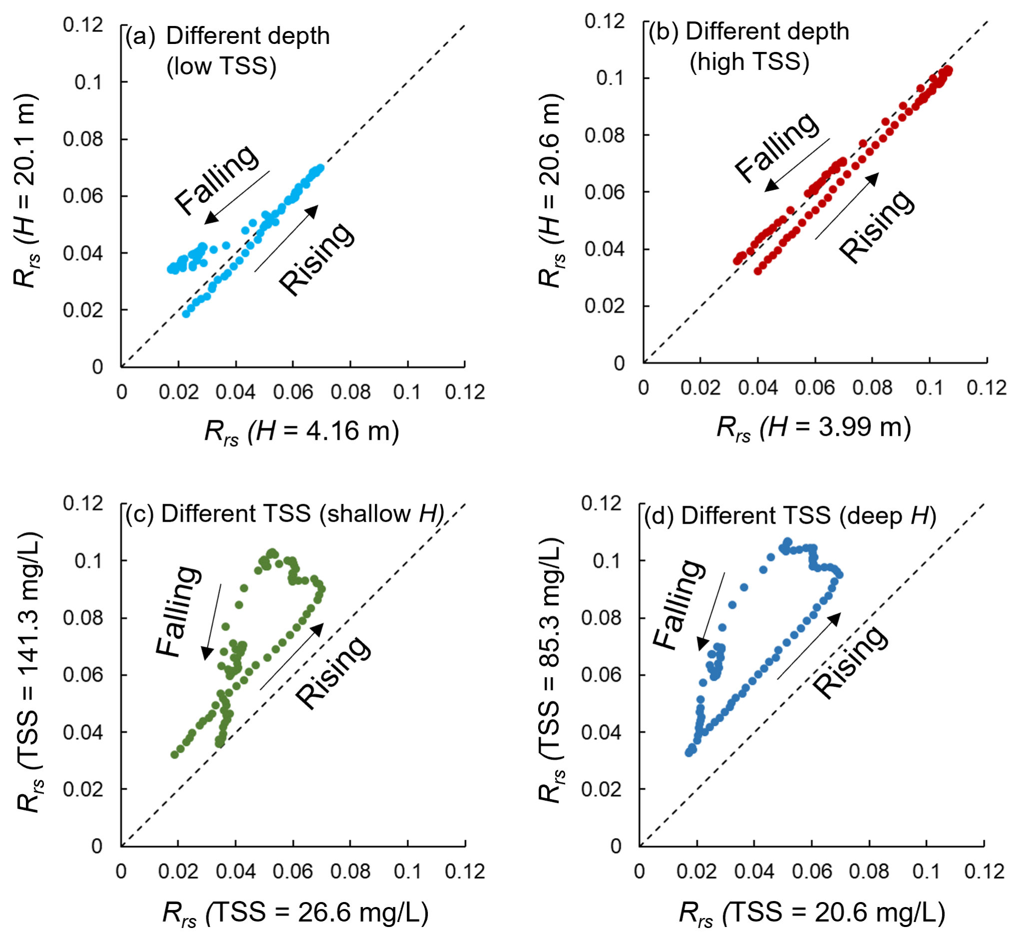

Figure 5. Spectral relationships under varying water depth (H) and TSS conditions. (a) Different depths with low TSS during the 2021 Fall campaign. (b) Different depths with high TSS during the 2021 Spring campaign. (c) Varying TSS levels in shallow regions. (d) Varying TSS levels in deep regions. Arrows indicate the rising and falling limbs in the spectra in Figure 4.

Compared to the minor effect from the depth difference, the TSS difference shows substantial effects, shaping the hysteresis loop in Figures 5c and d. This result suggests that sediment acts as a significant confounding factor in water depth retrievals. The wavelength range from 550 to 600 nm is considered relevant for bottom reflectance under the water column in various studies focusing on water depth retrievals (Legleiter & Harrison, 2019; Legleiter et al., 2016; Gwon et al., 2023; Kwon et al., 2023c; Niroumand-Jadidi et al., 2022). However, suspended sediment can substantially disrupt reflectance in this range by impeding light transmittance. This observation is consistent with our hypothesis, as discussed in Section 2.1, which posits negligible bottom reflectance in turbid and deep conditions. Therefore, the spectral characteristics of WLD during the 2021 Spring and Fall campaigns are highly complex owing to high turbidity. We provide a detailed assessment of hyperspectral retrieval performance using this dataset in the following sections.

3.2 RF performance evaluation based on sliding-window pixel averaging

Spectral images inherently contain pixel-level noise primarily due to water surface roughness (Zeng et al., 2017). Legleiter and Kinzel (2021) enhanced the texture of depth maps from RGB videos collected by helicopters and unmanned aircraft systems (UASs) through temporal and spatial averaging. They reported that temporal averaging showed superior enhancement; however, hyperspectral images are still acquired as a single-frame image. Additionally, UASs or airborne-based spectral images are more susceptible to noise due to their narrower pixel size, compared to satellite images. Therefore, here, we assessed the accuracy of RF-RFE training based on spatial averaging with sliding window sizes of 1x1, 3x3, and 5x5. The accuracy (R^2, Figure 6) increased from 0.91 to 0.94 with the 3x3 sliding window pixel averaging. The standard deviation also decreased, suggesting a more stable estimation. While a window size of 5x5 further improved accuracy, it led to an increase in standard deviation. Consequently, we determined that a window size of 3x3 is the optimal choice, balancing both accuracy and stability in our RF training.

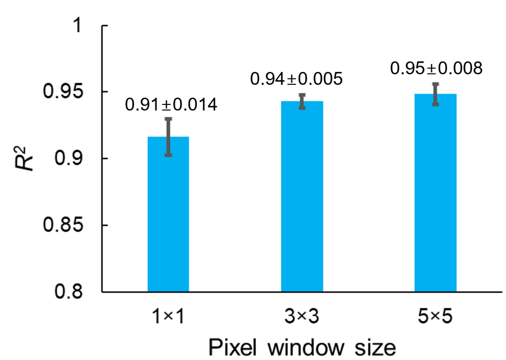

Figure 6. Comparison of model performance based on pixel window size. The results indicate average R-squared (R^2) values and their corresponding standard deviations from 5-fold cross-validation (CV).

3.3 Comparison of regression methods

We compared RF-RFE with three widely used depth retrieval algorithms, linear OBRA, exponential OBRA, and PLSR-RFE. Legleiter and Harrison (2019) reported that the exponential OBRA demonstrated better performance than other non-linear forms and has the advantage of yielding only positive depth values. Therefore, we implemented both the linear and exponential forms of OBRA for comparison. For training and testing, we used a combined dataset from both campaigns to evaluate performance in generalizing optically complex datasets. We compared the 5-fold CV results and selected wavelength, as summarized in Table 2.

Table 2. R^2 of 5-fold cross-validation (CV) and selected wavelengths of each model. The PLSR results include the calibrated number of components.

Algorithm	*CV* R^2	Selected wavelength (nm)
Linear OBRA (combined learning)	0.27±0.014	762, 832
Exponential OBRA (combined learning)	0.24±0.020	762, 832
PLSR-RFE (combined learning)	0.51±0.021	481, 541, 546, 551, 556, 561, 591, 646, 681, 702, 707, 712, 727, 732, 737, 742, 747, 752, 757, 767, 792, 797, 802, 807, 812, 877, 882, 887 (number of component = 8)
PLSR-RFE (Spring)	0.55±0.016	656, 661, 752, 762, 767, 827, 837, 862, 877, 887, 897 (number of component = 9)
PLSR-RFE (Fall)	0.58±0.014	511, 531, 541, 561, 571, 591, 641, 666, 707, 732, 737, 762, 797, 807, 852 (number of component = 9)
RF-RFE (combined learning)	0.94±0.005	446, 451, 481, 486, 531, 546, 551, 556, 561, 566, 571, 591, 707, 712, 762, 767, 882, 887, 892, 897
RF-RFE (Spring)	0.92±0.003	446, 451, 456, 461, 466, 471, 481, 486, 491, 496, 501, 511, 516, 521, 526, 531, 556, 566, 571, 586, 591, 606, 636, 651, 661, 666, 676, 681, 686, 717, 722, 747, 762, 767, 782, 832, 852, 872, 882, 887, 892, 897
RF-RFE (Fall)	0.97±0.001	486, 581, 586, 591, 696, 767, 897

Both linear and exponential OBRA select the same wavelengths and exhibit a similar distribution of correlation between water depth and band ratio for all possible band pairs (see supporting information Figure S1). The selected wavelengths are included in the NIR region, not corresponding to wavelengths commonly used in water depth retrievals. Although the accuracy is higher in the linear form, both approaches result in low accuracy with CV R^2 values of 0.27 and 0.24. We attribute this result to the weak correlation between water depth and the optimal band ratio ($X = \ln(R_{rs}(742)/R_{rs}(812))$), revealing no discernible trend in both campaigns (see supporting information Figure S2). Therefore, the plot of in-situ measured versus estimated depth from linear OBRA shows an apparent limitation in estimating depth beyond 10 m in training and testing (Figures 7a, b).

PLSR-RFE selects 28 spectral bands from a total of 91 bands across the entire wavelength range. Refer to the RFE results in Figure S3a in the supporting information. This model improves the CV R^2 to 0.51, which is twice as high as that achieved by linear OBRA (Table 2). While the OBRA shows a flat slope in the comparison plot, the depth estimated by PLSR shows better agreement with the observations, with a slope closer to 1:1 (Figures 7b, e). This enhancement results from considering a greater number of spectral bands. Specifically, this result suggests that accounting for spectral variability is crucial for training two campaign datasets with markedly different turbidity conditions. However, the overall estimated depth is underestimated, and the MAPE remains high at 77.25% and 70.08% in training and testing results, respectively. The calibrated numbers of latent variables are 8 or 9, which are high values within the calibration range (Figure S3).

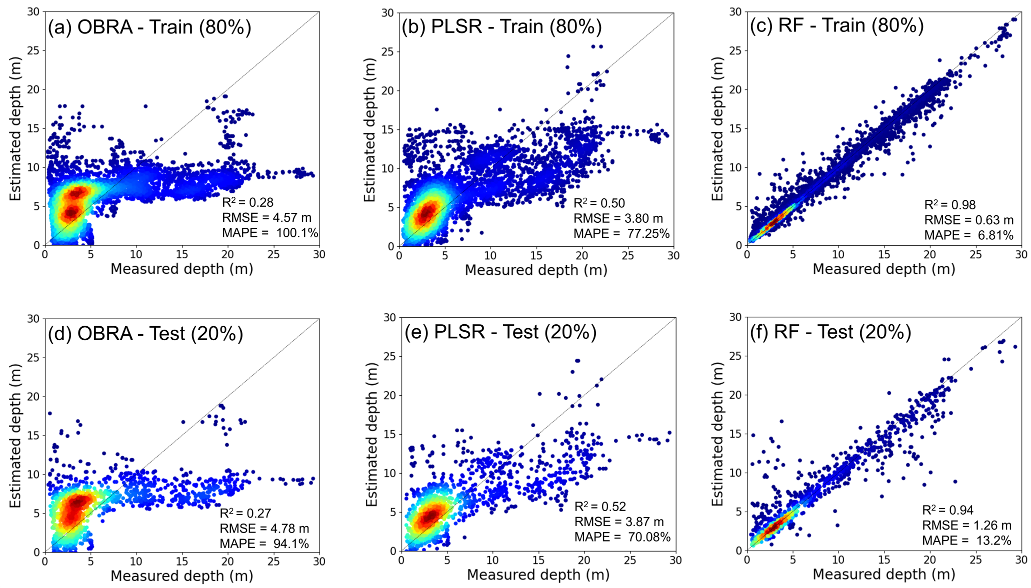

Figure 7. Comparison of models (OBRA, PLSR-RFE, and RF-RFE) for depth retrieval. (a-c) Training dataset: 80% random split. (d-f) Testing dataset: 20% random split.

This indicates the complexity of the training dataset and leads to poor generalization to new data (Jensen et al., 2019a). Furthermore, this model exhibits a particular limitation under conditions of high turbidity, as demonstrated by the poorer result in the Spring compared to that in the fall (Table 2 and Figure S3 b and c).

A comparison between OBRA and PLSR highlights the importance of learning from various spectral bands. In this context, RF substantially enhances the depth retrieval performance, achieving a CV R^2 of 0.94 by reflecting high non-linearity and learning relevant spectral bands (Table 2). The standard deviation of CV is relatively low at 0.005 compared to other methods. This result is consistent with the high correlation in the plot of in-situ measured versus estimated depth (Figures 7c and f). The MAPE values are 6.81% and 13.2%, representing more accurate results compared to other remote sensing-based depth retrievals in shallow or clear waters (Legleiter & Harrison, 2019). The noteworthy point here is that there is high consistency for estimation of depth up to approximately 30 m in both training and testing (Figure 7c, f).

By learning from the combined dataset, RF-RFE is the most accurate when it learns 20 spectral bands (Table 2). Considering the RMSE results based on the number of bands selected by RFE, the accuracy tends to converge from around 20 bands (Figure S3b). These findings imply that learning from approximately 20 bands is advisable when dealing with a diverse range of depth and turbidity conditions. Additionally, results from training RF on Spring and Fall datasets separately reveal differences in the optimal number of bands according to turbidity variations (Table 2). Under high turbidity conditions in Spring, 42 bands are selected, with a preference for both longer and shorter wavelengths—under 500 nm and beyond 700 nm. In contrast, under low turbidity conditions in Fall, only 7 bands are selected, and these bands are relatively evenly distributed across wavelengths. These findings reveal that learning a wide range of wavelengths is beneficial to estimate depth under turbid conditions, although the 550 - 600 nm bands are widely used due to a high correlation with riverbeds.

For deeper insights into the maximum detectable depth, the results of the PTID show that CV R^2 values of linear OBRA and PLSR initially decrease with the cutoff depth, and then gradually increase until reaching convergence near 15 m (Figure 8). This observed trend aligns with the findings from OPTID results in shallow and clear rivers, such as the Sacramento River in northern California and the Snake River in Wyoming, USA (Legleiter et al., 2018; Legleiter & Harrison, 2019). The absence of an inflection point implies that the depth retrieval models are robust to variations in depth range and, rather, sensitive to the dataset size. However, it is noteworthy that the CV R^2 values of OBRA and PLSR remain low and are not applicable even under shallow conditions due to high turbidity.

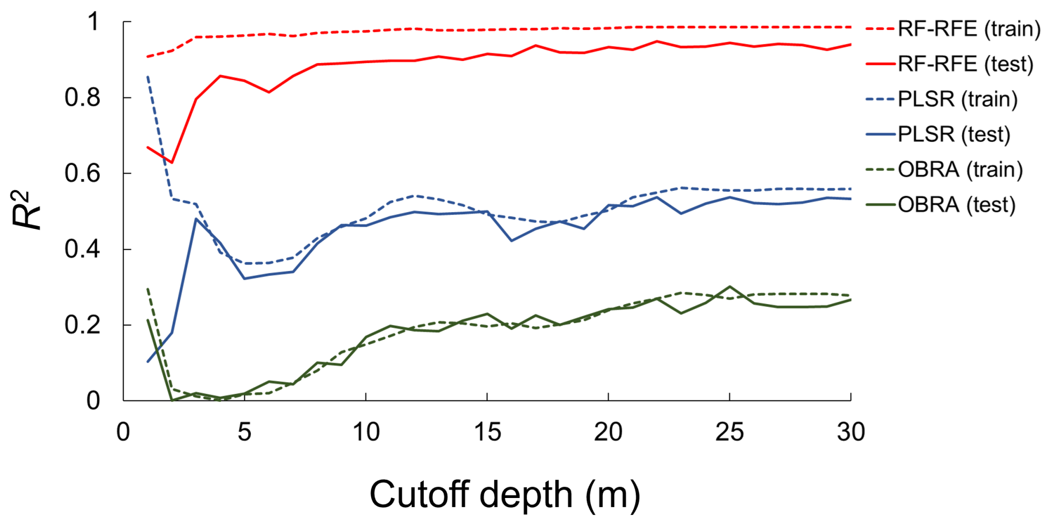

Figure 8. Model performance with progressively truncated input depths.

In contrast, RF-RFE demonstrates stable and accurate performance across the cutoff depth sampling. The CV R^2 values for training are consistently maintained above 0.9 from 2 m to 30 m. Moreover, CV R^2 values for testing gradually increase and converge, reaching stability near 8 m. This result underscores the ability of RF-RFE to be effectively trained on datasets with depths up to approximately 30 m.

3.4 Depth mapping and comparison with ADCP and a hydrodynamic model

We map the depth of both campaigns using RF-RFE with combined learning (Table 2). To estimate water depth within the wet area, we utilize the normalized difference water index (NDWI) to identify wet pixels, following the methodology outlined by Kwon et al. (2023c). Subsequently, we assess the quality of the depth map by comparing it with ADCP measurement and ANUGA hydrodynamic model results (Wright et al., 2022), particularly focusing on performance within shallow and deep regions (the retrieved depth map for the entire region during the Spring and Fall campaigns can be seen in Figures S3 and S4 in the supporting information).

To evaluate depth mapping in detail, we retrieve the cross-sectional depth profiles by the RF-RFE and compare them with ADCP measurements in both shallow ($H < 5m$) and deep regions ($H > 15m$) (Figure 9). The cross-sections exhibit irregular depth patterns attributed to dynamic sediment transport in the sediment partitioning region. Despite this irregularity, RF effectively estimates the profiles during both Spring and Fall.

In particular, the depth profiles retrieved from the image, filtered by a 3×3 window, reproduce a clear shape, even capturing the hump shape (Figure 9b) with an RRMSE under 5%. In contrast, profiles without sliding window averaging include higher noise levels, with an RRMSE twice as high. For deep cross-sections (Figures 9c and 9d), the RRMSE slightly increases; however, RF successfully retrieves depths of approximately 30 m (Figure 9c), reaching the maximum depth measured by ADCP. Therefore, this result highlights the applicability of RF-RFE to turbid and deep water conditions.

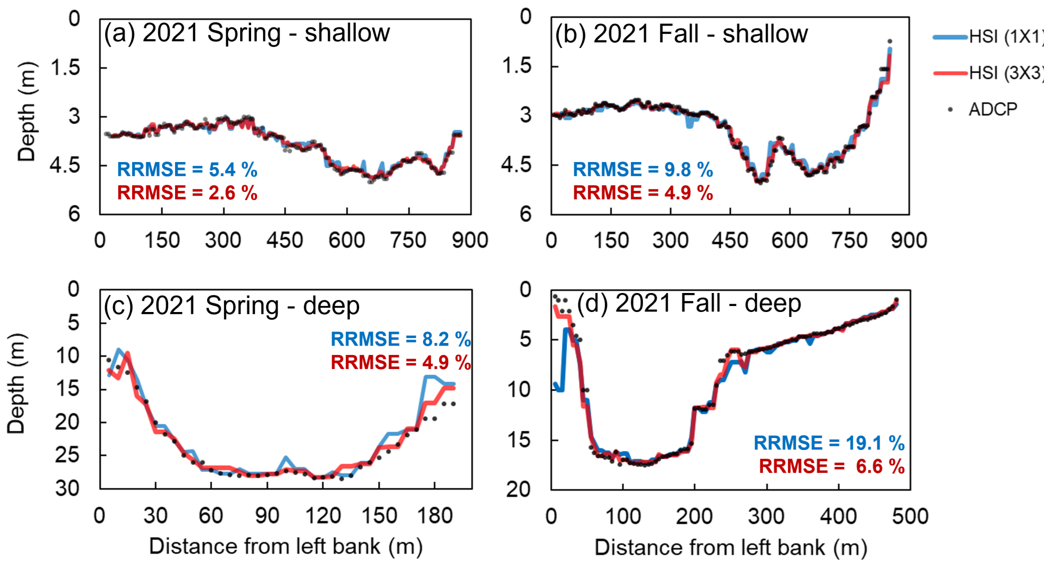

Figure 9. Comparison of depth measurements: remote sensing versus field measurements. (a-b) Shallow sections ($H_{max} < 5$m) during the 2021 Spring and Fall campaigns. (c) Deep sections ($H_{max} > 10$m) during the 2021 Spring and Fall campaigns. The blue and red lines represent results with window sizes of (1×1) and (3×3), respectively.

The retrieved depth map (Figure 10a) of the turbid case (Spring) from RF (combined learning) (Figure 10a) exhibits similar spatial patterns to ADCP measurements (Figure 2b) and the ANUGA-simulated map in both shallow and deep regions (Figure 10b). However, the difference map between both depth maps shows some disconnected and noisy regions with overestimation or underestimation in the hyperspectral retrieved map. This result could be attributed to noise in the raw image, arising from cloudiness or surface reflection. Additionally, certain areas may have entirely different water characteristics not adequately represented in the RF-RFE training data. These points will be discussed in Section 4.3.

3.5 Spectral analysis using SHAP

We can interpret the distinct spectral characteristics of AVIRIS-NG images captured during the Spring and Fall campaigns through the relative band importance derived from the RF (Figure 11). During the Spring campaign, the 446 nm wavelength, the shortest in the spectrum, is notably important. In contrast, the Fall campaign results highlight the 897 nm wavelength as the most crucial. While the spectral bands commonly used for depth estimation in the 550 - 600 nm range show some significance under both conditions, the high importance of short (446 nm) and long (897 nm) wavelengths for each campaign implies their effectiveness as discriminative factors, possibly due to variations in turbidity between the two cases. In addition, RF can generalize spectral

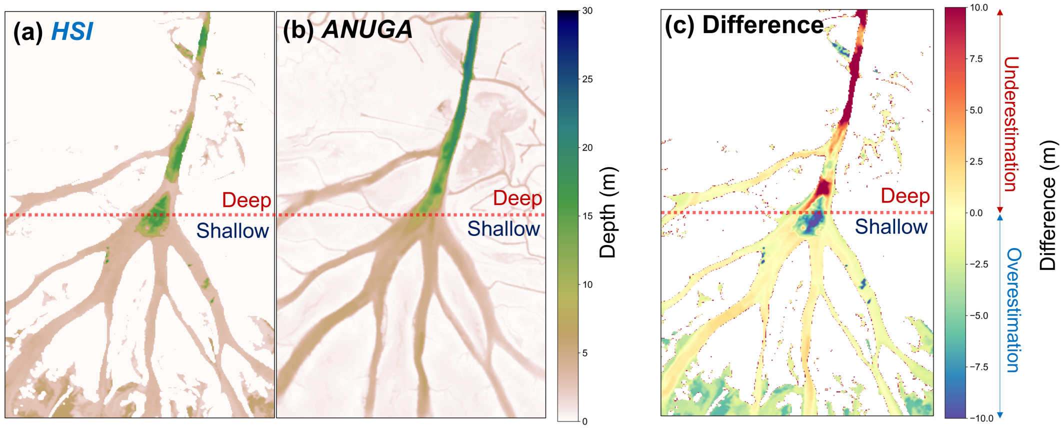

Figure 10. Spatial comparison of depth measurements in 2021 Spring campaign: (a) AVIRIS-NG versus (b) ANUGA. (c) Difference map.

variability from both cases within a single model by incorporating all crucial bands identified in each instance (Figure 11b). The most critical bands for the RF, trained using a combined dataset, are related to high attenuation (446, 897 nm), sediment (712 nm), and riverbed (531 nm). The red-edge (712 nm) and green (531 nm) bands are typically used for suspended sediment and depth retrievals, respectively (Kwon et al., 2022a; Legleiter et al., 2009b), but they are less important than the high attenuation bands (446, 897 nm) (Pegau et al., 1997) under deep and turbid water conditions. The variation in chl-a between the campaigns is linked to the significance of the long green (571 nm) band, which typically peaks at high chl-a concentrations (Pahlevan et al., 2020; Pyo et al., 2018). However, in conditions of high turbidity and low chl-a during Spring, the 571 nm band gains more importance. Conversely, under low turbidity and high chl-a conditions during Fall, the 712 nm band becomes more prominent. This distinction results from the ability to filter out sediment and organic effects that hinder accurate depth measurement.

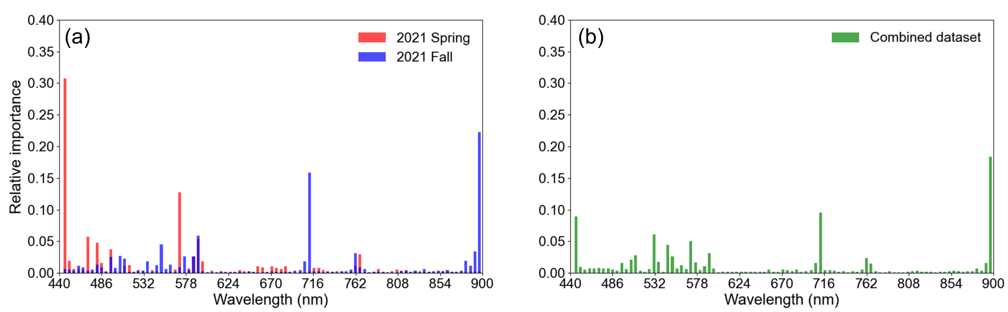

Figure 11. Relative importance of spectral bands estimated by RF. (a) Importance from separately trained RF for each campaign. (b) Importance from RF trained on a combined dataset of both campaigns.

The SHAP results provide a deeper interpretation of the causal relationship between depth and spectral bands within RF showing how the top 20 key spectral bands influence the model output (Figure 12). Here, the SHAP values indicate the degree to which spectral bands impact the model output – a positive value increases the predicted value (related to deep depth), while a negative value decreases it (related to shallow depth). Notably, the selected key bands for Spring and Fall were similar, but their influences, as observed in the distribution of SHAP values, exhibited different trends.

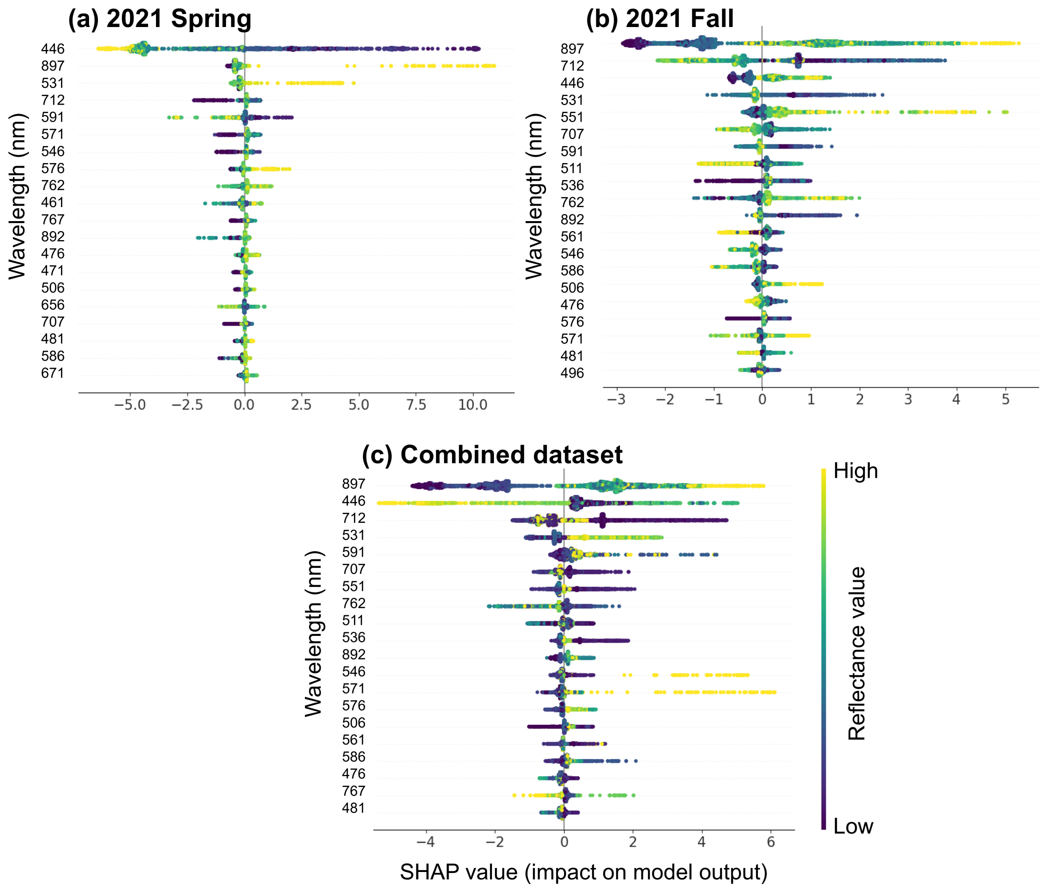

Figure 12. SHAP summary plot from trained RF representing the impact of each spectral band on model output. This graph ranks the top 20 most important bands by their SHAP value. The colorbar represents the relative value of reflectance.

In the case of Spring, the short blue (446 nm) band is the most significant and decreases the predicted depth. The dominance of its influence is evident through the wide range of SHAP values. Shorter blue wavelengths under 450 nm are highly sensitive to turbid factors (e.g., suspended sediment, organic matter) due to the higher absorption and attenuation coefficients within the water column. Conversely, the NIR band (897 nm) increases the model output, indicating a strong relationship with deeper depths. Both 446 nm and 897 nm are closely associated with water column absorption and attenuation, but 897 nm is more affected by water turbidity. Therefore, owing to the high turbidity in Spring, the 446 nm band played a more crucial role than the 897 nm band.

In the Fall, the NIR band (897 nm) is the most crucial band, and it has a strong positive correlation with the predicted depth while showing a negative relationship with model output. This disparity can be attributed to the low turbidity conditions in the Fall. Low turbidity can strengthen the attenuation of the NIR bands, thereby increasing the transmittance of these bands. This effect is also consistent with the low R_{rs} value observed in the reflectance spectrum (Figure 4). Despite the dominance of high attenuation bands (446 nm and 897 nm), other bands also demonstrate non-negligible importance. This result implies a high degree of spectral variability in each case. The SHAP results from the RF model with combined learning (Figure 12c) show that the diverse impacts of each spectral band are effectively reflected by the RF model, with the important band ranking consistent with the result of the individual campaigns. Notably, both 446 nm and 897 nm bands emerge as the top two significant variables, further affirming their significant role in accounting for the differences between the two cases. The NIR band (897 nm) is typically affected by temperature, potentially influencing its role for individual campaigns (Pegau et al., 1997).

The SHAP dependence plot provides additional insight into the relationship between crucial bands (446 nm, 897 nm, and 712 nm) and water depth. The 446 nm band shows a clear negative correlation with the SHAP value under high turbidity conditions (Figure 13a); this correlation is attributed to its high correlation with the NIR band, arising from a shared feature of high attenuation. Although the SHAP value trends are not clear when turbidity is low, we observe some high positive values when reflectance values are high (Figure 13b). These SHAP values indicate that the short blue band is associated with both shallow and deep ranges under high turbid conditions. However, under low turbidity, its correlation is limited to specific deep regions.

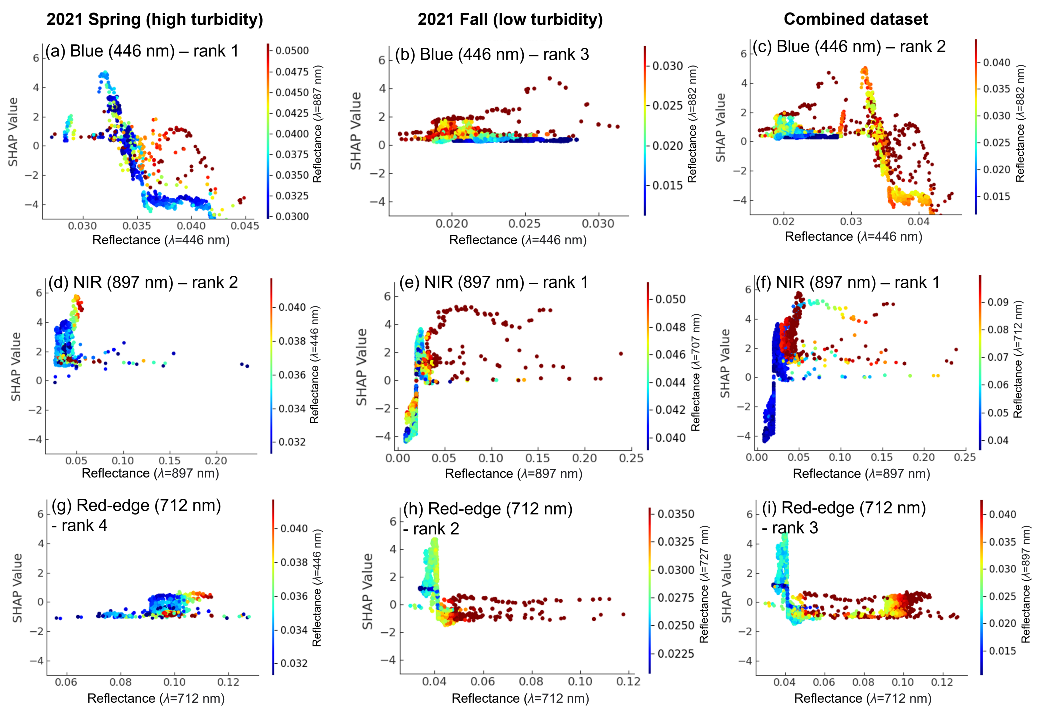

Figure 13. SHAP dependence plot to understand the contribution of high-ranked bands in Spring, Fall, and combined datasets: (a-c) Blue band (446 nm), (d-f) NIR band (897 nm), (g-i) Red-edge band (712 nm). The colorbar shows the corresponding most correlated band and the red box indicates the sensitive SHAP value range.

In both Spring and Fall, the 897 nm band exhibits a positive correlation with SHAP values (Figures 13d and e). However, in both cases, it shows linearity only at reflectance values below 0.05 and irregular trends beyond that point. Moreover, under high turbidity conditions, it consistently shows positive SHAP values. Conversely, the 712 nm band, closely linked to sediment, demonstrates high SHAP values only when reflectance is below 0.05 under low turbidity (Figures 13g and h). This result suggests that, in the case of high turbidity, the 446 nm and 897 nm bands having higher attenuation coefficients in the water column, are more important for deep-depth estimation than the 712 nm band related to sediment. This result aligns with the hypothesis of this study that water column reflectance can be used for depth retrievals due to its relationship as exponential attenuation with water depth (see Section 2.1).

Notably, in the results from the combined dataset, these distinctly different patterns overlap, indicating that the model can account for the spectral variability of both datasets (Figures 13c, f, and i). This result reveals that RF is capable of learning complex datasets by effectively handling them through data separation, as shown in the color difference in the plot, similar to a clustering approach.

4 Discussion

4.1 Transferability of hyperspectral retrievals for depth mapping

Hyperspectral depth retrievals can be a strong alternative to depth surveys by offering detailed spatial information. However, several limitations need to be addressed, including performance under optically complex conditions, before they can be applied to a variety of settings.This study revealed the feasibility of hyperspectral retrievals even in deep and turbid conditions, one of the most challenging tasks for a remote sensing approach. We showed that combining learning of spectral data under vastly different conditions is feasible at WLD. The Spring campaign case with high turbidity resulted in a CV R^2 of 0.92. Interestingly, when trained with the Fall campaign case with lower turbidity, the CV R^2 increased to 0.94. Despite such improvement, we also identified several constraints and inherent limitations in passive remote sensing using an empirical approach. As indicated by the SHAP results, transferring separate models with substantially different turbidity conditions is challenging. Spectral analysis revealed that when turbidity varies by approximately fourfold, the spectral characteristics change significantly. Consequently, although SHAP rankings for key bands were similar between spring and fall, their relationship with model output (water depth) was markedly different, as depicted in the dependence plot (Figure 13). This strong dependence on the learning dataset is an inherent disadvantage. Therefore, while transferability might exist for separately trained models under similar conditions, achieving global applicability within the trained region necessitates learning across various conditions through combined learning. The consistency in results between separate and combined learning indicates the potential for continuous improvement through learning from various datasets, as demonstrated in Table 2.

To develop a model applicable to various conditions, it is necessary to collect more diverse data. In particular, confounding factors of water quality (e.g., suspended sediment, CDOM, and chlorophyll) substantially affect spectral characteristics, as they directly influence the inherent optical properties (IOPs) such as the absorption and backscattering coefficients of water (Fan et al., 2015; Woźniak & Stramski, 2004). In the cases shown in this study, we observed significant variations in water depth, but not in water quality parameters. Hence, future studies should analyze the impact of variability in other water quality parameters on the transferability of the depth retrieval model. The AVIRIS-NG images used in this study covered a large deltaic area. Acquiring frequent drone or airborne images requires significant effort. Therefore, for a more comprehensive analysis of spatial variability, we expect that hyperspectral or multispectral satellite imagery covering a wide area will provide deeper insights. To account for spatial variability in water quality, spectral clustering can classify each river based on water quality, as reported in the spectral clustering-based regression method in a confluence (Kwon et al., 2023b), and divide the region according to spectral similarity.

Additionally, we need a more comprehensive understanding of the spectral characteristics of deep and turbid waters, where depth retrievals rely solely on water column reflectance. The wavelength of the most important bands, 446 nm in Spring and 867 nm in Fall, typically demonstrate high attenuation, and these bands showed a strong correlation with a wide range of water depths (Figures 13a and e). However, the dominant wavelength range varied significantly among different rivers. Hence, future studies should include measuring IOPs within specific wavelength ranges to analyze the relationship between attenuation and depth in deep and turbid conditions.

4.2 Maximum detectable depth from hyperspectral remote sensing

As depicted in Figure 9c, we found the maximum detectable depth from AVIRIS-NG to be approximately 30 m, even in turbid conditions—a significant finding that positions the proposed approach as a promising method compared to other remote sensing techniques. Among the various imaging spectroscopy approaches, our results show an enhancement compared to the approximately 4 m of maximum depth reported in previous research (Legleiter & Harrison, 2019). This enhancement suggests that remote sensing-based depth retrievals can be further improved owing to the rapid development of platforms, sensors, and algorithms. The relationship between reflectance and depth is affected by the depth range, as represented in Equation (1). Therefore, learning various spectral bands and non-linearity is crucial to account for the complexity arising from varied depths, which can be achieved by ML.

Recent advancements in sensors and algorithms have significantly improved the accuracy and reliability of lidar-based bathymetry (Chen et al., 2021; Zhang et al., 2022; Xie et al., 2023). Chen et al. (2021) introduced a novel algorithm, the adaptive variable ellipse filtering bathymetric method (AVEBM), for lidar applications. Employing this method, they demonstrated the capabilities of the ICESat-2 equipped with the ATLAS, which incorporates a photon-counting technique, to enhance water depth estimation to approximately 17 m. Notably, this evaluation was conducted under clear water conditions. Turbidity poses significant challenges for lidar performance, especially considering its utilization of a single wavelength, typically green. The imaging spectroscopy approach could be more effective for deep water detection under turbid conditions because of the range of wavelengths included. Spectral bands across 446 to 897 nm contribute to the model learning performance (Figure 12c). Green bands should be among those sensitive to water quality parameters like chlorophyll and CDOM.

This study used only the data collected during the 2021 Spring and Fall campaigns in WLD; thus, further evaluation under more diverse conditions is necessary. During these campaigns, TSS was the dominant factor influencing reflectance spectra shapes (Figure 5). This result suggests that we need further evaluation of the maximum detectable depth according to TSS or turbidity. In addition, unavailability of imagery during cloudy and rainy weather is an inherent disadvantage of passive remote sensing. Therefore, the selection of sensors for coastal remote sensing should be flexible, taking into account the objectives of the study and the surrounding environment.

4.3 Control factors for depth mapping quality

When comparing the depth maps from AVIRIS-NG and ANUGA (Figure 10), we observed discontinuous regions in the deep river areas. The RF model demonstrated high accuracy not only with the training data but also with test data and cross-validation (Figure 7 and Table 2). This result indicates that the model performs well in retrieving the ADCP-measured locations. However, the estimation of deep water depth can be quite susceptible to subtle variations in reflectance. Under deep water depth, alterations in depth were primarily observable in the short blue (446 nm) or NIR (897 nm) bands (Figure 5), where the attenuation coefficient is high. Moreover, under high turbidity, these depth-related changes were minimal, implying that RF learned this subtle difference.

The averaged reflectance spectra of the discontinuous areas (underestimated areas) and the normal deep areas of the Spring campaign (Figure S6a) show that, however, the reflectance difference was not substantial. The difference plot (Figure S6b) indicates that the main differences occurred within the short blue and NIR wavelengths. This difference is close to the contrast between the shallow (approximately 4 m) and deep (approximately 20 m) areas within these wavelength ranges (Figure S6b). Considering the subtle effects of depth difference on reflectance under turbid conditions (Figure 5b), this slight difference can lead to the underestimation of depth.

Reflectance with high attenuation is highly sensitive to noise, which cannot be overcome by atmospheric correction (Vanhellemont, 2019). Additionally, variations in airborne altitude, pitch, and roll along each flight path can influence the viewing geometry between the sensor and the observed surface, thereby slightly influencing the BRDF effects in the acquired spectra.

Addressing the correction of discontinuous regions in deep areas is an important direction for future studies. Establishing a relationship between water level and river width in deep regions through remote sensing products can provide valuable insights for correction (Wu et al., 2023). This approach involves estimating depth in discontinuous regions and subsequently integrating this information with the depth map. Additionally, a fusion approach could involve integrating lidar-derived water level maps. This method would allow the correction of error-prone areas and could be used to convert spectrally estimated depths to water levels. The Surface Water and Ocean Topography (SWOT) mission is providing greatly improved spatiotemporal data on surface elevation of global water bodies (Liu et al., 2024). Coupling imaging spectroscopy and SWOT data can make bathymetry mapping more accessible worldwide and enhance the potential for high resolution and repeat morphological monitoring of deltaic dynamic systems.

5 Concluding remarks

Retrieving water depth in turbid and deep waters is one of the most challenging tasks in coastal remote sensing. To explore the potential of imaging spectroscopy for depth mapping in such demanding conditions, we evaluated ML-based hyperspectral retrievals using AVIRIS-NG imagery in the WLD. Combining the RF-RFE with SHAP, this study investigated the spectral variability of deep and turbid waters, focusing on the influence of key spectral bands on depth estimation in these challenging conditions. Our result support five key findings as follows:

1. The study revealed intricate spectral characteristics of WLD in deep and turbid conditions, highlighting variations in reflectance spectra influenced by suspended sediment and water depth. Notably, this study highlighted that reflectance spectra showed subtle differences against depth variations under turbid conditions, while the TSS variations induced high variability. Nevertheless, we found the short blue (446 nm) and NIR (897 nm) bands to be key variables for deep water retrievals.
2. RF-RFE successfully generalized two different campaign datasets, producing robust depth retrieval across the WLD. This result was achieved through the advantages of multi-band learning and non-linearity learning. The RF-RFE achieved a high CVR^2 of 0.94±0.005 for the combined learning, outperforming other regression methods (OBRA and PLSR).
3. The application of RF-RFE for depth mapping showed accurate depth estimation, even in irregular and deep cross-sections. This model revealed a significant improvement in the maximum detectable depth, reaching approximately 30 m even in turbid conditions.

4. A SHAP analysis suggested that various spectral bands are necessary to address spectral variability arising from turbidity and varied depth range. Notably, the short blue and NIR bands emerged as the most dominant across the entire depth range, implying the significance of attenuation within the water column in deep and turbid conditions.
5. The effective bands were similar for each campaign regardless of turbidity, but their relationship with water depth was substantially different. The SHAP dependence plot showed that combined learning of RF-RFE enables the model to effectively handle spectral variability in complex datasets.

The study also found limitations in deep-depth retrievals under turbid conditions. Due to the high dependency on short blue and NIR bands, subtle variations in reflectance values induced by weather and water surface conditions could be crucial for accurate depth mapping. Therefore, correcting discontinuous regions in deep areas needs further investigation. A fusion of multi-remote sensing products could be beneficial to achieve more robust and accurate depth mapping.

Conflict of Interest

The authors declare no conflicts of interest relevant to this study.

Data Availability Statement

ADCP water depth data are available for download from the ORNL DAAC at `https://doi.org/10.3334/ORNLDAAC/2081`. Similarly, AVIRIS-NG L2B BRDF-adjusted surface reflectance data can be accessed from the ORNL DAAC at `https://doi.org/10.3334/ORNLDAAC/2139`. The processing codes can be found at `https://github.com/siyoonk/Kwon_Depth_mapping_WLD`.

Acknowledgments
This work was supported by the NASA Delta-X project, which is funded by the Science Mission Directorate's Earth Science Division through the Earth Venture Suborbital-3 Program (NNH17ZDA001N-EVS3) and the National Research Foundation of Korea (NRF) grant funded by the Korean government (MSIT) (RS-2023-00209539).

References

Baek, D., Seo, I. W., Kim, J. S., & Nelson, J. M. (2019). UAV-based measurements of spatio-temporal concentration distributions of fluorescent tracers in open channel flows. *Advances in Water Resources*, *127*, 76–88. Retrieved from `https://doi.org/10.1016/j.advwatres.2019.03.007` doi: 10.1016/j.advwatres.2019.03.007

Breiman, L. (2001). Random forests. *Machine Learning*, *45*, 5–32. Retrieved from `https://doi.org/10.1023/A:1010933404324` doi: 10.1023/A:1010933404324

Bruegge, C. J., Thomas Arnold, G., Czapla-Myers, J., Dominguez, R. A., Helmlinger, M. C., Thompson, D. R., . . . Wenny, B. N. (2021). Vicarious Calibration of eMAS, AirMSPI, and AVIRIS Sensors during FIREX-AQ. *IEEE Transactions on Geoscience and Remote Sensing*, *59*(12), 10286–10297. doi: 10.1109/TGRS.2021.3066997

Caballero, I., & Stumpf, R. P. (2023). Confronting turbidity, the major challenge for satellite-derived coastal bathymetry. *Science of The Total Environment*, *870*, 161898. Retrieved from `https://www.sciencedirect.com/`

science/article/pii/S0048969723005132 doi: https://doi.org/10.1016/j.scitotenv.2023.161898

Cao, Z., Ma, R., Duan, H., Pahlevan, N., Melack, J., Shen, M., & Xue, K. (2020). A machine learning approach to estimate chlorophyll-a from Landsat-8 measurements in inland lakes. *Remote Sensing of Environment*, *248*(October 2019), 111974. Retrieved from https://doi.org/10.1016/j.rse.2020.111974 doi: 10.1016/j.rse.2020.111974

Carrascal, L. M., Galván, I., & Gordo, O. (2009). Partial least squares regression as an alternative to current regression methods used in ecology. *Oikos*, *118*(5), 681-690. doi: https://doi.org/10.1111/j.1600-0706.2008.16881.x

Chapman, J. W., Thompson, D. R., Helmlinger, M. C., Bue, B. D., Green, R. O., Eastwood, M. L., ... Lundeen, S. R. (2019). Spectral and radiometric calibration of the next generation airborne visible infrared spectrometer (aviris-ng). *Remote Sensing*, *11*(18). Retrieved from https://www.mdpi.com/2072-4292/11/18/2129 doi: 10.3390/rs11182129

Chen, Y., Le, Y., Zhang, D., Wang, Y., Qiu, Z., & Wang, L. (2021). A photon-counting lidar bathymetric method based on adaptive variable ellipse filtering. *Remote Sensing of Environment*, *256*, 112326. Retrieved from https://www.sciencedirect.com/science/article/pii/S0034425721000444 doi: https://doi.org/10.1016/j.rse.2021.112326

Christensen, A., Mallard, J., Nghiem, J., Simard, M., Pavelsky, T., & Lamb, M. (2022). *Delta-x: Acoustic doppler current profiler channel surveys, mrd, louisiana, 2021, v2. ornl daac, oak ridge, tennessee, usa.*

de Almeida, C. T., Galvão, L. S., Aragão, L. E. d. O. C. e., Ometto, J. P. H. B., Jacon, A. D., Pereira, F. R. d. S., ... Longo, M. (2019). Combining LiDAR and hyperspectral data for aboveground biomass modeling in the Brazilian Amazon using different regression algorithms. *Remote Sensing of Environment*, *232*(March), 111323. Retrieved from https://doi.org/10.1016/j.rse.2019.111323 doi: 10.1016/j.rse.2019.111323

Demarchi, L., Kania, A., Ciezkowski, W., Piórkowski, H., Oświecimska-Piasko, Z., & Chormański, J. (2020). Recursive feature elimination and random forest classification of natura 2000 grasslands in lowland river valleys of poland based on airborne hyperspectral and LiDAR data fusion. *Remote Sensing*, *12*(11). doi: 10.3390/rs12111842

Dethier, E. N., Renshaw, C. E., & Magilligan, F. J. (2020). Toward Improved Accuracy of Remote Sensing Approaches for Quantifying Suspended Sediment: Implications for Suspended-Sediment Monitoring. *Journal of Geophysical Research: Earth Surface*, *125*(7). doi: 10.1029/2019JF005033

Fan, Y., Li, W., Calzado, V. S., Trees, C., Stamnes, S., Fournier, G., ... Stamnes, K. (2015). Inferring inherent optical properties and water constituent profiles from apparent optical properties. *Optics Express*, *23*(15), A987. doi: 10.1364/oe.23.00a987

Fichot, C., Harringmeyer, J., & Weiser, M. (2022). *Delta-X: In Situ Water Quality Indicators across MRD, LA, USA, 2021, Version 2.* https://doi.org/10.3334/ORNLDAAC/2080. ORNL DAAC, Oak Ridge, Tennessee, USA.

Gao, B.-C., & Li, R.-R. (2021). Correction of Sunglint Effects in High Spatial Resolution Hyperspectral Imagery Using SWIR or NIR Bands and Taking Account of Spectral Variation of Refractive Index of Water. *Advances in Environmental and Engineering Research*, *02*(03). doi: 10.21926/aeer.2103017

Greenberg, E., Thompson, D. R., Jensen, D., Townsend, P. A., Queally, N., Chlus, A., ... Simard, M. (2022). An Improved Scheme for Correcting Remote Spectral Surface Reflectance Simultaneously for Terrestrial BRDF and Water-Surface Sunglint in Coastal Environments. *Journal of Geophysical Research: Biogeosciences*, *127*(3), 1–21. doi: 10.1029/2021JG006712

Guyon, I., Weston, J., Barnhil, l. S., & Vapnik, V. (2002). Gene selection for cancer

classification using support vector machines. *Machine Learning*, *46*, 389–422.
Gwon, Y., Kwon, S., Kim, D., Seo, I. W., & You, H. (2023). Estimation of shallow stream bathymetry under varying suspended sediment concentrations and compositions using hyperspectral imagery. *Geomorphology*, *433*, 108722.
Harringmeyer, J. P., Ghosh, N., Weiser, M. W., Thompson, D. R., Simard, M., Lohrenz, S. E., & Fichot, C. G. (2024). A hyperspectral view of the nearshore Mississippi River Delta: Characterizing suspended particles in coastal wetlands using imaging spectroscopy. *Remote Sensing of Environment*, *301*(November 2023). doi: 10.1016/j.rse.2023.113943
Harrison, L. R., Legleiter, C. J., Sridharan, V. K., Dudley, P. N., & Daniels, M. E. (2022). Evaluating the Sensitivity of Multi-Dimensional Model Predictions of Salmon Habitat to the Source of Remotely Sensed River Bathymetry. *Water Resources Research*, *58*(12), 1–20. doi: 10.1029/2022WR033097
Hestir, E. L., Brando, V. E., Bresciani, M., Giardino, C., Matta, E., Villa, P., & Dekker, A. G. (2015). Measuring freshwater aquatic ecosystems: The need for a hyperspectral global mapping satellite mission. *Remote Sensing of Environment*, *167*, 181–195. Retrieved from `http://dx.doi.org/10.1016/j.rse.2015.05.023` doi: 10.1016/j.rse.2015.05.023
Hiatt, M., & Passalacqua, P. (2015). Hydrological connectivity in river deltas: The first-order importance of channel-island exchange. *Water Resources Research*, *51*(4), 2264-2282. Retrieved from `https://agupubs.onlinelibrary.wiley.com/doi/abs/10.1002/2014WR016149` doi: https://doi.org/10.1002/2014WR016149
Hossain, F., Das, P., Srinivasan, M., Tsontos, V., Oaida, C. M., Nickles, C., ... Pavelsky, T. (2022). Building user-readiness for satellite earth observing missions: The case of the surface water and ocean topography (swot) mission. *AGU Advances*, *3*(6), e2022AV000680. Retrieved from `https://agupubs.onlinelibrary.wiley.com/doi/abs/10.1029/2022AV000680` (e2022AV000680 2022AV000680) doi: https://doi.org/10.1029/2022AV000680
Jensen, D., Cavanaugh, K. C., Simard, M., Okin, G. S., Castañeda-Moya, E., McCall, A., & Twilley, R. R. (2019b). Integrating imaging spectrometer and synthetic aperture radar data for estimating wetland vegetation aboveground biomass in coastal Louisiana. *Remote Sensing*, *11*(21). doi: 10.3390/rs11212533
Jensen, D., Simard, M., Cavanaugh, K., Sheng, Y., Fichot, C. G., Pavelsky, T., & Twilley, R. (2019a). Improving the transferability of suspended solid estimation in wetland and deltaic waters with an empirical hyperspectral approach. *Remote Sensing*, *11*(13). doi: 10.3390/RS11131629
Kim, W., Mohrig, D., Twilley, R., Paola, C., & Parker, G. (2009). Is it feasible to build new land in the mississippi river delta? *Eos, Transactions American Geophysical Union*, *90*(42), 373-374. Retrieved from `https://agupubs.onlinelibrary.wiley.com/doi/abs/10.1029/2009EO420001` doi: https://doi.org/10.1029/2009EO420001
Kuenzer, C., Heimhuber, V., Huth, J., & Dech, S. (2019). Remote sensing for the quantification of land surface dynamics in large river delta regions—a review. *Remote Sensing*, *11*(17). Retrieved from `https://www.mdpi.com/2072-4292/11/17/1985` doi: 10.3390/rs11171985
Kwon, S., Gwon, Y., Kim, D., Seo, I. W., & You, H. (2023c). Unsupervised classification of riverbed types for bathymetry mapping in shallow rivers using uav-based hyperspectral imagery. *Remote Sensing*, *15*(11). Retrieved from `https://www.mdpi.com/2072-4292/15/11/2803` doi: 10.3390/rs15112803
Kwon, S., Noh, H., Seo, I. W., & Park, Y. S. (2023a). Effects of spectral variability due to sediment and bottom characteristics on remote sensing for suspended sediment in shallow rivers. *Science of The Total Environment*, *878*, 163125.
Kwon, S., Seo, I. W., & Lyu, S. (2023b). Investigating mixing patterns of suspended

sediment in a river confluence using high-resolution hyperspectral imagery. *Journal of Hydrology*, *620*, 129505.

Kwon, S., Seo, I. W., Noh, H., & Kim, B. (2022b). Hyperspectral retrievals of suspended sediment using cluster-based machine learning regression in shallow waters. *Science of The Total Environment*, *833*, 155168.

Kwon, S., Shin, J., Seo, I. W., Noh, H., Jung, S. H., & You, H. (2022a). Measurement of suspended sediment concentration in open channel flows based on hyperspectral imagery from uavs. *Advances in Water Resources*, *159*, 104076. Retrieved from `https://www.sciencedirect.com/science/article/pii/S0309170821002281` doi: https://doi.org/10.1016/j.advwatres.2021.104076

Lee, Z., Carder, K. L., & Arnone, R. A. (2002). Deriving inherent optical properties from water color: a multiband quasi-analytical algorithm for optically deep waters. *Applied Optics*, *41*(27), 5755. doi: 10.1364/ao.41.005755

Lee, Z., Carder, K. L., Mobley, C. D., Steward, R. G., & Patch, J. S. (1999). Hyperspectral remote sensing for shallow waters: 2 Deriving bottom depths and water properties by optimization. *Applied Optics*, *38*(18), 3831. doi: 10.1364/ao.38.003831

Legleiter, C. J., & Harrison, L. R. (2019). Remote Sensing of River Bathymetry: Evaluating a Range of Sensors, Platforms, and Algorithms on the Upper Sacramento River, California, USA. *Water Resources Research*, *55*(3), 2142–2169. doi: 10.1029/2018WR023586

Legleiter, C. J., King, T. V., Carpenter, K. D., Hall, N. C., Mumford, A. C., Slonecker, T., ... Rosen, B. H. (2022). Spectral mixture analysis for surveillance of harmful algal blooms (SMASH): A field-, laboratory-, and satellite-based approach to identifying cyanobacteria genera from remotely sensed data. *Remote Sensing of Environment*, *279*(November 2021), 113089. Retrieved from `https://doi.org/10.1016/j.rse.2022.113089` doi: 10.1016/j.rse.2022.113089

Legleiter, C. J., & Kinzel, P. J. (2021). Improving Remotely Sensed River Bathymetry by Image-Averaging. *Water Resources Research*, *57*(3). doi: 10.1029/2020WR028795

Legleiter, C. J., Overstreet, B. T., & Kinzel, P. J. (2018). Sampling strategies to improve passive optical remote sensing of river bathymetry. *Remote Sensing*, *10*(6), 1–24. doi: 10.3390/rs10060935

Legleiter, C. J., Roberts, D. A., & Lawrence, R. L. (2009b). Spectrally based remote sensing of river bathymetry. *Earth Surface Processes and Landforms*, *34*(March), 1039–1059. Retrieved from `10.1002/esp.1787%0ATart` doi: 10.1002/esp.1787Tart

Legleiter, C. J., Roberts, D. A., Marcus, W. A., & Fonstad, M. A. (2004). Passive optical remote sensing of river channel morphology and in-stream habitat: Physical basis and feasibility. *Remote Sensing of Environment*, *93*(4), 493–510. doi: 10.1016/j.rse.2004.07.019

Legleiter, C. J., Stegman, T. K., & Overstreet, B. T. (2016). Spectrally based mapping of riverbed composition. *Geomorphology*, *264*, 61–79. Retrieved from `http://dx.doi.org/10.1016/j.geomorph.2016.04.006` doi: 10.1016/j.geomorph.2016.04.006

Li, Z. (2022). Extracting spatial effects from machine learning model using local interpretation method: An example of SHAP and XGBoost. *Computers, Environment and Urban Systems*, *96*(June), 101845. Retrieved from `https://doi.org/10.1016/j.compenvurbsys.2022.101845` doi: 10.1016/j.compenvurbsys.2022.101845

Liu, K., Song, C., Zhao, S., Wang, J., Chen, T., Zhan, P., ... Zhu, J. (2024). Mapping inundated bathymetry for estimating lake water storage changes from SRTM DEM: A global investigation. *Remote Sensing of Environment*, *301*(September 2023), 113960. Retrieved from `https://doi.org/10.1016/`

j.rse.2023.113960 doi: 10.1016/j.rse.2023.113960
Lundberg, S. M., Erion, G., Chen, H., & et al. (2020). From local explanations to global understanding with explainable ai for trees. *Nature Machine Intelligence*, *2*, 56–67. doi: 10.1038/s42256-019-0138-9
Lundberg, S. M., & Lee, S.-I. (2017). A unified approach to interpreting model predictions. In I. Guyon et al. (Eds.), *Advances in neural information processing systems* (Vol. 30). Curran Associates, Inc. Retrieved from https://proceedings.neurips.cc/paper_files/paper/2017/file/8a20a8621978632d76c43dfd28b67767-Paper.pdf
McKean, J., Tonina, D., Bohn, C., & Wright, C. (2014). Effects of bathymetric lidar errors on flow properties predicted with a multi-dimensional hydraulic model. *Journal of Geophysical Research: Earth Surface*, *119*, 644–664. doi: 10.1002/2013JF002897.
Meacham-Hensold, K., Montes, C. M., Wu, J., Guan, K., Fu, P., Ainsworth, E. A., ... Bernacchi, C. J. (2019). High-throughput field phenotyping using hyperspectral reflectance and partial least squares regression (plsr) reveals genetic modifications to photosynthetic capacity. *Remote Sensing of Environment*, *231*, 111176. Retrieved from https://www.sciencedirect.com/science/article/pii/S0034425719301804 doi: https://doi.org/10.1016/j.rse.2019.04.029
Mobley, C. (1999). Estimation of the remote-sensing reflectance from above-surface measurements. *Applied Optics*, *38*(36), 7442. doi: 10.1364/ao.38.007442
Mobley, C., Boss, E., & Roesler, C. (2010). *Ocean opticsweb book.* Retrieved from http://www.oceanopticsbook.info/ (Accessed on 17 November 2023)
Moramarco, T., Barbetta, S., Bjerklie, D. M., Fulton, J. W., & Tarpanelli, A. (2019). River Bathymetry Estimate and Discharge Assessment from Remote Sensing. *Water Resources Research*, *55*(8), 6692–6711. doi: 10.1029/2018WR024220
Niroumand-Jadidi, M., Bovolo, F., & Bruzzone, L. (2020). SMART-SDB: Sample-specific multiple band ratio technique for satellite-derived bathymetry. *Remote Sensing of Environment*, *251*(January), 112091. Retrieved from https://doi.org/10.1016/j.rse.2020.112091 doi: 10.1016/j.rse.2020.112091
Niroumand-Jadidi, M., Legleiter, C. J., & Bovolo, F. (2022). Bathymetry retrieval from CubeSat image sequences with short time lags. *International Journal of Applied Earth Observation and Geoinformation*, *112*(July), 102958. Retrieved from https://doi.org/10.1016/j.jag.2022.102958 doi: 10.1016/j.jag.2022.102958
Niroumand-Jadidi, M., Pahlevan, N., & Vitti, A. (2019). Mapping substrate types and compositions in shallow streams. *Remote Sensing*, *11*(3). doi: 10.3390/rs11030262
Pahlevan, N., Smith, B., Binding, C., Gurlin, D., Li, L., Bresciani, M., & Giardino, C. (2020). Hyperspectral retrievals of phytoplankton absorption and chlorophyll-a in inland and nearshore coastal waters. *Remote Sensing of Environment*(xxxx), 112200. Retrieved from https://doi.org/10.1016/j.rse.2020.112200 doi: 10.1016/j.rse.2020.112200
Passalacqua, P., Belmont, P., & Foufoula-Georgiou, E. (2012). Automatic geomorphic feature extraction from lidar in flat and engineered landscapes. *Water Resources Research*, *48*(3). Retrieved from https://agupubs.onlinelibrary.wiley.com/doi/abs/10.1029/2011WR010958 doi: https://doi.org/10.1029/2011WR010958
Pegau, W. S., Gray, D., & Zaneveld, J. R. V. (1997). Absorption and attenuation of visible and near-infrared light in water: dependence on temperature and salinity. *Applied Optics*, *36*(24), 6035. doi: 10.1364/ao.36.006035
Probst, P., Wright, M. N., & Boulesteix, A. L. (2019). Hyperparameters and tuning strategies for random forest. *Wiley Interdisciplinary Reviews: Data Mining and*

Knowledge Discovery(2010), 1–18. doi: 10.1002/widm.1301

Pyo, J. C., Ligaray, M., Kwon, Y. S., Ahn, M. H., Kim, K., Lee, H., ... Cho, K. H. (2018). High-spatial resolution monitoring of phycocyanin and chlorophyll-a using airborne hyperspectral imagery. *Remote Sensing*, *10*(8). doi: 10.3390/rs10081180

Ribeiro, M. T., Singh, S., & Guestrin, C. (2016). "why should i trust you?": Explaining the predictions of any classifier. In *Proceedings of the 22nd acm sigkdd international conference on knowledge discovery and data mining* (p. 1135–1144). New York, NY, USA: Association for Computing Machinery. Retrieved from `https://doi.org/10.1145/2939672.2939778` doi: 10.1145/2939672.2939778

Shapley, L. S. (1953). A value for n-person games. In H. W. Kuhn & A. W. Tucker (Eds.), *Contributions to the theory of games (am-28), volume ii* (pp. 307–318). Princeton University Press. Retrieved from `https://doi.org/10.1515/9781400881970-018` doi: 10.1515/9781400881970-018

Simard, M., Denbina, M. W., Wright, K. A., & Jensen, D. (2020). The delta-x framework: A reality check for hydrodynamic, sediment transport and ecogeomorphic models. In *Ocean sciences meeting.*

Singer, M., Krivobokova, T., Munk, A., & de Groot, B. (2016). Partial least squares for dependent data. *Biometrika*, *103*(2), 351–362. Retrieved from `https://doi.org/10.1093/biomet/asw010` doi: 10.1093/biomet/asw010

Teresa Jarriel, P. P., John Swartz. (2021). Global rates and patterns of channel migration in river deltas. *Proceedings of the National Academy of Sciences*, *118*(46), e2103178118. Retrieved from `https://www.pnas.org/doi/abs/10.1073/pnas.2103178118` doi: 10.1073/pnas.2103178118

Thompson, D. R., Boardman, J. W., Eastwood, M. L., Green, R. O., Haag, J. M., Mouroulis, P., & Van Gorp, B. (2018a). Imaging spectrometer stray spectral response: In-flight characterization, correction, and validation. *Remote Sensing of Environment*, *204*(September 2017), 850–860. doi: 10.1016/j.rse.2017.09.015

Thompson, D. R., Cawse-Nicholson, K., Erickson, Z., Fichot, C. G., Frankenberg, C., Gao, B. C., ... Thompson, A. (2019). A unified approach to estimate land and water reflectances with uncertainties for coastal imaging spectroscopy. *Remote Sensing of Environment*, *231*(June), 111198. Retrieved from `https://doi.org/10.1016/j.rse.2019.05.017` doi: 10.1016/j.rse.2019.05.017

Thompson, D. R., Gao, B.-C., Green, R. O., Roberts, D. A., Dennison, P. E., & Lundeen, S. R. (2015). Atmospheric correction for global mapping spectroscopy: Atrem advances for the hyspiri preparatory campaign. *Remote Sensing of Environment*, *167*, 64-77. (Special Issue on the Hyperspectral Infrared Imager (HyspIRI)) doi: https://doi.org/10.1016/j.rse.2015.02.010

Thompson, D. R., Jensen, D., Chapman, J., Greenberg, E., & Simard, M. (2022). *Delta-x: Aviris-ng l2 surface reflectance, mrd louisiana, 2021. ornl daac, oak ridge, tennessee, usa.*

Thompson, D. R., Jensen, D., Chapman, J., Simard, M., & Greenberg, E. (2023). *Delta-X: AVIRIS-NG L2B BRDF-Adjusted Surface Reflectance, MRD, LA, 2021, V2.* `https://doi.org/10.3334/ORNLDAAC/2139`. ORNL DAAC, Oak Ridge, Tennessee, USA.

Thompson, D. R., Natraj, V., Green, R. O., Helmlinger, M. C., Gao, B. C., & Eastwood, M. L. (2018b). Optimal estimation for imaging spectrometer atmospheric correction. *Remote Sensing of Environment*, *216*(January), 355–373. Retrieved from `https://doi.org/10.1016/j.rse.2018.07.003` doi: 10.1016/j.rse.2018.07.003

Vanhellemont, Q. (2019). Daily metre-scale mapping of water turbidity using CubeSat imagery. *Optics Express*, *27*(20), A1372. doi: 10.1364/oe.27.0a1372

Wong, J., Liew, S. C., Wong, E., & Lee, Z. (2019). Modeling the remote-sensing reflectance of highly turbid waters. *Applied Optics*, *58*(10), 2671. doi: 10.1364/ao.58.002671

Woźniak, S. B., & Stramski, D. (2004). Modeling the optical properties of mineral particles suspended in seawater and their influence on ocean reflectance and chlorophyll estimation from remote sensing algorithms. *Applied Optics*, *43*(17), 3489–3503. doi: 10.1364/AO.43.003489

Wright, K., Passalacqua, P., Simard, M., & Jones, C. E. (2022). Integrating Connectivity Into Hydrodynamic Models: An Automated Open-Source Method to Refine an Unstructured Mesh Using Remote Sensing. *Journal of Advances in Modeling Earth Systems*, *14*(8). doi: 10.1029/2022MS003025

Wu, J., Li, W., Du, H., Wan, Y., Yang, S., & Xiao, Y. (2023). Estimating river bathymetry from multisource remote sensing data. *Journal of Hydrology*, *620*, 129567. Retrieved from `https://www.sciencedirect.com/science/article/pii/S0022169423005097` doi: https://doi.org/10.1016/j.jhydrol.2023.129567

Xie, C., Chen, P., Zhang, Z., & Pan, D. (2023). Satellite-derived bathymetry combined with Sentinel-2 and ICESat-2 datasets using machine learning. *Frontiers in Earth Science*, *11*(March), 1–16. doi: 10.3389/feart.2023.1111817

Zeng, C., Richardson, M., & King, D. J. (2017). The impacts of environmental variables on water reflectance measured using a lightweight unmanned aerial vehicle (UAV)-based spectrometer system. *ISPRS Journal of Photogrammetry and Remote Sensing*, *130*, 217–230. Retrieved from `http://dx.doi.org/10.1016/j.isprsjprs.2017.06.004` doi: 10.1016/j.isprsjprs.2017.06.004

Zhang, X., Ma, Y., Li, Z., & Zhang, J. (2022). Satellite derived bathymetry based on ICESat-2 diffuse attenuation signal without prior information. *International Journal of Applied Earth Observation and Geoinformation*, *113*(June). doi: 10.1016/j.jag.2022.102993

Zinger, J. A., Rhoads, B. L., Best, J. L., & Johnson, K. K. (2013). Flow structure and channel morphodynamics of meander bend chute cutoffs: A case study of the Wabash River, USA. *Journal of Geophysical Research: Earth Surface*, *118*(4), 2468–2487. doi: 10.1002/jgrf.20155

Figure 1.

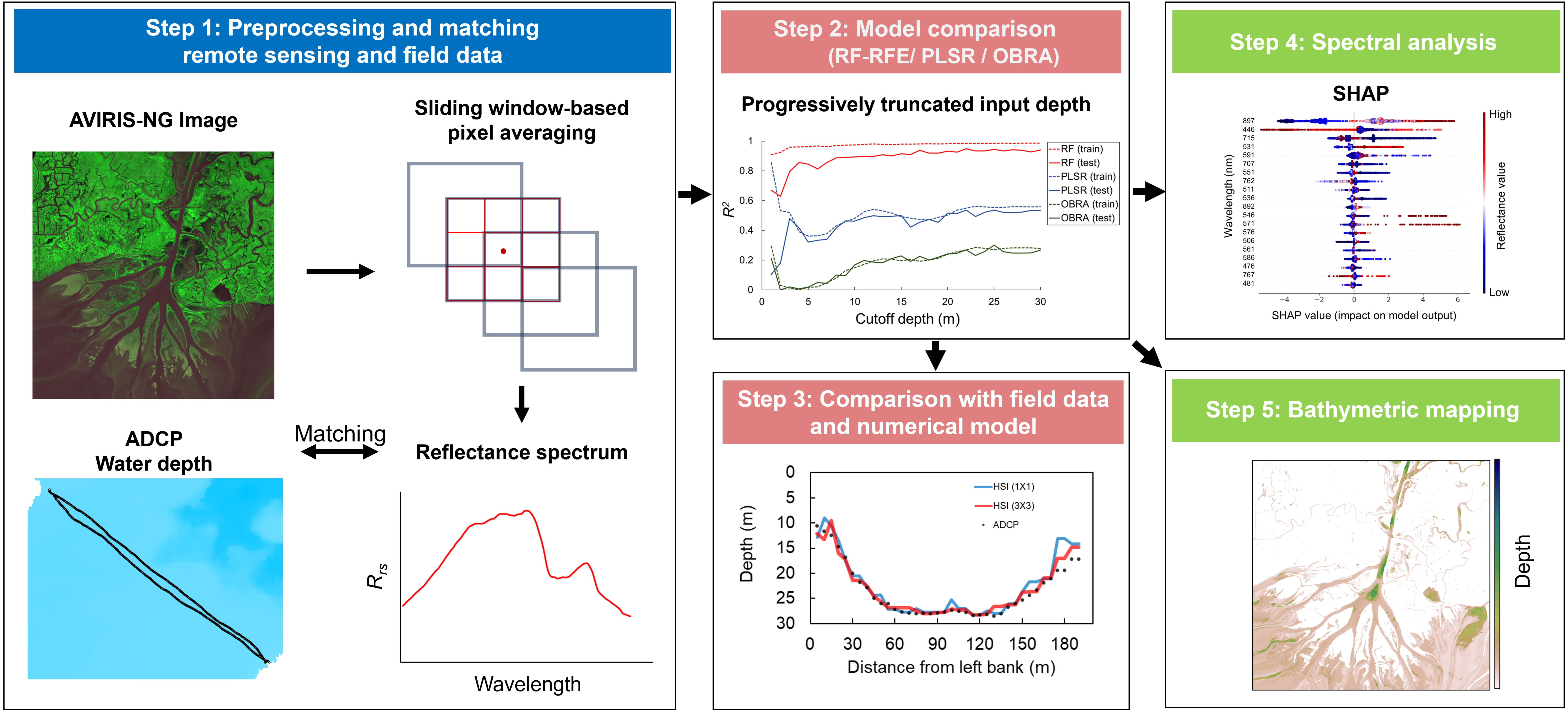

Step 1: Preprocessing and matching remote sensing and field data
AVIRIS-NG Image
Sliding window-based pixel averaging
ADCP Water depth
Matching
Reflectance spectrum
R_{rs}
Wavelength
Step 2: Model comparison (RF-RFE/ PLSR / OBRA)
Progressively truncated input depth
RF (train)
RF (test)
PLSR (train)
PLSR (test)
OBRA (train)
OBRA (test)
R^2
Cutoff depth (m)
Step 3: Comparison with field data and numerical model
HSI (1X1)
HSI (3X3)
ADCP
Depth (m)
Distance from left bank (m)
Step 4: Spectral analysis
SHAP
Wavelength (nm)
High
Reflectance value
Low
SHAP value (impact on model output)
Step 5: Bathymetric mapping
Depth

Figure 2.

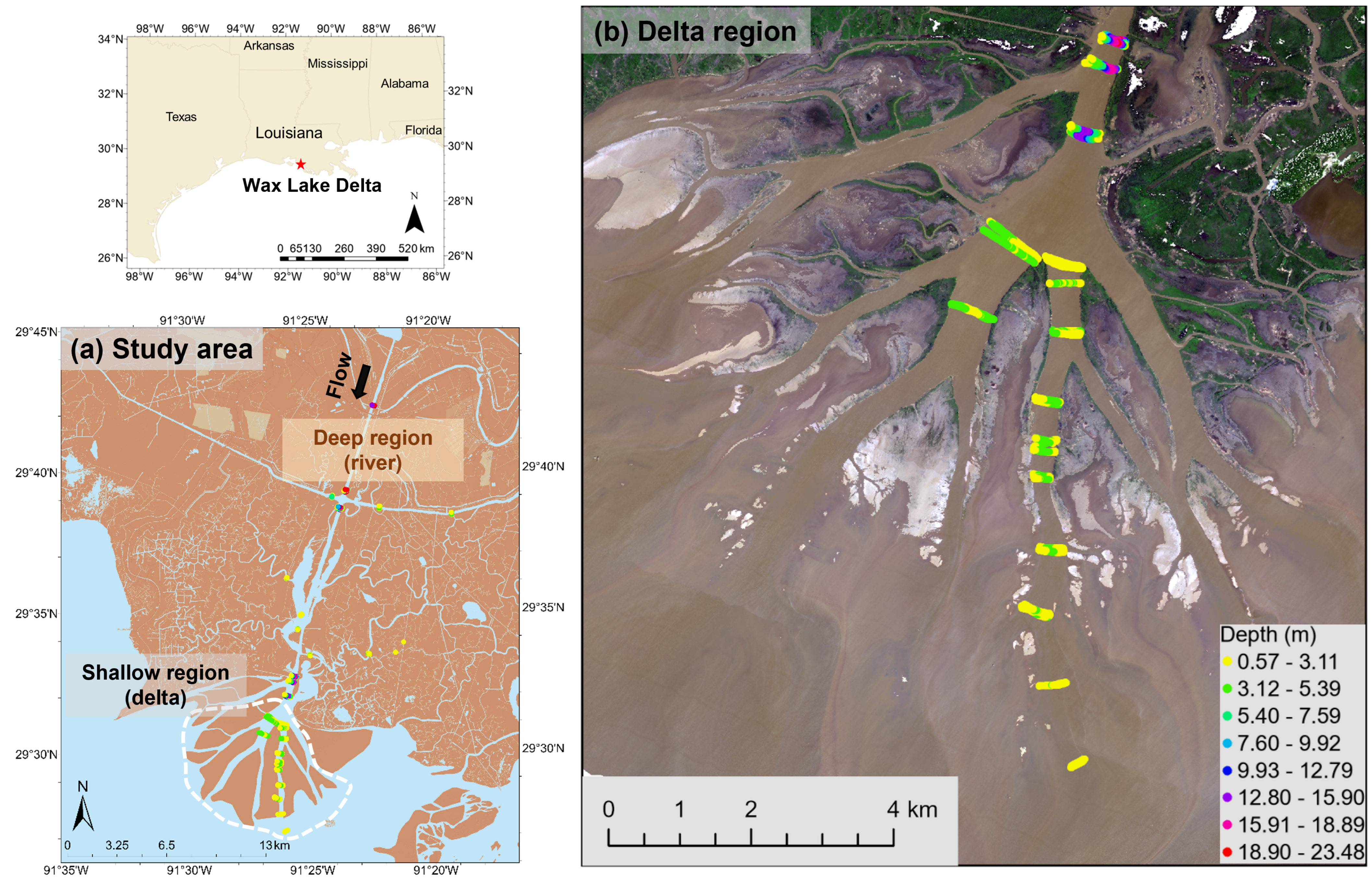

98°W
96°W
94°W
92°W
90°W
88°W
86°W
34°N
32°N
30°N
28°N
26°N
Arkansas
Mississippi
Alabama
Texas
Louisiana
Florida
Wax Lake Delta
N
0 65130 260 390 520 km
(a) Study area
91°30'W
91°25'W
91°20'W
29°45'N
29°40'N
29°35'N
29°30'N
Flow
Deep region (river)
Shallow region (delta)
N
0 3.25 6.5 13 km
91°35'W
(b) Delta region
0 1 2 4 km
Depth (m)
0.57 - 3.11
3.12 - 5.39
5.40 - 7.59
7.60 - 9.92
9.93 - 12.79
12.80 - 15.90
15.91 - 18.89
18.90 - 23.48

Figure 3.

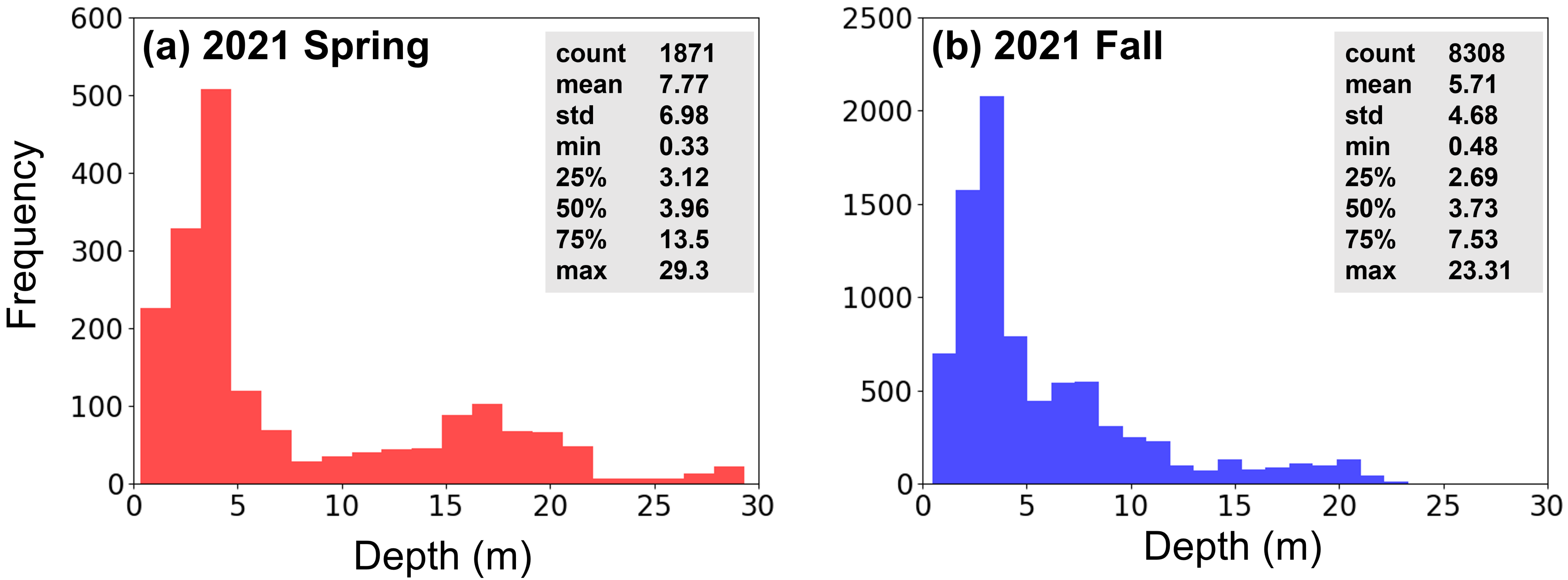
(a) 2021 Spring
count 1871
mean 7.77
std 6.98
min 0.33
25% 3.12
50% 3.96
75% 13.5
max 29.3
Frequency
Depth (m)
0
100
200
300
400
500
600
0
5
10
15
20
25
30
(b) 2021 Fall
count 8308
mean 5.71
std 4.68
min 0.48
25% 2.69
50% 3.73
75% 7.53
max 23.31
Depth (m)
0
500
1000
1500
2000
2500
0
5
10
15
20
25
30

Figure 4.

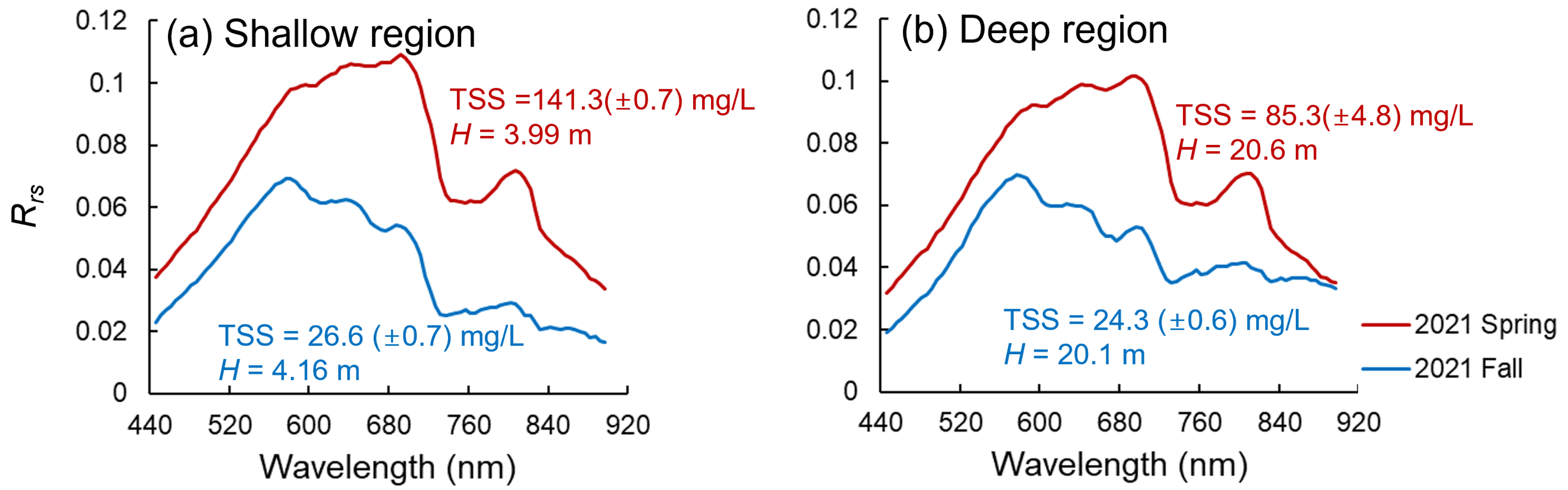
(a) Shallow region
TSS =141.3(±0.7) mg/L
H = 3.99 m
TSS = 26.6 (±0.7) mg/L
H = 4.16 m
(b) Deep region
TSS = 85.3(±4.8) mg/L
H = 20.6 m
TSS = 24.3 (±0.6) mg/L
H = 20.1 m
2021 Spring
2021 Fall
Rrs
0.12
0.1
0.08
0.06
0.04
0.02
0
440
520
600
680
760
840
920
Wavelength (nm)

Figure 5.

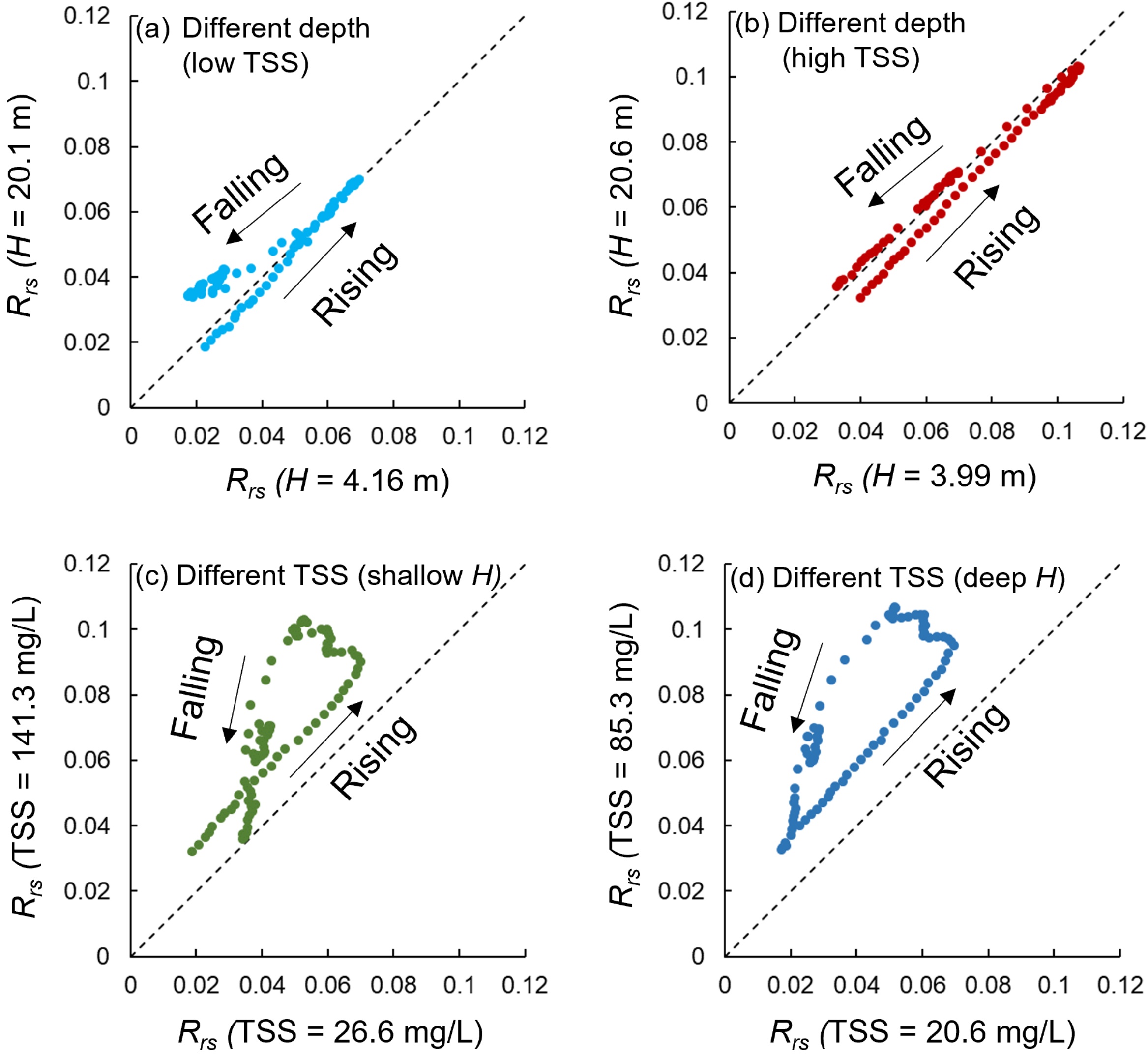

(a) Different depth (low TSS)
Falling
Rising
R_{rs} (H = 20.1 m)
R_{rs} (H = 4.16 m)
(b) Different depth (high TSS)
Falling
Rising
R_{rs} (H = 20.6 m)
R_{rs} (H = 3.99 m)
(c) Different TSS (shallow H)
Falling
Rising
R_{rs} (TSS = 141.3 mg/L)
R_{rs} (TSS = 26.6 mg/L)
(d) Different TSS (deep H)
Falling
Rising
R_{rs} (TSS = 85.3 mg/L)
R_{rs} (TSS = 20.6 mg/L)
0
0.02
0.04
0.06
0.08
0.1
0.12

Figure 6.

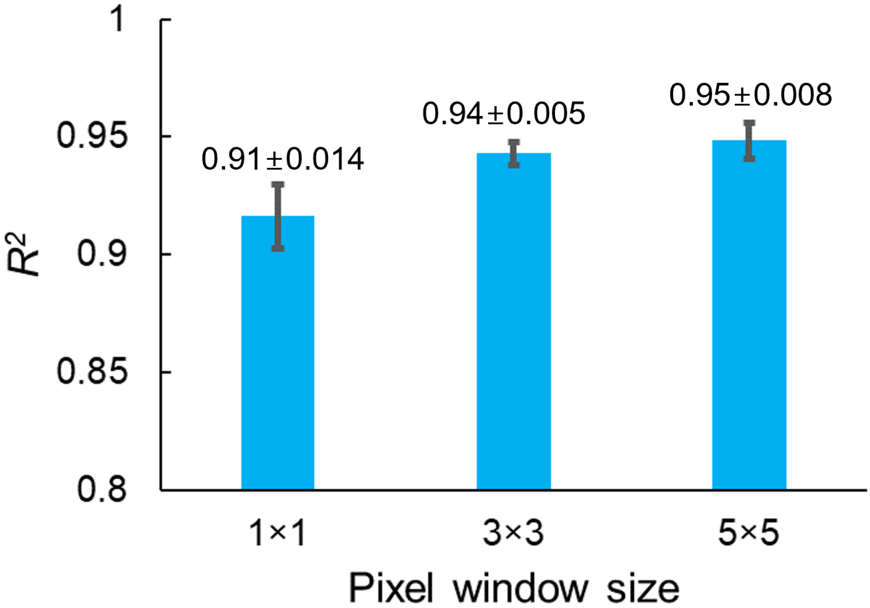

1
0.95
0.9
0.85
0.8
R^2
0.91±0.014
0.94±0.005
0.95±0.008
1×1
3×3
5×5
Pixel window size

Figure 7.

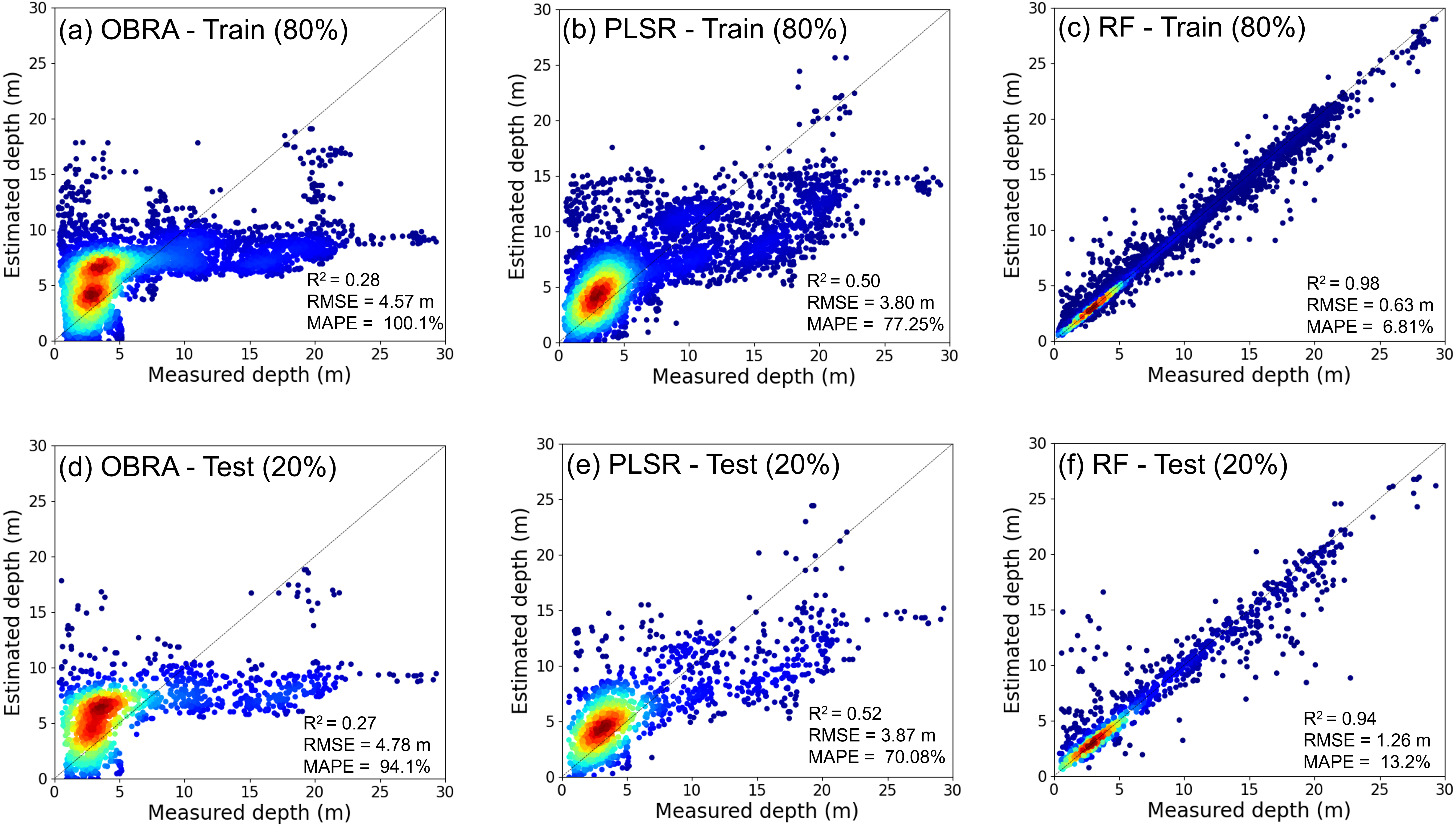

(a) OBRA - Train (80%)
R² = 0.28
RMSE = 4.57 m
MAPE = 100.1%
(b) PLSR - Train (80%)
R² = 0.50
RMSE = 3.80 m
MAPE = 77.25%
(c) RF - Train (80%)
R² = 0.98
RMSE = 0.63 m
MAPE = 6.81%
(d) OBRA - Test (20%)
R² = 0.27
RMSE = 4.78 m
MAPE = 94.1%
(e) PLSR - Test (20%)
R² = 0.52
RMSE = 3.87 m
MAPE = 70.08%
(f) RF - Test (20%)
R² = 0.94
RMSE = 1.26 m
MAPE = 13.2%
Estimated depth (m)
Measured depth (m)

Figure 8.

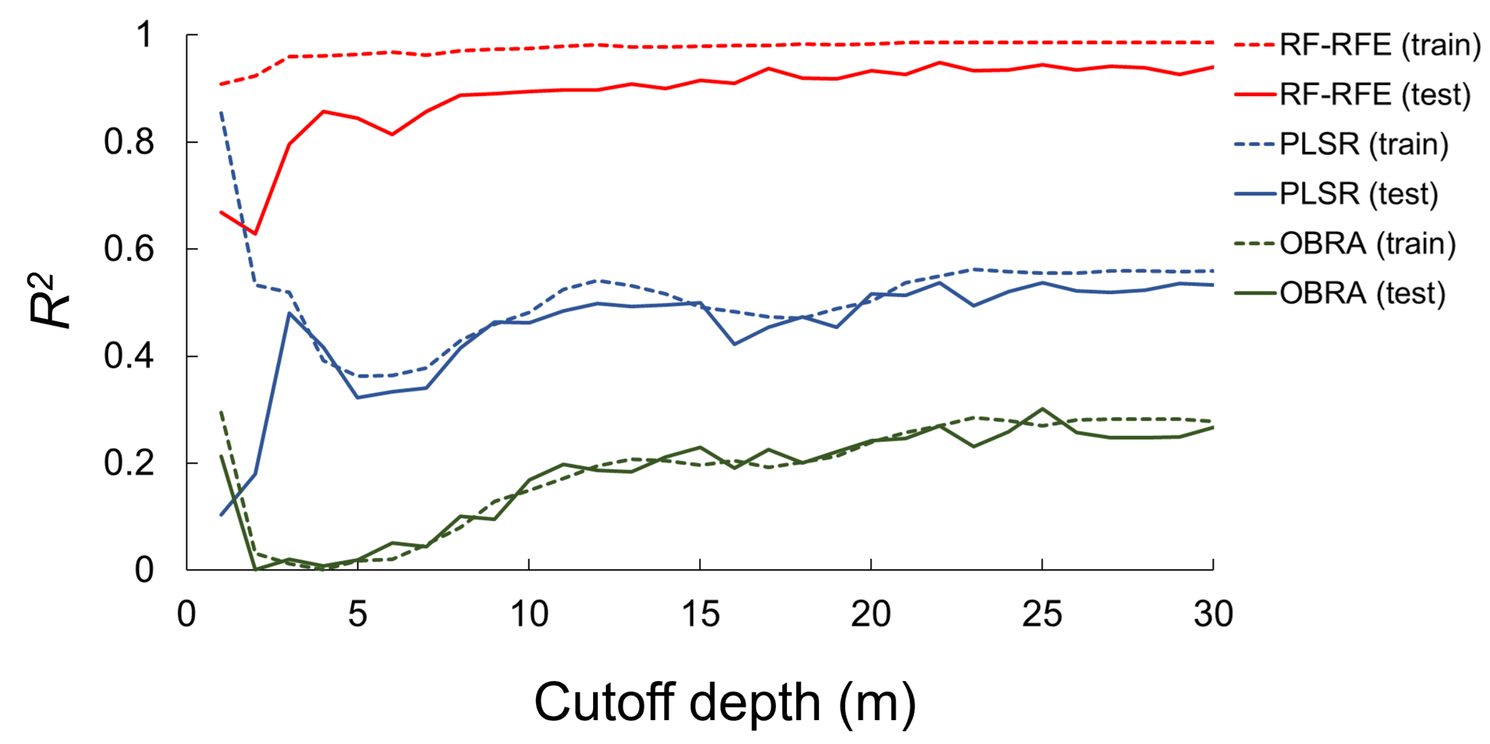

RF-RFE (train)
RF-RFE (test)
PLSR (train)
PLSR (test)
OBRA (train)
OBRA (test)
R^2
1
0.8
0.6
0.4
0.2
0
0
5
10
15
20
25
30
Cutoff depth (m)

Figure 9.

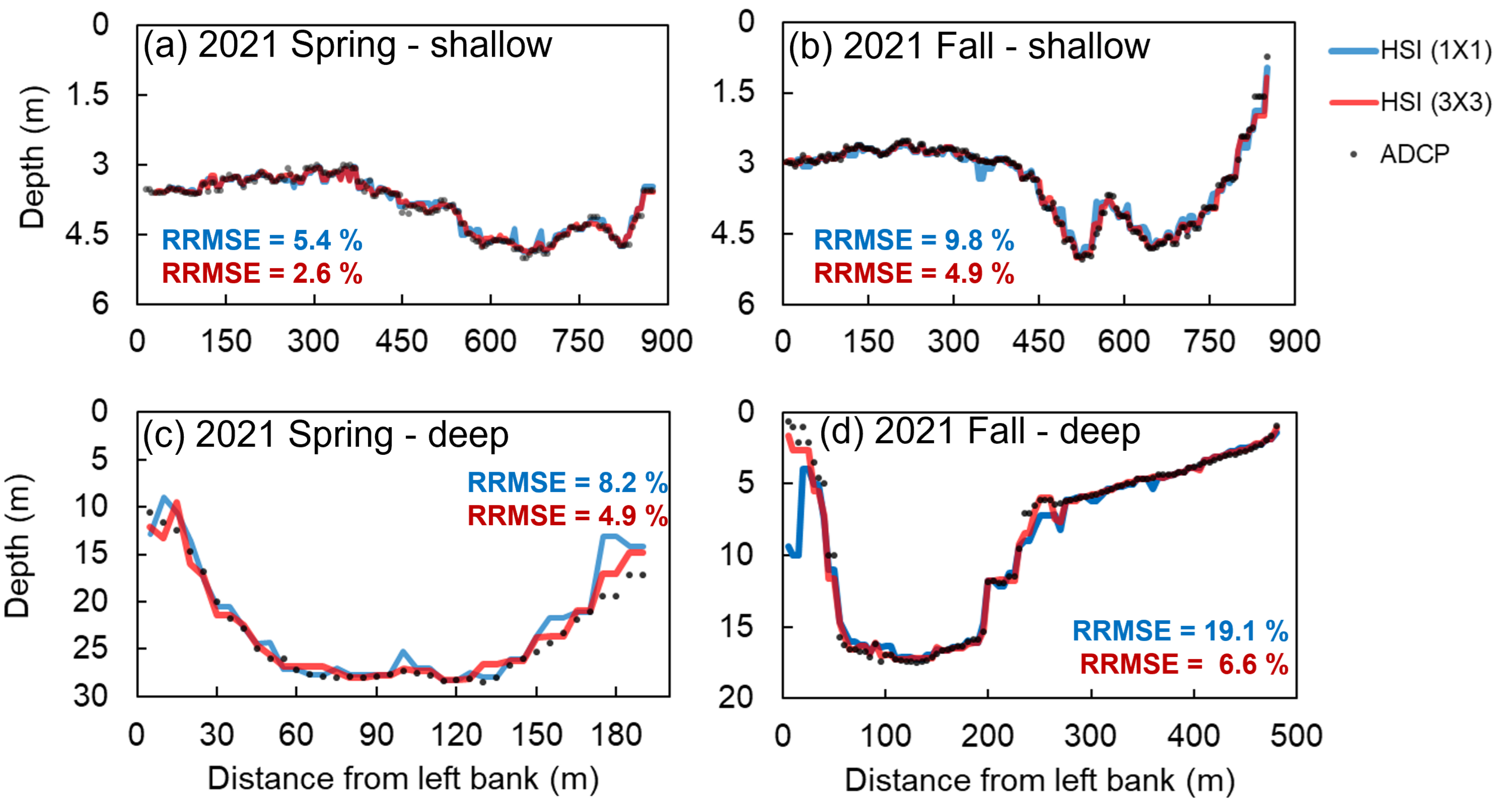

(a) 2021 Spring - shallow
(b) 2021 Fall - shallow
(c) 2021 Spring - deep
(d) 2021 Fall - deep
HSI (1X1)
HSI (3X3)
ADCP
RRMSE = 5.4 %
RRMSE = 2.6 %
RRMSE = 9.8 %
RRMSE = 4.9 %
RRMSE = 8.2 %
RRMSE = 4.9 %
RRMSE = 19.1 %
RRMSE = 6.6 %
Depth (m)
Distance from left bank (m)

Figure 10.

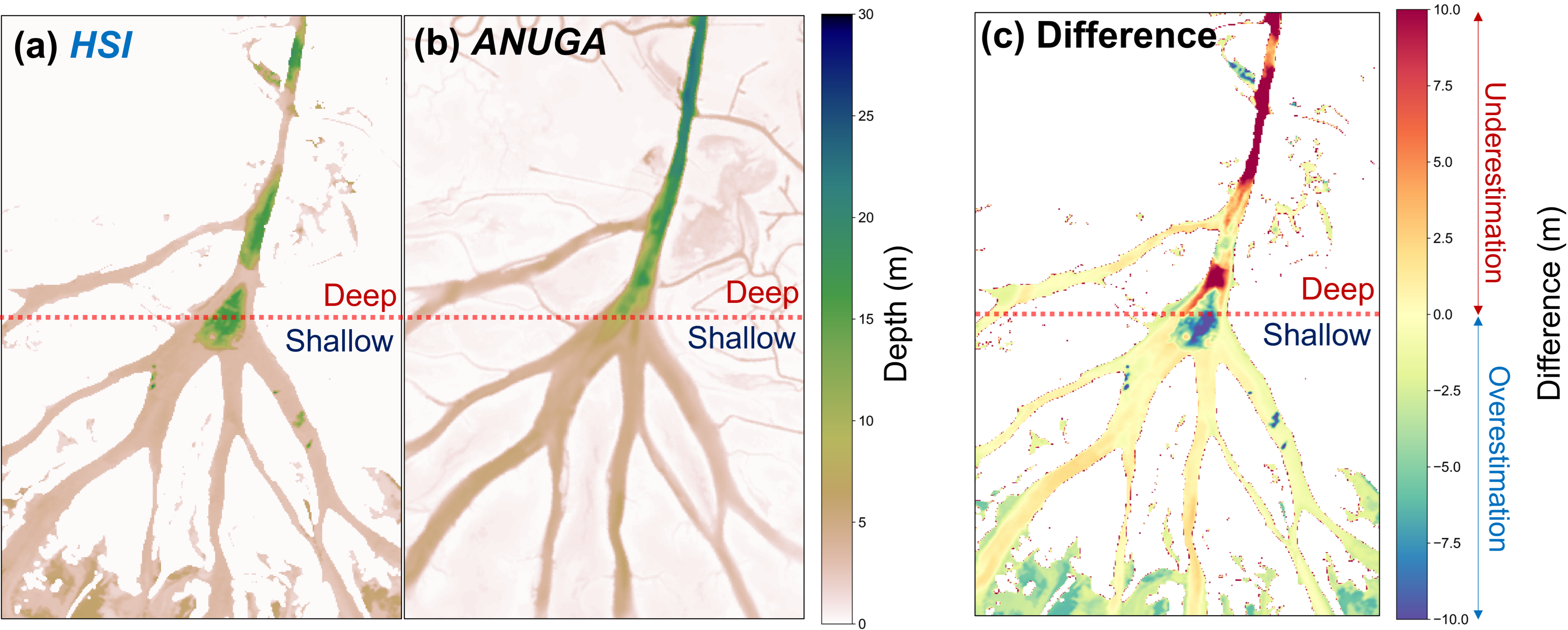

(a) HSI
(b) ANUGA
(c) Difference
Deep
Shallow
Deep
Shallow
Deep
Shallow
Depth (m)
30
25
20
15
10
5
0
Difference (m)
10.0
7.5
5.0
2.5
0.0
−2.5
−5.0
−7.5
−10.0
Underestimation
Overestimation

Figure 11.

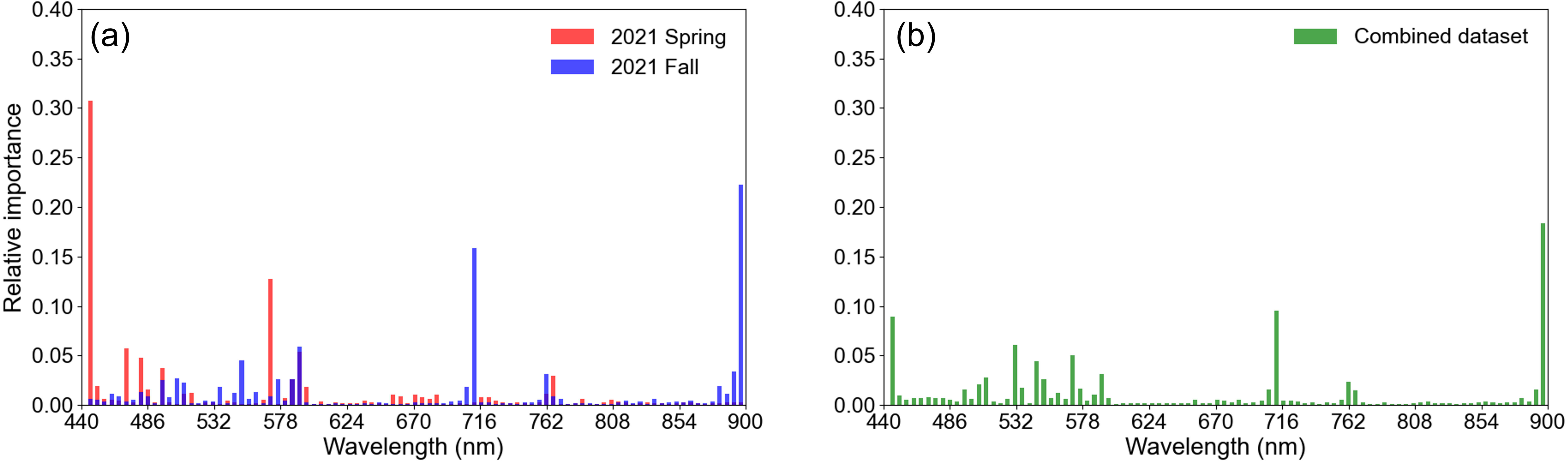

(a)
2021 Spring
2021 Fall
Relative importance
0.40
0.35
0.30
0.25
0.20
0.15
0.10
0.05
0.00
440
486
532
578
624
670
716
762
808
854
900
Wavelength (nm)
(b)
Combined dataset
0.40
0.35
0.30
0.25
0.20
0.15
0.10
0.05
0.00
440
486
532
578
624
670
716
762
808
854
900
Wavelength (nm)

Figure 12.

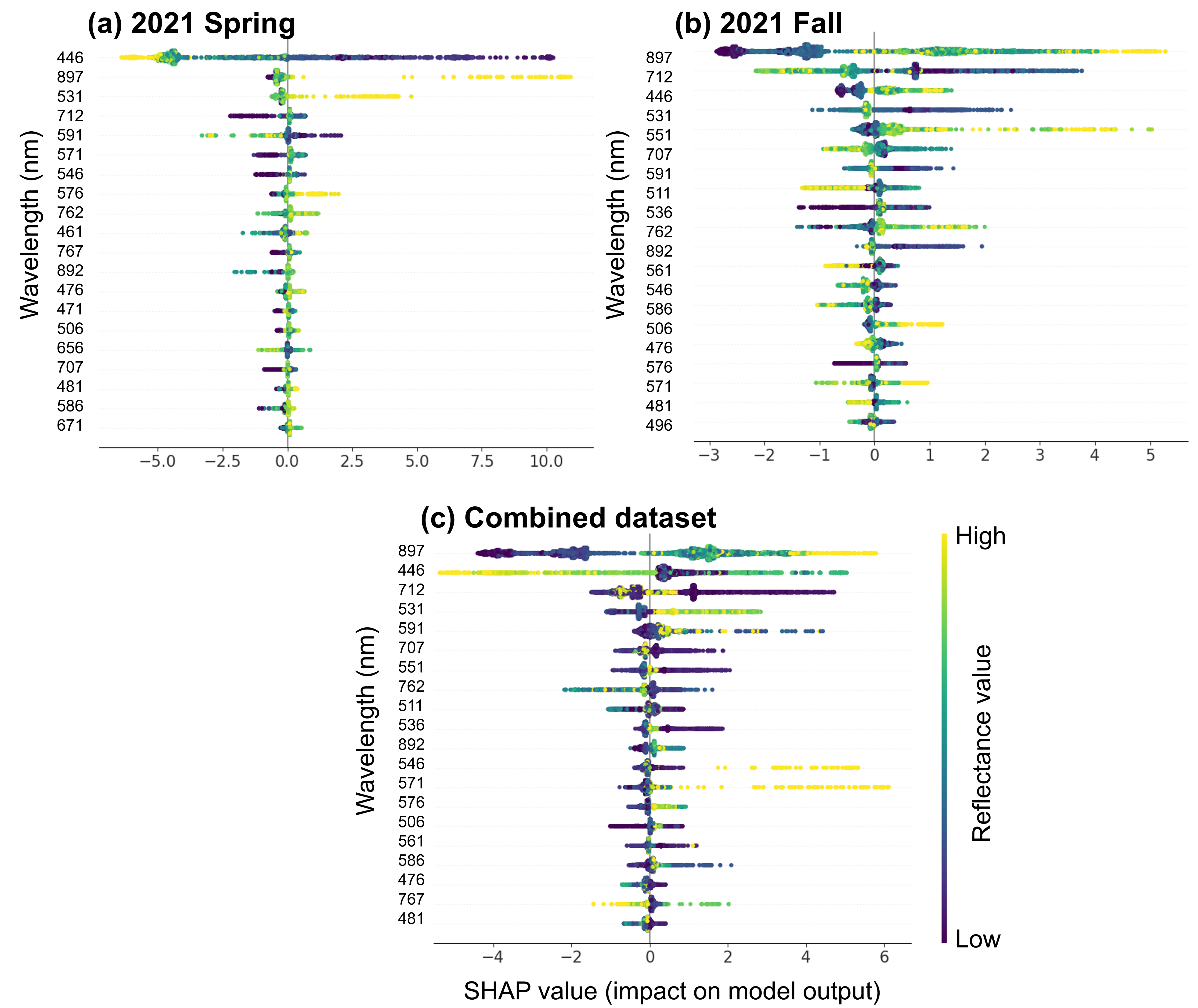
(a) 2021 Spring
(b) 2021 Fall
(c) Combined dataset
Wavelength (nm)
SHAP value (impact on model output)
Reflectance value
High
Low

Figure 13.

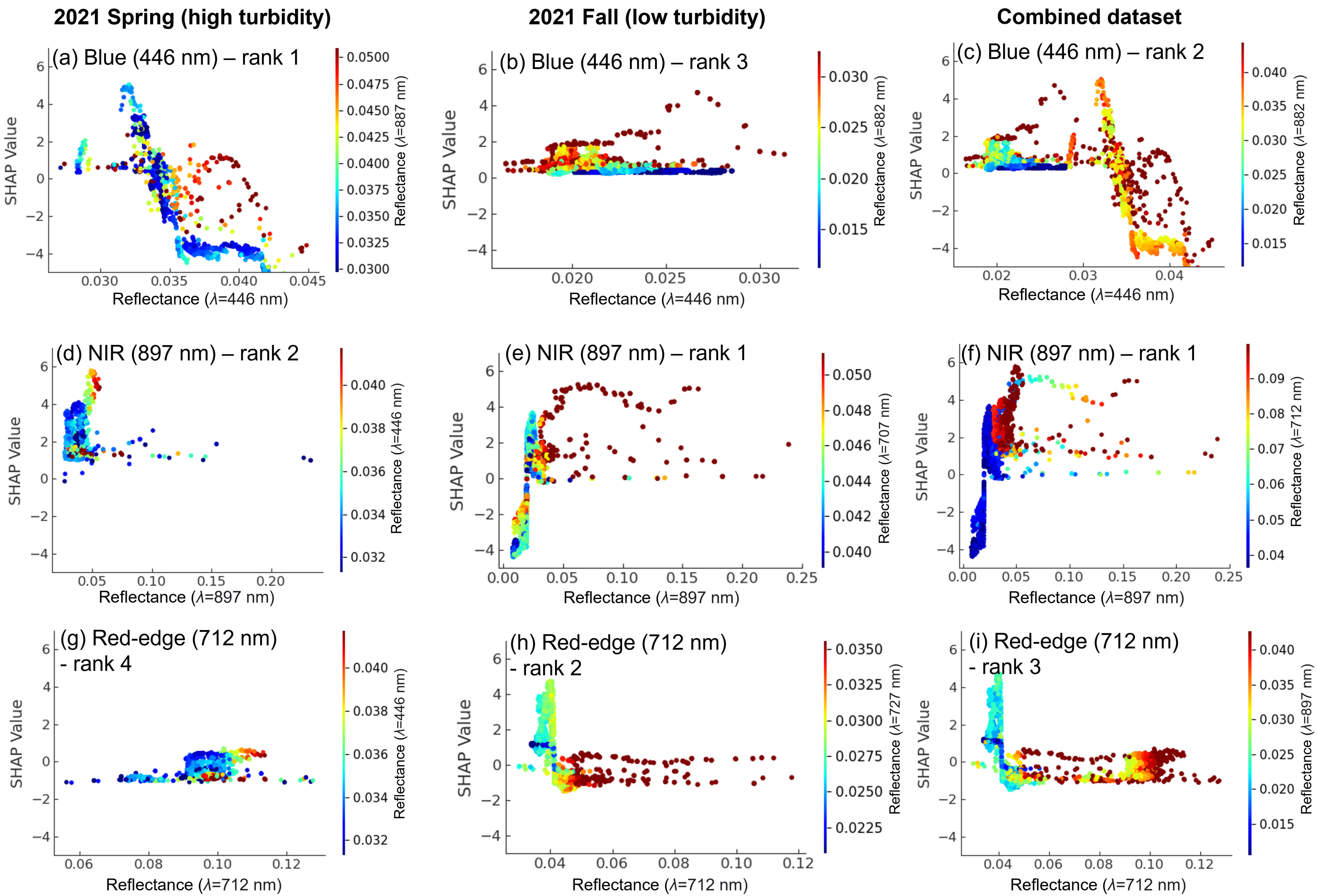

2021 Spring (high turbidity)
2021 Fall (low turbidity)
Combined dataset
(a) Blue (446 nm) – rank 1
(b) Blue (446 nm) – rank 3
(c) Blue (446 nm) – rank 2
(d) NIR (897 nm) – rank 2
(e) NIR (897 nm) – rank 1
(f) NIR (897 nm) – rank 1
(g) Red-edge (712 nm) - rank 4
(h) Red-edge (712 nm) - rank 2
(i) Red-edge (712 nm) - rank 3
SHAP Value
Reflectance (λ=446 nm)
Reflectance (λ=897 nm)
Reflectance (λ=712 nm)
Reflectance (λ=887 nm)
Reflectance (λ=882 nm)
Reflectance (λ=707 nm)
Reflectance (λ=727 nm)

Figure S1.

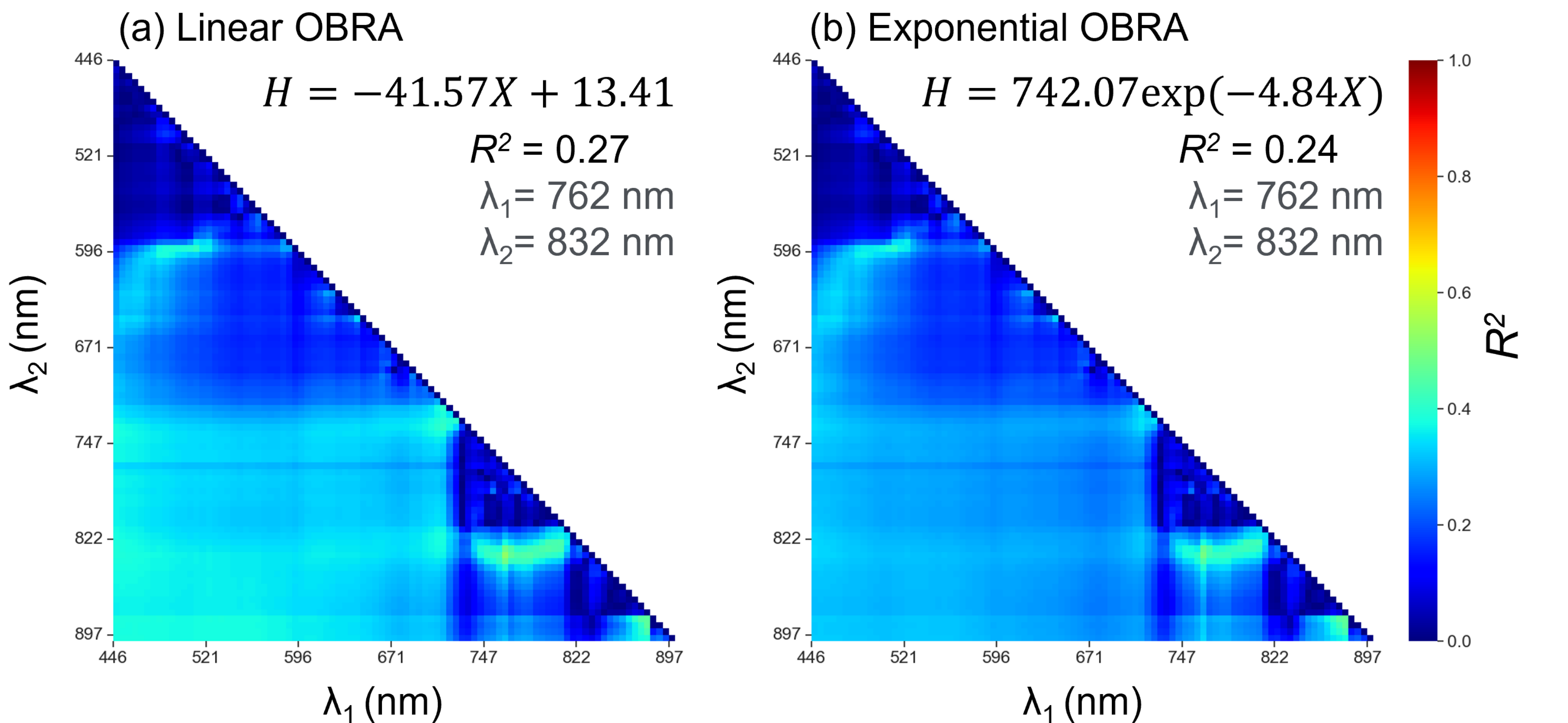

(a) Linear OBRA
$H = -41.57X + 13.41$
$R^2 = 0.27$
$\lambda_1 = 762$ nm
$\lambda_2 = 832$ nm
(b) Exponential OBRA
$H = 742.07\exp(-4.84X)$
$R^2 = 0.24$
$\lambda_1 = 762$ nm
$\lambda_2 = 832$ nm
λ_2 (nm)
λ_1 (nm)
446
521
596
671
747
822
897
R^2
0.0
0.2
0.4
0.6
0.8
1.0

Figure S2.

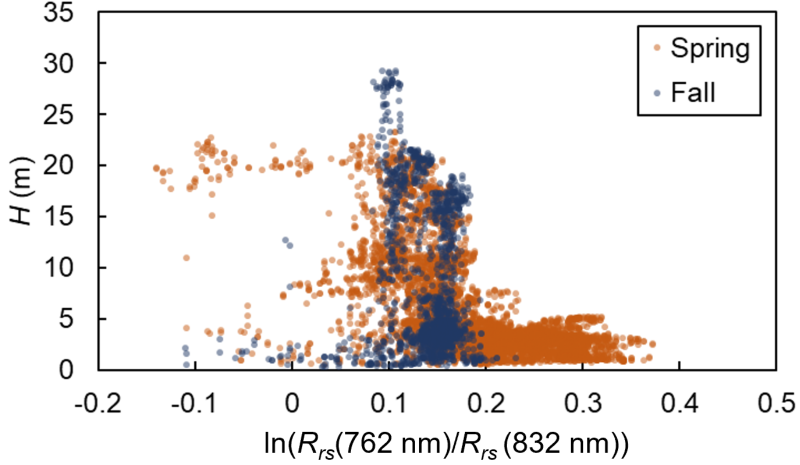

Spring
Fall
H (m)
35
30
25
20
15
10
5
0
-0.2
-0.1
0
0.1
0.2
0.3
0.4
0.5
ln(Rrs(762 nm)/Rrs (832 nm))

Figure S3.

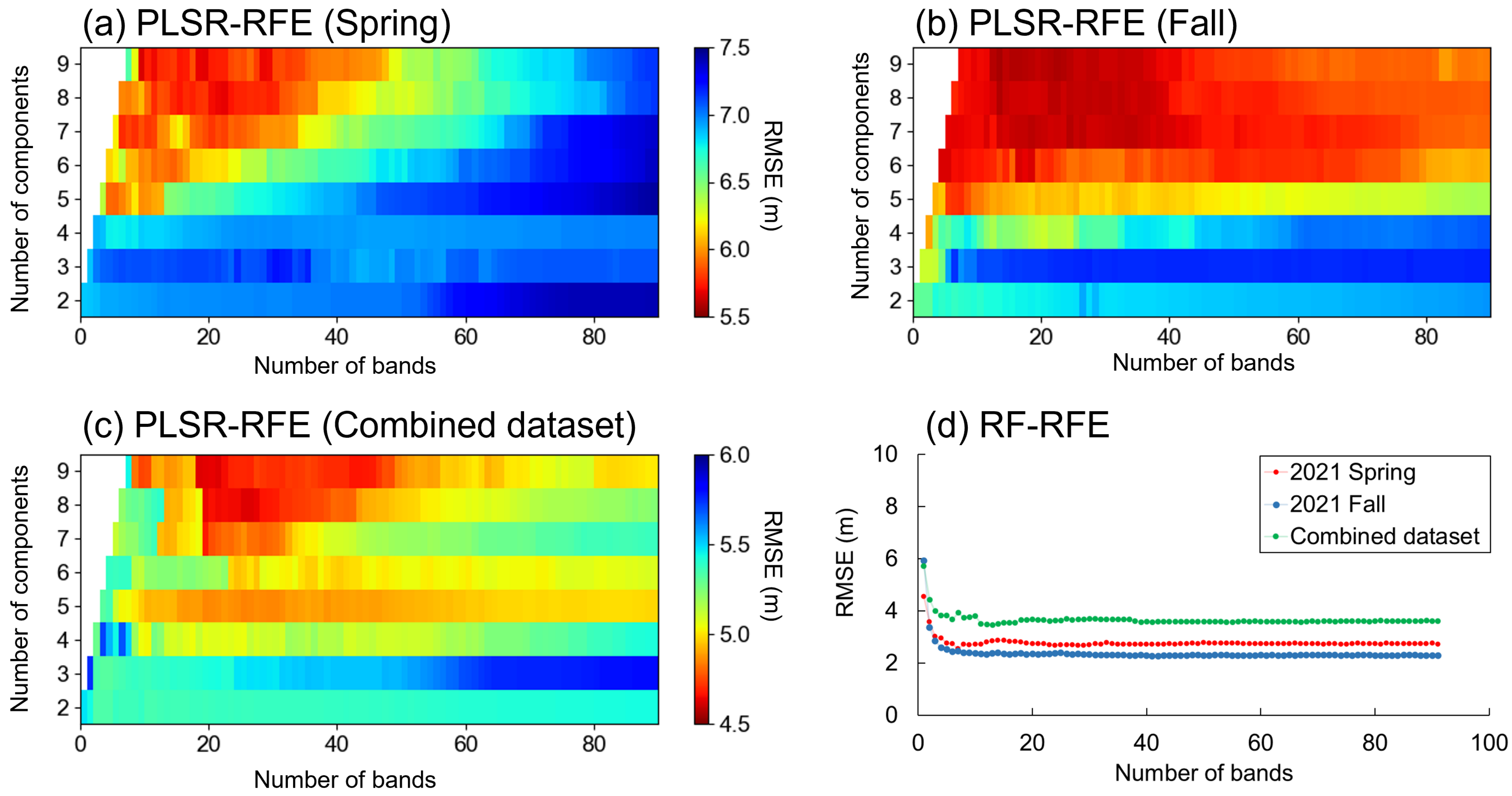

(a) PLSR-RFE (Spring)
(b) PLSR-RFE (Fall)
(c) PLSR-RFE (Combined dataset)
(d) RF-RFE
Number of components
Number of bands
RMSE (m)
2021 Spring
2021 Fall
Combined dataset

Figure S4.

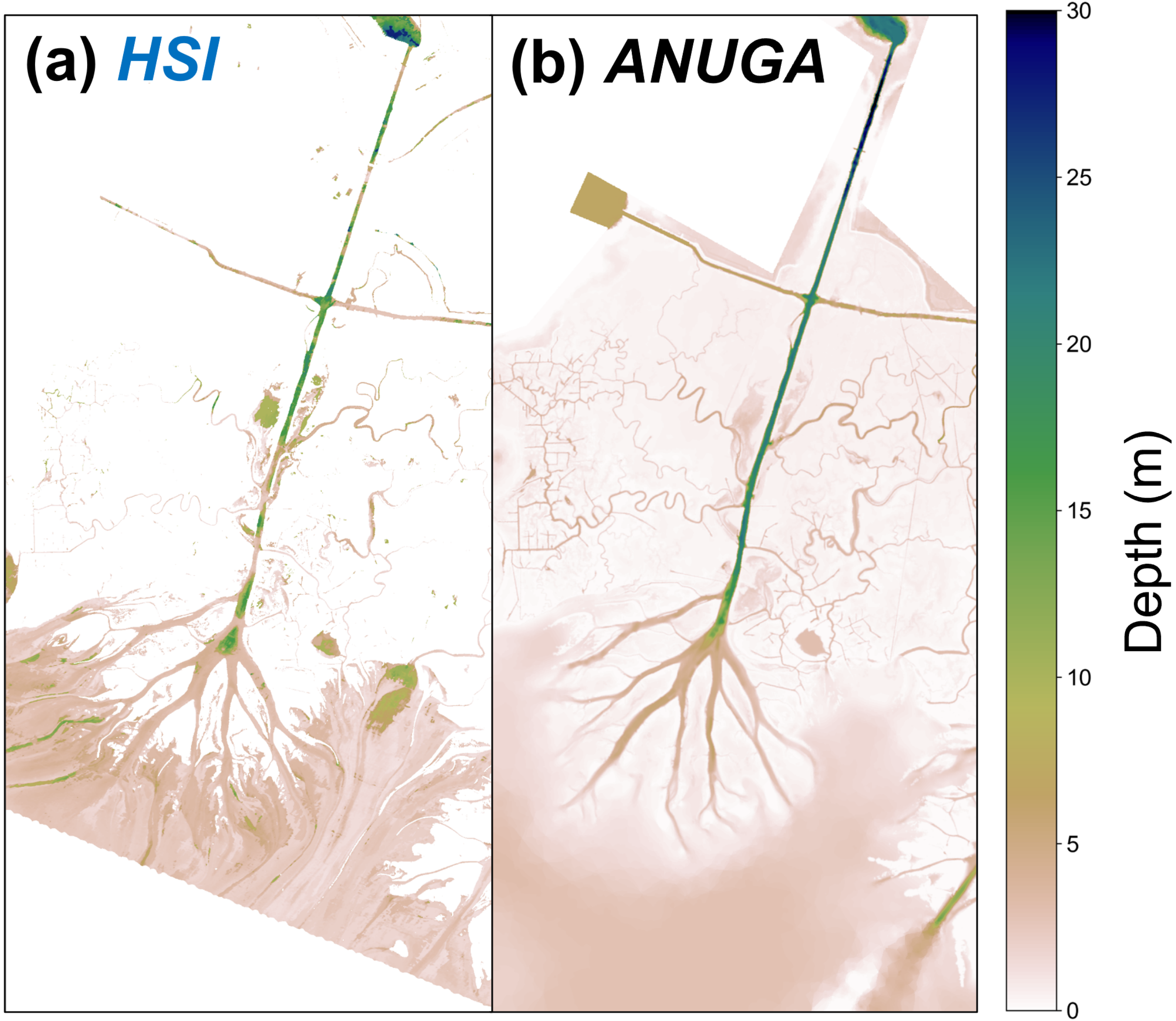
(a) HSI
(b) ANUGA
30
25
20
15
10
5
0
Depth (m)

Figure S5.

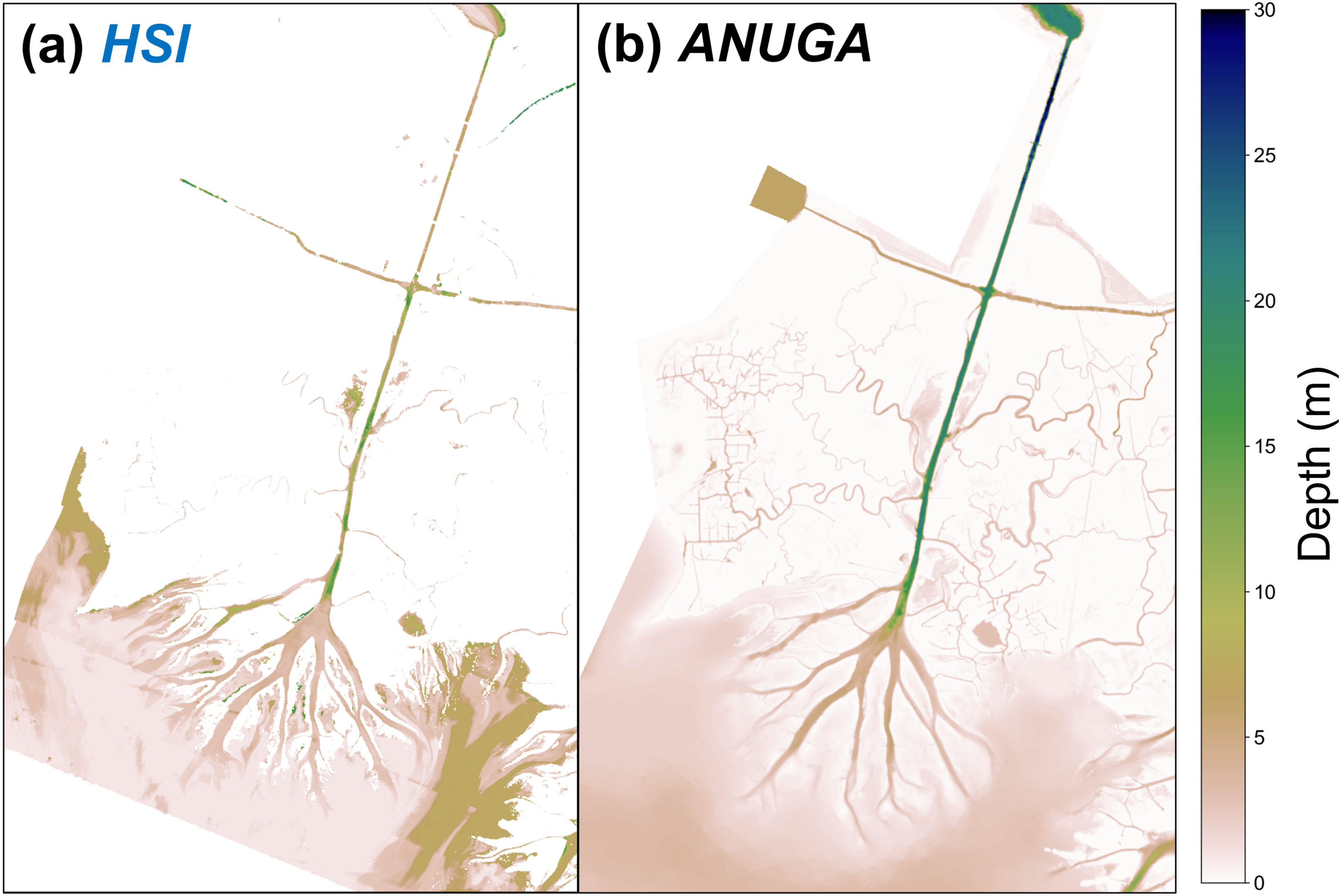

(a) HSI
(b) ANUGA
Depth (m)
30
25
20
15
10
5
0

Figure S6.

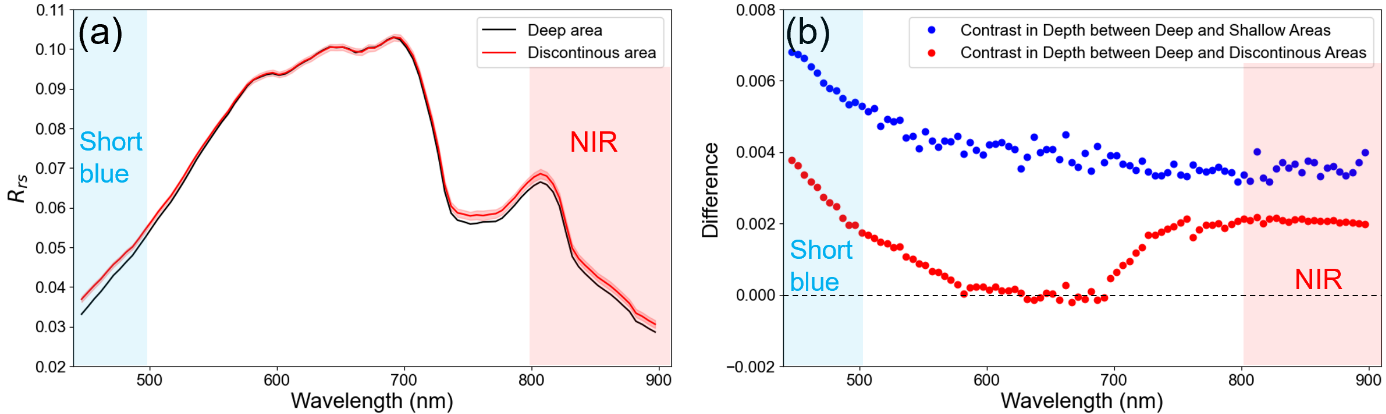

(a)
Deep area
Discontinous area
Short
blue
NIR
R_{rs}
0.11
0.10
0.09
0.08
0.07
0.06
0.05
0.04
0.03
0.02
500
600
700
800
900
Wavelength (nm)
(b)
Contrast in Depth between Deep and Shallow Areas
Contrast in Depth between Deep and Discontinous Areas
Short
blue
NIR
Difference
0.008
0.006
0.004
0.002
0.000
−0.002
500
600
700
800
900
Wavelength (nm)

Supporting Information for "Depth Mapping in Turbid and Deep Waters Using AVIRIS-NG Imagery: A Study in Wax Lake Delta, Louisiana, USA"

Siyoon Kwon[1], Paola Passalacqua[1,2], Antoine Soloy[3], Daniel Jensen[3], Marc Simard[3]

[1]Maseeh Department of Civil, Architectural and Environmental Engineering, The University of Texas at Austin, Austin, TX, USA

[2]Department of Earth and Planetary Sciences, The University of Texas at Austin, Austin, TX, USA

[3]Jet Propulsion Laboratory, California Institute of Technology, Pasadena, CA, USA

Contents of this file

1. Figures S1 to S6

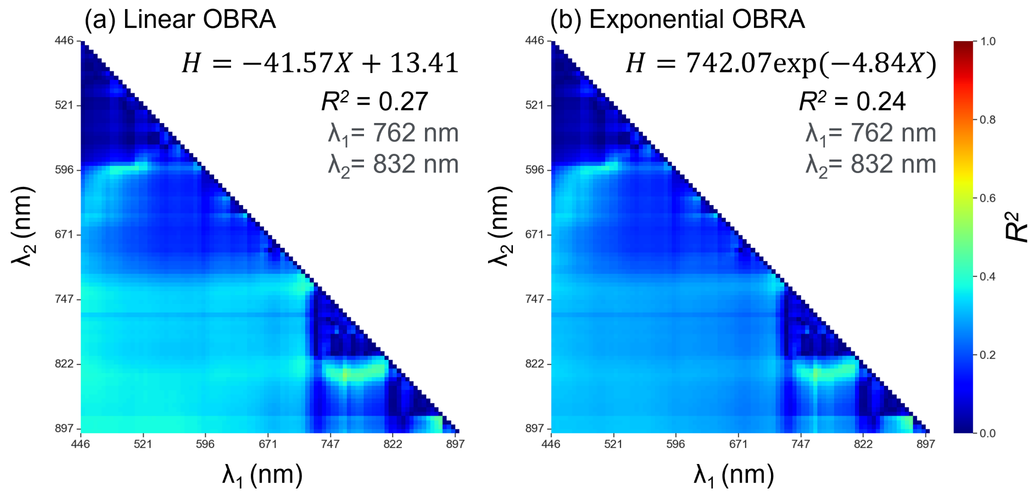

Figure S1. OBRA matrices, regression equations, and selected wavelengths for (a) linear and (b) exponential forms.

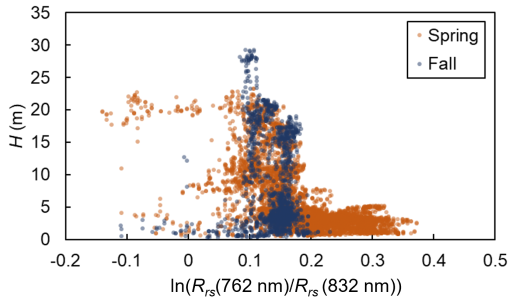

Figure S2. Relationships between optimal band ratio and water depth during Spring and Fall campaigns.

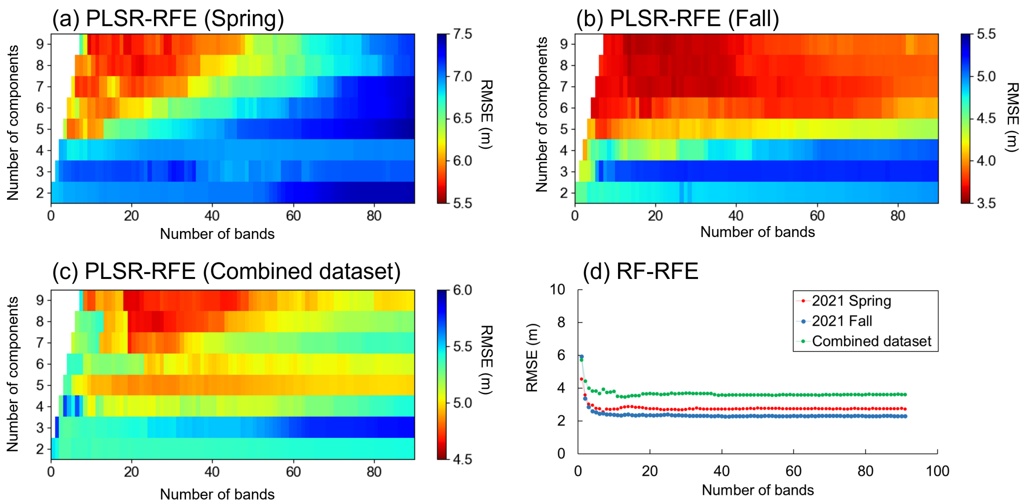

Figure S3. Results of RFE-CV for (a-c) PLSR and (d) RF: RMSE values according to the number of selected spectral bands and components (latent variables in PLSR).

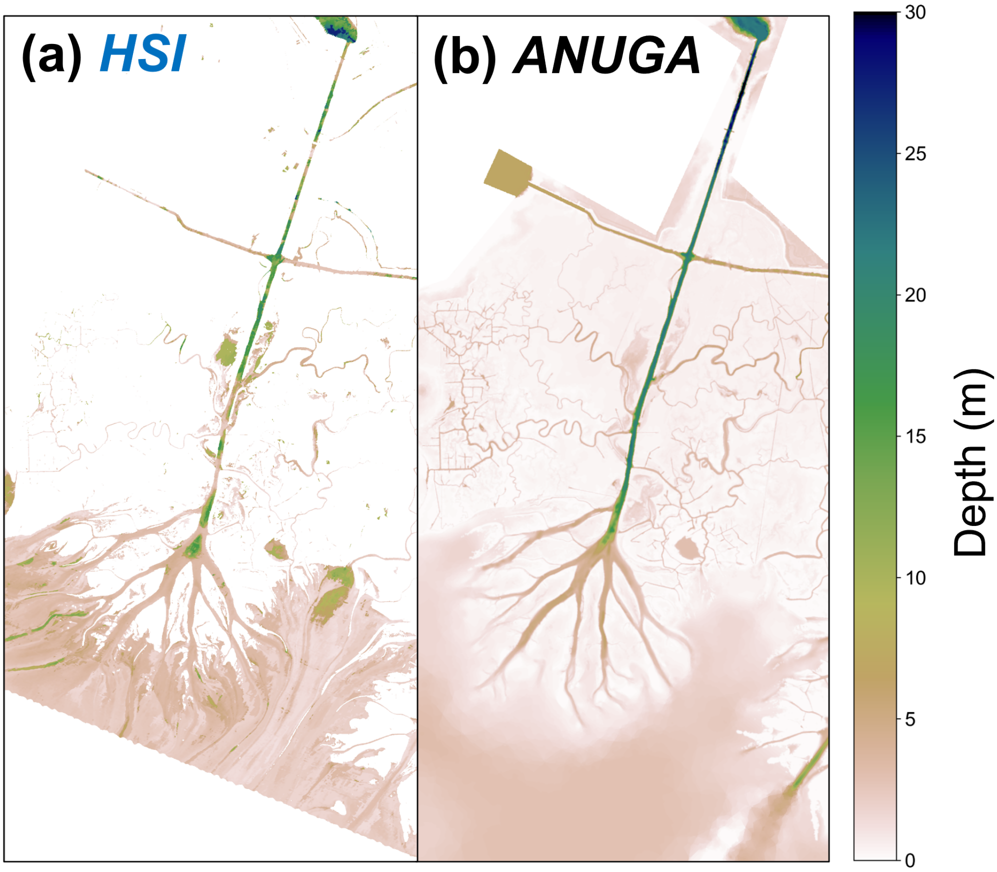

Figure S4. Retrieved depth map by RF-RFE during Spring campaign.

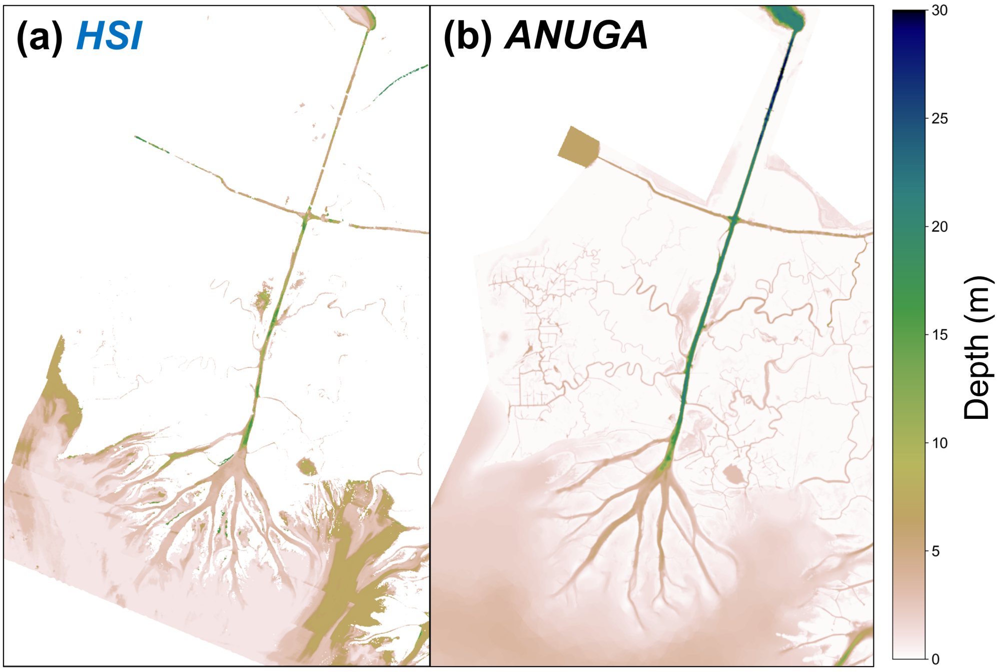

Figure S5. Retrieved depth map by RF-RFE during Fall campaign.

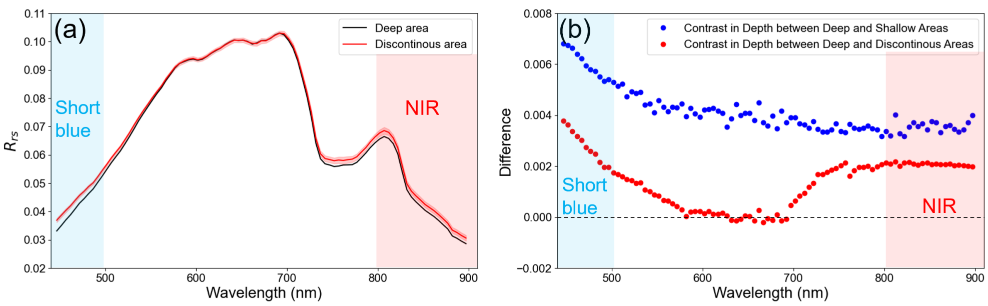

Figure S6. (a) Averaged reflectance spectrum of deep and discontinuous areas. (b) Reflectance difference between deep and shallow areas and deep and discontinuous areas.